INVESTIGATING THE AUTOMATION OF THE 3D COMPUTATIONAL MODEL DEVELOPMENT WORKFLOW OF THE COCHLEAR IMPLANT

by

Heinrich George Crous

Submitted in partial fulfilment of the requirements for the degree
Master of Engineering (Bioengineering)

in the

Department of Electrical, Electronic and Computer Engineering
Faculty of Engineering, Built Environment and Information Technology

UNIVERSITY OF PRETORIA

July 2018

ACKNOWLEDGEMENTS

Financial assistance provided by the National Research Foundation (NRF) in respect of the costs of this study is hereby acknowledged. Opinions or conclusions that have been expressed in this study are those of the writer and must not be seen to represent the views, opinions or conclusions of the NRF.

I wish to extend my sincere gratitude to my family and friends for their contribution to this research script through continuous support, encouragement and their faith in my abilities.

SUMMARY

INVESTIGATING THE AUTOMATION OF THE 3D COMPUTATIONAL MODEL DEVELOPMENT WORKFLOW OF THE COCHLEAR IMPLANT

by

Heinrich George Crous

Supervisor: Prof T. Hanekom

Co-supervisor: Prof J.J. Hanekom

Department: Electrical, Electronic and Computer Engineering

University: University of Pretoria

Degree: Master of Engineering (Bioengineering)

Keywords: Simulation, cochlear implant, computational modelling, 3D model, automation.

The workflow of the development of three-dimensional (3D) computational models for cochlear implants was investigated, with specific focus on applied automation techniques. No fully automated process was found in the literature that could perform the entire 3D model development from the first to the final stage, with the greatest lack of automation identified in the data interpretation and processing phase. It is proposed that the workflow of 3D model development can be automated to such an extent that an automated cochlear model generator can be developed. The aim of such a method is to reduce time spent on model development, and decrease the number of complicated manual procedures often involved in 3D model development whilst maintaining model accuracy. A knowledge-based landmark detection algorithm was used to develop a semi-automated cochlear model creation tool by using standard CT scan data. Six 3D electric volume conduction models were produced by applying the automated method. Electric potential distributions, as a result of intracochlear stimulation, were calculated and then used to predict neural activating function patterns. Predictions from models resulting from automated generation were compared to predictions from models that were created by a purely manual generation method. Automation of the model development workflow was achieved, although an initial manual calibration procedure was required for each model. For the

development of 3D models, the use of multiple geometrical landmark points (GLP) greatly affected cochlear model morphology, potential distributions, and neural excitement as opposed to the use of a singular GLP.

This work suggests that the semi-automated method developed and presented in this study is able to detect cochlear landmarks with an 84.28% similarity to the manual method. Higher intracochlear potentials were predicted with the automated method because of the reduced volume of the automatically generated models compared to that of manually created models. The higher potentials indicated a greater probability of neural excitation when compared to the manually created models, under similar stimulation conditions.

OPSOMMING

ONDERSOEK OP DIE OUTOMATISERING VAN DIE DRIE DIMENSIONELE MODEL ONTWIKKELLING PROSES VAN 'N KOGLEÊRE INPLANTING

deur

Heinrich George Crous

Studieleier: Prof T. Hanekom

Medestudieleier: Prof J.J. Hanekom

Departement: Elektriese, Elektroniese en Rekenaaringenieurswese

Universiteit: Universiteit van Pretoria

Graad: Magister in Ingenieurswese (Bio-Ingenieurswese)

Sleutelwoorde: Drie-dimensioneel, kogleêre inplanting, 3D model, outomatisering, modellering

Die proses waarvolgens drie-dimensionele (3D) simuleringsmodelle vir kogleêre modelle ontwikkel word was ondersoek met spesifieke fokus op toegepaste outomatiseringstegnieke. Tot op hede bestaan daar geen modelontwikkelingstegniek wat ten volle geoutomatiseer is vir die ontrekking van rou data tot ‘n volledige 3D model nie. Die grootste gaping i.t.v. outomatisering in hierdie proses word gesien in die verwerking en verfyning van data. Die studie hipotese veronderstel dat die modelontwikkelingsproses verder ge-outomatiseer kan word tot so mate dat ‘n algoritme ontwikkel word en geïmplimenteer kan word vir meer kliniese doeleindes. Die doel van die studie was om die tyd wat spandeer word op modelontwikkelling te verminder deur die outomatiseringstegnieke toe te pas sonder om die akkuraatheid van die so ‘n 3D model te verminder. Semi-outomatiese tegnieke was toegepas, waarvan ‘n kennisgedrewe algoritme ingesluit was om kogleêre landmerkpunte the identifiseer; asook beeldintensiteitgedrewe tegnieke om die elektrodetrajek te bepaal. Ses 3D modelle van kogleas, elk met ‘n ingeplante elektrode, is ontwikkel deur die tegniek en vergelyk met modelle wat met die hand ontwikkel is. Outomatiseringstegnieke het die tydsduur van die model se ontwikkelingsproses verbeter en verkort, alhoewel daar gedurende die proses ‘n kalibreringsproses nodig was wat met die hand geïmplimenteer moes word. Die modelle wat ontwikkel is deur die outomatiese metode, het al drie kogleêree landmerkpunte

ingesluit en het merkwaardige verskille in die model volume, geometrie, elektriese potensiaal verspreiding en neurale aktiwiteit van die modelle aangedui. Die studie dui daarop dat dit moontlik is om deur middel van ‘n semi-geoutomatiseerde proses ‘n 3D model te ontwikkel wat kogleêre landmerkpunte kan meet, met ‘n 84.28% ooreenstemming met metings wat met die hand gedoen is. Die modelle wat ontwikkel is deur die semi-geoutomatiseerde proses dui ook aan op ‘n hoër elektriese potensiaal verspreiding en meer neurale aktiwiteit onder konstante stimuleringsomstandighede.

LIST OF ABBREVIATIONS

CI	Cochlear Implant
CT	Computed Tomography
FEM	Finite Element Method
μ-CT	Micro Computed Tomography
KBLDA	Knowledge based Landmark Detection Algorithm
MBD	Model-based Diagnostics
MPM	Model-predicted Mapping
NRMSE	Normalised-Root-Mean-Squared-Error
SST	Statistical Shape Model

TABLE OF CONTENTS

CHAPTER 1 INTRODUCTION

1.1 PROBLEM STATEMENT

1.1.1 Context of the problem

Since the first use of auditory prosthesis such as cochlear implants, the restoration of the ability to hear became a possibility for individuals who suffer from severe hearing loss. These devices work through electrical stimulation of the auditory nerve fibres. Sound signals are detected by an external microphone, which is then digitally encoded by a speech processor. The signals are transmitted to the electrode array implanted into the individual's cochlea. The implanted electrode array delivers current pulses to the surviving auditory nerve fibres at different locations along the length of the cochlea. These current pulses excite the cochlear neurons and are perceived as sound by the brain.

The level of benefit that different users receive from such an implanted device varies and remains difficult to predict. The use of three-dimensional (3D) computational models made it possible for researchers to better understand how neuroprosthetic devices would function under various conditions for various users (Malherbe, 2009, Noble et al., 2011, Malherbe et al., 2013, Malherbe et al., 2015, Tran et al., 2015, Braithwaite et al., 2016, Malherbe et al., 2016, Mangado et al., 2016, Gross, 2017). Since the development of 3D models, interest in the use of such models has grown (Agrawal and Newbold, 2012), specifically in the development of models to assist in the understanding and predicting of the responses of an electrically stimulated cochlea. Some studies have extended upon the use of generic models to more user-specific models, which indicated a significant variability in results by including user-specific characteristics in models (Malherbe, 2009,

Noble et al., 2011, Malherbe et al., 2013, Malherbe et al., 2015, Tran et al., 2015, Malherbe et al., 2016, Gross, 2017). User-specific models have also shown promise for clinical application (Hanekom and Hanekom, 2016), specifically in model-based diagnostics (MBD), as one study has investigated possible causes and solutions to facial nerve stimulation as a result of an electrically stimulated cochlea for a specific user (Gross, 2017).

In the majority of studies, the level of detail in these 3D models often does not include finer cochlear structures or naturally variable cochlear characteristics. By including more detail and accommodating user-variances, models can be tailored to describe the cochlea, electrode array and biophysical interface for a specific individual. Such models can be used to investigate performance variation among different cochlear implant (CI) users.
It is a laborious process to create custom computational models of individual CI users' cochleae.
Therefore, if user-specific models were to be translated from a primarily research tool to a clinical setting where they can be applied as part of the maintenance protocol for CI users, there is a need for a method that would allow rapid generation of user-specific models.

1.1.2 Research gap

While some automation of selected portions of the model generation workflow has been presented (Rodt et al., 2002, Wang et al., 2006, Erixon et al., 2009, Noble et al., 2011, Agrawal and Newbold, 2012, Reda et al., 2013, Aneja et al., 2015, Tran et al., 2015, Hanekom and Hanekom, 2016, Malherbe et al., 2016, Gross, 2017), no single turn-key solution, that includes user-specificity, exists for the development of 3D computational models of the cochlea. Studies that require the use of 3D computational models have a model development stage that is often very time-consuming as it relies on various levels of automation and manual techniques to convert anatomical data into 3D geometric entities for simulation purposes (Wang et al., 2006, Malherbe, 2009, Tran et al., 2015). Studies tend to focus more on the results obtained from 3D computational models of the electrically stimulated cochlea and not on the actual methods of model development in terms of an automation point of view (Yoo et al., 2000a, Yoo et al., 2000b, Rodt et al.,

2002, Wang et al., 2006, Hanekom and Hanekom, 2016). The investigation and development of automation techniques for each of the various model development phases involved in 3D model development will ultimately aid the development of an automated method to create a 3D model of an electrically stimulated cochlea.

1.2 RESEARCH OBJECTIVE AND QUESTIONS

The following research questions were defined for the development of an automated 3D cochlea and cochlear implant computational model generator.

- Is it possible to develop an automated landmarklandmarking tool that is ultimately able to identify and outline landmark points that define the cochlea and the implanted cochlear electrode array from anatomical data source images?
- Is data fusion required to define anatomical data sets such as the cochlear spirals that represent the cochlea and the cochlear implant?
- Will an automated model generator provide similar results when compared to manual methods?

Following these research questions, the study aims to assess the viability of an automated 3D cochlea model generator with the objective to expedite translation of the models to clinical application.

1.3 APPROACH

The hypothesis is that if the various model development phases can be automated, 3D user-specific models could be generated faster than what can be achieved with manual methods. This study will explore the development of automation techniques for each of the model development phases, with the objective to firstly determine the feasibility and viability of an automated 3D cochlea model generator and secondly to assess the geometric integrity of the resulting models.

By deconstructing the main research questions, the following goals can be set.

- Select an appropriate data source and develop a method to convert images to a specific required resolution and physical image dimensions, format and colour scale.

- Investigate and/or develop a technique that automatically identifies specific landmark points that outline the shape of a cochlea and the various structures that make up the cochlea from cross-sectional imagery.
- Develop a technique that evaluates the extracted data and applies data processing techniques to smooth data in order to remove unwanted discrepancies caused by image noise, such as excessive electrode artefact, without compromising the validity of the model. This technique will also involve data fusion where necessary. Such data fusion techniques involve a similar approach as followed by Malherbe et al. (2015), where extracted landmark data are compared to a database of cochlea templates to find the best match and extrapolate the data based on this match.
- The smoothed data must be validated before any further model development phases can continue. The study must validate the data by means of comparison of the dimensions reported in the literature. A comparison algorithm must be developed to determine if the data is valid when the comparisons between the calculated and physical dimensions yield a value lower than a specific set tolerance.
- After validation, the data must be converted to a specific x, y, and z coordinate system to define the cross-sectional faces of the various cochlear structures and the cochlear spirals that act as guide paths.
- The converted data sets must then be imported to software such as SolidWorks or COMSOL through which the respective geometries must be created and combined, if possible, to construct the specific cochlear model. This model must then be converted to a specific file format that is readable and able to be exported to multiphysics software such as COMSOL.
- Once the automated measurement and model development phase is complete, the measurements and models resulting from the automated process must be compared to model predictions from the manually generated models. The method and model accuracy can be established based on a comparison between the relevant model predictions.

1.4 RESEARCH CONTRIBUTION

The primary objective of this study is to support the translation of computational models of the electrically stimulated human cochlea to clinical tools, such as model-based diagnostics (MBD) and model-predicted mapping (MPM) (Malherbe et al., 2013, Malherbe et al., 2015, Malherbe et al., 2016, Gross, 2017). If these tools were to become part of the management protocol of implant users, rapid model generation techniques are required to make the resource available to larger numbers of implant users. The outcomes of the study will thus decrease the time required for user-specific model development. The automated model generation approach may also allow for consistent identification and quantification of landmarks, which in turn, will remove measurement variations among human observers, which could affect model predictions. Such an automated 3D model development tool would also lay the foundation for future expansions of cochlear models to include further anatomical detail.

1.5 OVERVIEW OF STUDY

This dissertation is divided into five chapters.

- Chapter 1 serves as an outline to the study and describes the background, research problem, and approach.
- Chapter 2 presents a literature review on computational modelling methods relevant to the automated reconstruction of the 3D geometry of the cochlea and cochlear implant electrode.
- Chapter 3 presents the methods applied to develop the automated model development strategy.
    - Section 3.2.1 presents the first step in the automated model development strategy; i.e. the development of a knowledge-based landmark detection algorithm (KBLDA) to enable the detection and extraction of cochlear landmarks and electrode pathways for a specific user. The method was applied to the existing CT scans of three users with bilateral CI's. The landmarks detected by the KBLDA were validated by comparing them to manually measured landmark data.

  - In section 3.3.8, the next step in the automated method is described where the landmarks detected by the KBLDA were used as a geometric basis for the construction of a 3D model of an electrically stimulated cochlea. This was achieved by fitting a template 3D cochlea framework to the measured landmark spirals. Finite element modelling (FEM) software was used to create a mesh and determine the electric potential distribution inside an electrically stimulated cochlea. Existing models, created through a manual process, were used to compare and validate the potential distributions obtained from the automated method models.

- In Chapter 4 the outputs of each automatically and manually generated model pairs originating from the same image data set are compared as validation for the use of automated models. The activating function (Rattay, 1989) was employed to give an initial indication of the nerve fibre excitation patterns predicted by both manually and automatically generated models. Comparing the manual and automated methods' predicted activating functions, aided in validation of the models created with the automated method.
- Finally, in Chapter 5 the findings of the study are discussed and summarised and conclusions are drawn with regard to the accuracy, effectiveness and validity of the automated method

Figure 1.1 provides a diagrammatic summary of the approach taken in this study while **Figure 1.2** contextualises the work within the broader field of cochlear implants.

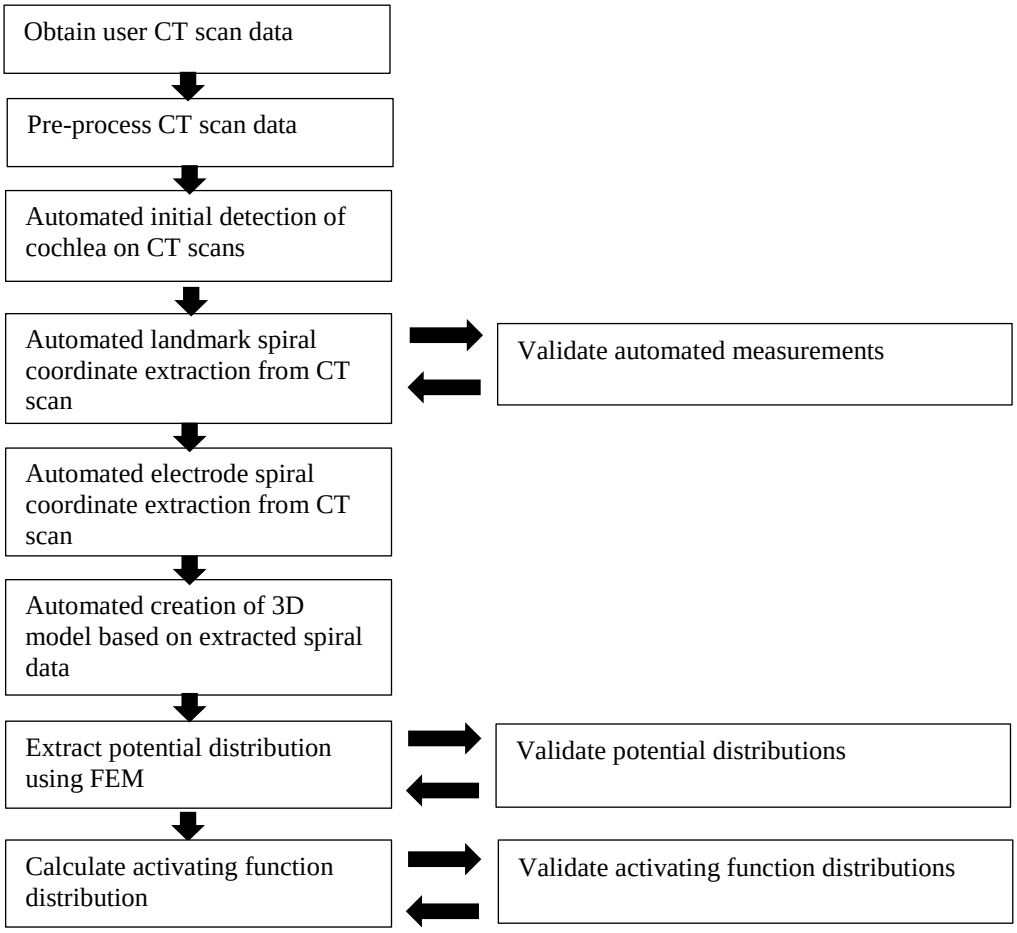

Figure 1.1 – Overview of the approach taken to conduct this study

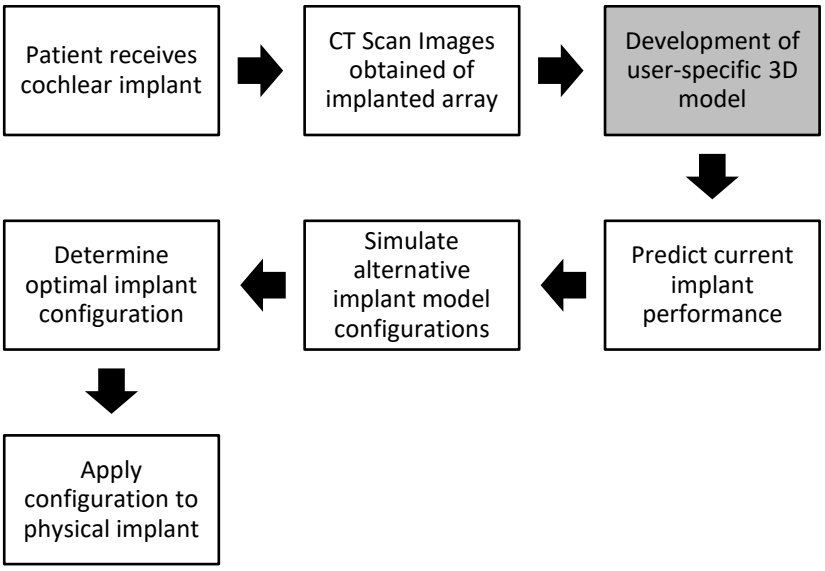

Figure 1.2 – Contextualisation of the study (grey block) within the broader field of cochlear implants

CHAPTER 2 LITERATURE STUDY

2.1 CHAPTER OBJECTIVES

The objective of this chapter is to present an overview of the literature regarding the development and automation of 3D computational models of the *live*, electrically stimulated human cochlea. The 3D computational model development workflow is discussed in order to establish the requirements for the development of such models, the methods used to create such models, and the level of automation that such methods currently offer.

2.2 THREE-DIMENSIONAL MODEL DEVELOPMENT WORKFLOW

Cochlear implants have changed the lives of many individuals who suffer from severe hearing loss as they provide such individuals with the ability to perceive sound after they became deaf or showed signs of severe hearing loss.

It must be noted that it is still not possible to predict how much a user will benefit from an implant. Knowing how a cochlea fitted with a CI works, and understanding which processes are involved in electric hearing, could allow researchers to identify crucial parameters for such prostheses. For this reason, researchers have been focusing on the development of 3D computational models since as early as 1987 (Girzon and Eddington, 1987). Computational models create a non-invasive means to study the details of the biophysical interface between the electrode array and the auditory neurons, typically by predicting potential distributions and neural excitation patterns of the electrically stimulated cochlea (Frijns et al., 1995, Agrawal and Newbold, 2012). These models not only provide insight into the workings of the implanted cochlea, but also have the additional benefit of allowing researchers to investigate a variety of experimental conditions and setups that may either not be feasible in a live user, or would take an

excessive amount of time to investigate in live users. Computational models may thus also remove the risk of harming a user during the search for possible solutions to problems associated with cochlear implantation. A simple example of using 3D models is the assessment of different electrode designs in a specific user and how these designs could prevent unwanted facial nerve stimulation (Gross, 2017).

Since the development of the earliest models, the level of detail has increased to include user-specific characteristics such as electrode trajectories and variations in cochlear size and shape among different individuals (Noble et al., 2011, Agrawal and Newbold, 2012, Malherbe et al., 2013, Malherbe et al., 2015, Tran et al., 2015). This increase in the level of detail is facilitated by the increase in computational power and the methods with which anatomical data is captured.

Simulations that utilise 3D reconstructions of structures are often divided into three main workflow phases or steps, which make up the model development procedure. These workflow phases are (i) data collection from anatomical data sources, (ii) data analysis and processing, and (iii) model geometry construction.

2.2.1 Workflow Phase 1: Collecting geometric data from anatomical sources

The quality of geometrical data is vital to any study as the answers that scientists seek lie hidden in the data used during the study. The accuracy of such data is imperative, as inaccurate data may lead to a false representation of a structure in a 3D computational model. There is a great deal of variability in anatomic features amongst different cochlear implant users (Erixon et al., 2009) and therefore, it is vital to capture these specific variations through the use of accurate anatomical data sources. The development of 3D computational models for cochleae and cochlear implants make use of image data obtained from three main sources: X-rays, digital photography of physically sliced anatomical structures, and computed tomography (CT) or come beam computed tomography (CBCT) scans.

2.2.1.1 Imaging of the cochlea and temporal bone through X-rays

The X-ray is one of the oldest imaging technologies used for medical purposes. Medical X-rays are used to produce radiographs by means of positioning the user in such a way that the part of the body required to be imaged is between the source of the X-ray and the X-ray detector. X-rays then travel through the body and are absorbed by the different tissues in the body. Depending on the radiological density of the tissues, the tissues appear as different degrees of greyscale colours.

Whilst able to capture anatomical data of the cochlea, the two-dimensional nature of X-rays does not allow for 3D interpretation of the data (Yoo et al., 2000b) and is not suitable to create a 3D cochlear model containing an implanted electrode array.

2.2.1.2 Imaging the cochlea using Serially Sectioned Imagery (SSI)

Among the various anatomical data sources available, serially sectioned images have been used in studies that involve 3D computational reconstruction of anatomical structures that make up the cochlea and the surrounding anatomy. An example of serially sectioned images are those images obtained from the Visible Human Project (VHP) (Tran et al., 2015). The sectional data captured in this way involves physically slicing the bodies of deceased individuals into small slices, with intervals between the slices of 1 mm to 0.33 mm. For studies involving anatomical structures with small dimensions (less than 0.6 mm), e.g. the cochlea, scientists prefer to use 0.33 mm datasets, which allow for better definition and representation of these structures (Erixon et al., 2009).

Because of the high resolution of the serially sectioned images, such imagery is well-suited to be used as a source of anatomical dimensional data; allowing scientists to distinguish among different anatomical structures in order to create 3D models with finer detail. One of the drawbacks to this technique, is the image pre-processing that is required to remove background colours created by the gel used to preserve the specimens. As such, background detail is known to negatively affect the accuracy of semi-automatic segmentation techniques (Tran et al., 2015). Although providing a higher level of detail,

this method of capturing geometric detail is an invasive procedure, which can only be used on deceased users.

2.2.1.3 Imaging of the cochlea and temporal bone through CT scans

Computed tomography (CT) is an imaging technique that is similar to the imaging technique of X-rays. However, CT scans differ from X-rays as they allow for the 3D interpretation of image data. In summary, a CT scan is an imaging technique that aims a narrow beam of X-rays at a patient. In summary, a CT scan is similar to an X-ray in that it aims a narrow beam of X-rays at a patient. Materials that make up the scanned section of the body, each absorb or reflect different levels of X-ray energy. These different levels of absorption are then captured by a detector and converted to a digital image. What sets a CT scan apart from an X-ray image, is that this narrow X-ray beam can be rotated around the patient, which then creates a series of sectional images through computational processing (Herman, 2009). These sectional images can then be combined to allow for the 3D reconstruction of anatomical structures.

More studies have shown to favour CT scans as a source of geometric data for the cochlea (Rodt et al., 2002, Rau et al., 2013, Bellos et al., 2014) as opposed to medical X-rays or serially sectioned imagery. This is due to the technological advances such an imaging technique which affords the researcher the ability to non-invasively capture 2D sectional data from multiple user-controlled angles of a living individual. Two main drawbacks to this technique are the poor resolution of the CT imagery, and artefact produced by metal objects such as electrode contacts. Both these drawbacks reduce the visibility of internal cochlearstructures as well as increase the difficulty to distinguish between the various internal structures (Wang and Vannier, 1998, Yoo et al., 2000a).

The benefits of CT scan imaging far outweigh the drawbacks mentioned above, since CT scan imaging can be applied with little effort within a rapid 3D model development protocol. For this reason, CT scans were used as the primary source of anatomical data in this study.

2.2.2 Workflow Phase 2: Data Interpretation and Processing

The next phase in the development of 3D computational models is data processing and analysis. After manually obtaining anatomical data from a variety of sources and methods available, the researcher is often left with a vast amount of raw data. The raw data usually contain measurement noise as a result of (i) the finite accuracy with which an observer can identify a landmark (intra-observer measurement noise), (ii) variability in identification of a landmark among different observers (inter-observer measurement noise) typically because of variable levels of experience, and (iii) poor visibility of anatomical structures if a low-resolution source such as a CT image is used. The outliers in the data are removed to create a smoother set of data points (Malherbe, 2009) .

The interpretation and processing of the data provided by anatomical data sources in the present study is primarily achieved through a combination of two methods known has *sectioning* and *helico-spiral approximation*, as discussed in the subsequent sections.

2.2.2.1 Sectioning

Sectioning is a technique where a digital image of a view plane through a structure is obtained upon which the colour properties of each pixel are evaluated. Pixels with similar properties are grouped together to form different sections. These grouped sections represent different anatomical structures to which material properties are assigned. Sectioning was utilised in a recent study, which explored the computational 3D reconstruction of the head of a deceased individual implanted with a cochlear implant (Tran et al., 2015). The sectioning method employed software such as ScanIP to combine sections into the different geometries that constitute the anatomical structure involved in the study. The technique described by Tran et al. (2015) is very time consuming since it has to be performed either manually, or by built-in semi-automatic segmentation tools that form part of the software used. Although the method offers great potential to accurately define numerous anatomical structures, it is not fully automated, thus increasing the duration of such a study.

Alternative sectioning methods were introduced through the use of software such as Amira (Wang et al., 2006). Similar to the Tran et al. study mentioned above, this study relied on

the use of a high-resolution data source, i.e. sectional histological data. The histological slides were first photographically digitised, after which the resulting colour images were converted to a specific greyscale range. The image processing software package Amira was then used to outline and define the specific anatomical structures. The software allowed for the alignment of consecutive slides, as well as automatic and semi-automatic tools for sectioning of the majority of anatomical structures. In the case of cochlear implants, the Amira software programme is able to section the majority of the anatomical structures that make up the cochlea, except for the basilar membrane and the endolymphatic sac (Wang et al., 2006). Such small structures require manual sectioning. Amira also allows the user to perform surface reconstruction through polygonal surface model generation, as well as a smoothing algorithm applied to these surfaces to remove unwanted vertices. Although this method made use of the semi-automated functions available in Amira, it was time-consuming and expensive as the study by Wang et al. (2006) spent 2-3 months primarily focussing on surface generation and smoothing.

The methods proposed by both the Tran and Wang studies use high resolution anatomical data sources, i.e. serially sectioned imagery, to increase the visibility of finer anatomical structures and thus the accuracy of the model representation of the cochlea and temporal bone. While the Tran and Wang studies were based on high-resolution images from cadavers, this method (sectioning) may also be applicable to lower-resolution data, such as CT image data. By applying such a method to CT scans could allow the user to better distinguish between the outer boundaries of the cochlea.

2.2.2.2 Helico-spiral approximation

The helico-spiral approximation is a method where a helical spiral is used as a model for the spiralling structures of the cochlea. In the study by Yoo et al. (2000b), the technique was implemented in the image analysis and visualization software package Analyze. The authors used a combination of the *growing method* and *thresholding* on CT images of the human cochlea to segment the cochlear canal, starting at the round window. The centre of masses of the cross-sectional segmented cochlear canals were combined to form a curve,

known as the central path. The data was then fitted to an Archimedean helico-spiral model to serve as a framework for measurement data for cochlear features (Yoo et al., 2000a). Similar models were later adopted (Yoo et al., 2000b) based on Fowler's model (Fowler et al., 1992), which is a helico-spiral sea shell model that was used to represent the human cochlea. Two processing steps from the Yoo et al. (2000b) study are relevant to the present study; i.e. (i) compensation for the orientation of the human head and cochlea as the cochlear tilt does not remain constant among individuals, and (ii) smoothing of data point measurements to eliminate measurement noise.

Another technique based on helico-spiral approximation and that is used in 3D reconstruction studies, is Landmarking. This technique often involves intensive initial manual data interpretation, after which a semi-automated process allows further data processing. The manual phase of the technique involves the identification of specific points, i.e. landmarks, on the boundaries of the anatomical structures that make up the cochlea as captured from CT and µCT scans. Following the primary identification of landmarks, the data were smoothed and interpolated through curve fitting of third order cubic splines (Malherbe et al., 2013, Malherbe et al., 2015, Malherbe et al., 2016). The smoothed data set was compared to 11 template cochlear spirals obtained from the literature (Erixon et al., 2009) to determine the best fitting template through a Procrustes superimposition. The best fitting template was used to create a 3D reconstruction of the cochlea, consisting of combined individual cochlear structures. (Malherbe et al., 2013). These data sets have also been used with Finite Element Method (FEM) software through integrated programming software such as COMSOL and Matlab, to allow for direct model reconstruction and subsequent simulation of the effects of electrical stimulation.

Although the method applied by Malherbe et al. (2013) has been successfully applied to produce a 3D computational model of the cochlea from lower-resolution clinical images, it requires a considerable level of manual input from the initial landmarking procedure as a result of image noise and landmark visibility. The present study will use and extend on this method, since it aims to automate the model generation process for live CI users for which clinical imaging is the only available anatomical data source. The use of this method not only enables the extraction of landmark data from CT scans, but also allows the use of

such landmark points to estimate the geometrical properties of smaller cochlear structures to create higher detail cochlear models.

2.2.3 Workflow Phase 3: Model Geometry Construction

The final stage in the development of 3D models involves the construction of the 3D geometric description of the anatomical structures from the various sets of landmark data. Three software packages were explored in terms of applicability and capability in the 3D reconstruction of anatomical structures.

2.2.3.1 SolidWorks

SolidWorks is a powerful 3D design software package that provides the user with design tools and solutions such as various drawing capabilities for parts, as well as the ability to create an assembly of separate parts (Solidworks.com, 2015). The software further enables the user to construct different geometries from macros, which can be imported in a specific format.

SolidWorks also allows the user to import existing 3D structures from other 3D software packages to explore and adapt the geometries of such models, as was done in a study where SolidWorks was used to perform virtual fitting of implantable devices in the mastoid cavity (Handzel et al., 2009). For this study, SolidWorks would allow data sets that describe the various spirals and cross-sectional faces of cochleae and cochlear implants to be imported in order to construct the various geometries that make up the cochlea.

2.2.3.2 Amira

Amira is an image processing software package used in the development of 3D models. The programme is well suited for the semi-automatic creation of 3D models from digital imaging output files such as CT scans, or other forms of digital photography. The programme also allows for the application of selection and segmentation tools (Wang et al., 2006).

In the field of 3D cochlear model construction, Amira has been used in studies that involved the identification of the most optimal cochleostomy site for cochlear implant

surgery by making use of a 3D model of the hook region and round window of a human cochlea (Li et al., 2007). The use of Amira has also aided in the development of a 3D model that investigated the mastoid cavity dimensions and temporal bone implant fittings (Handzel et al., 2009).

Software such as Amira allows the user to convert imaging data, such as CT scans, directly into a 3D model by enabling the user to select, define and combine sectional data through semi-automated built-in processes.

2.2.3.3 COMSOL with MATLAB Integration

COMSOLis a multiphysics finite element modelling and simulation software package that can be used to construct and solve 3D models of the cochlea as was achieved by Malherbe et al. (2013, 2015, 2016). The software allows the user to integrate the features of COMSOL with MATLAB. By utilising such a feature, the user is enabled to construct complex 3D models. Malherbe et al. (2013, 2015, 2016) used custom Matlab code to firstly perform data pre-processing such as smoothing, and then to generate separate 3D geometric representations of each of the anatomical structures that make up the cochlea and the cochlear implant electrode array. Each of these geometries was then imported into the same simulation domain in COMSOL in order to establish the complete 3D domain in which further analysis could be performed.

The use of COMSOL and MATLAB for 3D model reconstruction allows the user to specify exactly how the input data points must be combined in order to create the various 3D geometries. Once the geometries have been imported in COMSOL, the volumes can be meshed for subsequent finite element analysis.

2.3 AUTOMATION OF MODEL DEVELOPMENT STRATEGIES

Various automation methods have been used to reduce the time spent during detection and measurement of anatomical structures, with the aim of achieving a specific level of accuracy. These methods are applied to various fields of anatomy feature detection, some of which could be applied to the detection of cochleae and cochlear implants.

2.3.1 Image registration

Image registration relies on the use of reference images, otherwise known as source images, which are compared or aligned with target images to determine similarities and differences among source and target images. This method has been used for the automated detection of landmarks and anatomical features. A study done by Shahidi et al. (2014) utilised image registration techniques to detect craniofacial landmarks by designing software in MATLAB, which combine voxel and feature similarity-based methods. Other studies have utilised image registration of pre- and post-operative CT scans for the automatic segmentation of the internal structures of cochleae and intensity-based techniques to add the electrode array to the segmented internal structures (Reda et al., 2013). The intensity-based technique is used to optimise mutual information between images (Reda et al., 2013). This method is, however, limited to including only the scala vestibuli, spiral ganglion nerve bundles, and the scala tympani as internal structures in the cochlea. The study by Noble et al. (2011), employed image registration to automatically segment the scala tympani and the scala vestibuli with μCT scans as training or reference data sources. The segmentation data were then used to construct an active shape model (ASM) for the two internal structures. An ASM consists of a statistical model shape that iteratively changes to fit to a specific object on an image. Through the use of non-rigid image registration techniques, the ASM is driven to find an accurate solution. This method, however, only included two of the several internal structures of the cochlea, the scala tympani and the scala vestibuli, due to the low resolution of conventional CT scans, which are unable to provide sufficient information on the smaller internal structures of the cochlea. An additional automated landmark detection method that also follows a similar approach to that of image registration was investigated in the study by Sari et al. (2015). In their study, they utilised template matching methods combined with normalised cross-correlation measurements of similarity for cephalostat detection. To use this method to create user-specific models, pre- and post-operative CT scans would be required. However, pre- and post-operative scans are not always available for every user; thus creating difficulty in applying such a method.

Similar to ASM, a statistical shape model (SSM), where a set of points represent each shape in a common coordinate system, is another approach to construct the geometry of 3D computational models. This method involves manual segmentation of an anatomical structure, such as the cochlea, from a set of high resolution data sources. This type of approach is seen in the study of Mangado et al. (2016), aimed at the automatic generation of a computational model of cochlear implant surgery. The study used μCT scans from 17 users from which an average surface model of the cochlea was constructed. The method assigned various weights to known variations of the main modes of the model in order to remove the risk of highly deformed or unrealistically shaped models of the cochlea being formed. Through the use of image registration between clinical CT datasets and the SSM, an anatomical shape prediction can be made of the users' cochlea, through the adjustment of the various points that define the SSM. After establishment of the person-specific cochlea surface model, the implant electrode array is virtually placed within the cochlea model in order to create a realistic model of the users' implanted cochlea (Mangado et al., 2016). For the present study, SSM's show the benefits of data fusion as this study will make use of a cochlear template, containing a greater level of internal structure detail, which will be adapted to user-specific data.

2.3.2 Knowledge-based landmark detection

Automated model development strategies also extend to a method known as knowledge-based landmark detection. The knowledge-based landmark detection method approaches the automated landmark detection problem through the use of predefined or pre-agreed definitions of the landmarks. These definitions are integrated into an algorithm to automatically detect the landmarks. A method such as this is dependent on the anatomical knowledge of the particular landmark being searched for. A study done by Gupta et al. (2015) developed a knowledge-based landmark detection algorithm to detect cephalometric landmarks on a 3D level. This method proved to be more accurate in their study than other registration-based methods at that time. Additional studies, such as a study done by Aneja et al. (2015), utilised a type of knowledge-based detection algorithm

to detect 17 landmarks on mouse mandibles by means of incorporating information, such as landmark characteristics, into mathematically defined criteria.

Of the three automation techniques discussed, the knowledge-based landmark detection method reported the highest level of accuracy; i.e. as high as 90.33% (Gupta et al., 2015). While this method has not yet been applied to cochlear implants or the development of such models, it could prove to be effective as it not only enables the automation of landmark detection but maintains the accuracy of such automated measurements.
This study aimed to combine the benefits of sectioning, when applied to CT images, with knowledge-based landmark detection in order to develop an algorithm that is able to detect, extract and construct user-specific geometric 3D computational models.

2.4 SUMMARY

The literature study evaluated the various steps involved in model development and the techniques applied to automate the development of such models. For the study at hand, a combination of intensity-based segmentation and landmark-based helicon-spiral approximation will be utilised in order to extract geometrical information from conventional CT scans. To automate the process, a knowledge-based landmark detection algorithm will be developed to automate the process of 3D cochlear implant model development with the added support of MATLAB and Amira software integration.

CHAPTER 3 METHODS

3.1 CHAPTER OBJECTIVES

This chapter discusses the methods applied in order to automate the model development strategy for cochleae implanted with a CI electrode array.

The model development strategy on which this study is based requires a substantial amount of manual processing (Malherbe et al., 2016). The observer must manually digitise the most lateral, most superior, and most inferior landmarks of the cochlear duct on 360 CT scans, resectioned at one degree intervals around the modiolus. The raw landmark coordinates are subsequently processed. Data processing involves smoothing, rotation of the cochlea, data fusion through template matching, template interference removal, and 3D volume construction and combination. This manual method is a time-consuming, laborious process that demands significant effort.

The development of 3D computational models can be divided into two main bodies of interest, i) the cochlea and ii) the electrode array. The aim of this chapter is to discuss the methods applied to detect, extract and recreate the two main bodies from CT scan images. This chapter will discuss how each of the two main bodies were detected, extracted and recreated in a 3D computational model in an automated manner.

3.2 DETECTING, EXTRACTING AND RECREATING THE COCHLEA

3.2.1 Knowledge-based landmark detection algorithm

The foundation on which automated detection of the cochlea is built, is known as a knowledge-based landmark detection algorithm (KBLDA). The use of this method relies on known information of geometric features of the cochlea and the application of this knowledge to detect other cochleae.

The algorithm behind the automated model generation work flow is depicted in **Figure 3.1** and **Figure 3.2**. The algorithm requests several functions, built-in or newly-developed, in a specific order, subject to specific criteria and conditions being met. The paragraph number where each of the steps involved in the algorithm is discussed in the diagram below.

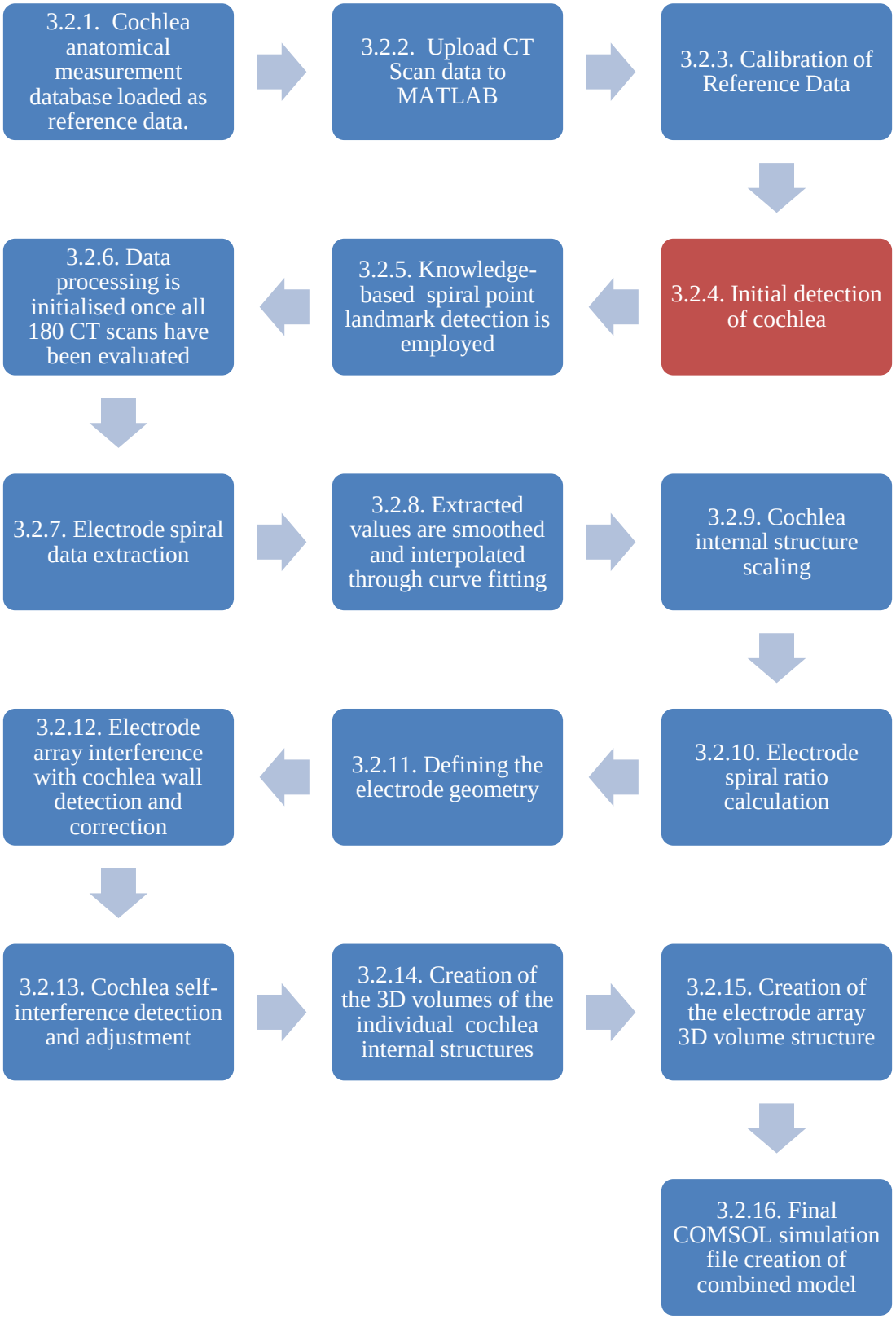

Figure 3.1 – Flow diagram of the systematic series of events followed in the KBLDA.

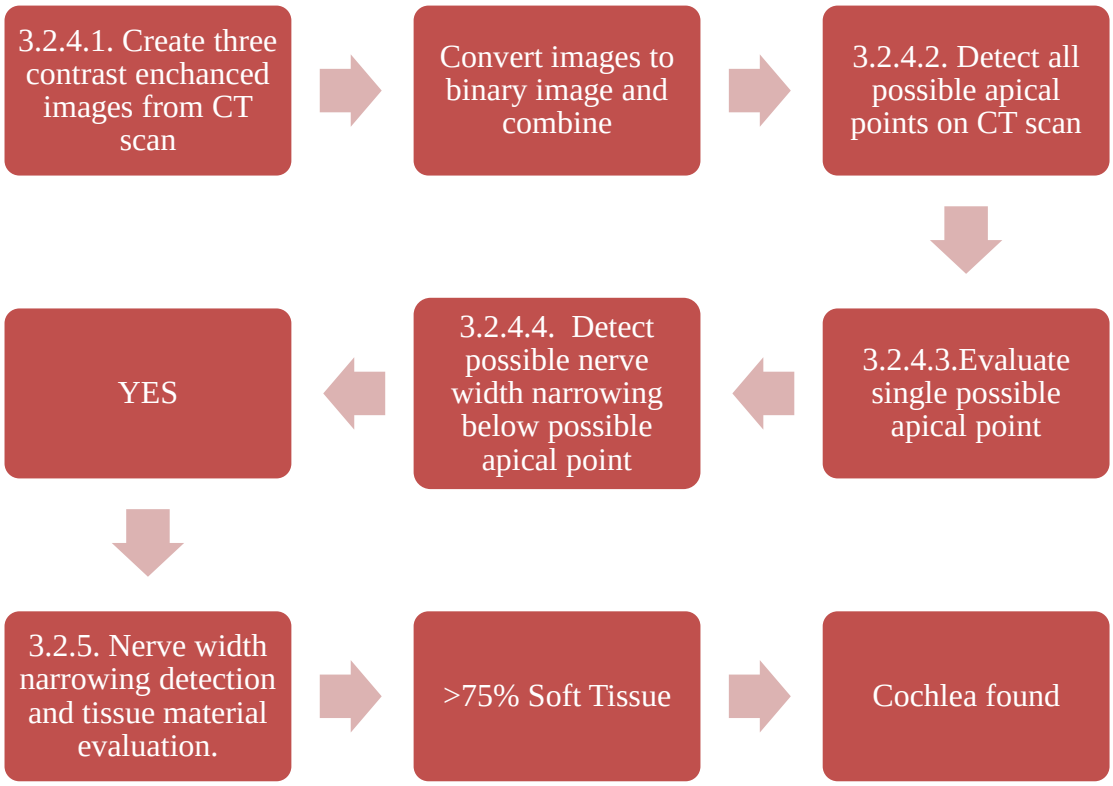

Figure 3.2 – Flow diagram of the systematic series of events followed in the section 3.2.4 of the KLBDA.

3.2.1.1 Cochlea anatomical measurement database loaded as reference data

As the KBLDA relies on knowledge of the cochlea and its geometric features, it demands a type of knowledge database. This knowledge database quantifies the characteristics of specific landmark points and defines the search features to find these landmarks in image datasets of cochleae. The database used in this study is defined by statistical data captured in the anatomical measurements of 15 cochleae. For each of the 15 cochleae, the most lateral, most superior and most inferior points on the outline of the cochlear duct were measured at 5 degree angular intervals around the modiolus. The radius and height of each point was measured relative to the most apical point of each of the respective cochleae. The average radius and height was determined for each angular interval value among the 15 sample cochleae. These values were then stored in a dataset of three matrices, which

served as the knowledge database. Refer to Addendum A for a more detailed description of equations applied.

3.2.1.2 Upload CT Scan data to MATLAB

Before one can detect any of the main bodies of interest, a data source that needs to be evaluated is required for the cochlea. For the present study, CT scan images are the main data source from which a model is to be constructed. The CT images used in this study are the same images that were used in the study performed by Malherbe et al. (2016). Those CT images were obtained with a Siemens Sensation Cardiac 64 CT Scanner (Siemens, Munich, Germany) with a 120 kV tube voltage, 112 mA tube current, and a slice thickness of 0.6 mm. As a result of the low resolution of the conventional CT scanner (0.6 mm voxel size), the quality of the cochlear images was relatively low. The Malherbe study resliced the images radially around the modiolus, the centre of cochlea, in 1˚ increments, which gave a set of 360 mid-modiolar images. The study only used the first 180 mid-modiolar images for three main reasons:

- The cochlea cross-section is a mirror view from 180 degrees to 360 degrees.
- Simultaneous measurements were made on both sides of the modiolus on each image.
- To reduce the number of images required to be measured, thereby decreasing the model generation time.

After the data of the knowledge database are loaded, the next step in the model development algorithm in this study is the upload of the user CT scan images. The image is loaded into Matlab which converts the image to a matrix with rows and columns equal to the height (a) and width (b) of the input image, respectively. Addendum A provides a detailed description of equations applied.

3.2.1.3 Calibration of Reference Data

The next step required in the algorithm involves a simple calibration procedure, in which the upright orientation of the reference data is rotated to the same orientation of the cochlea under evaluation. Rotating the knowledge database allows the detection algorithm to detect the landmark points by means of smaller and more accurately located search fields. These search fields are defined as constrained regions in which each of the landmark points are detected amongst the various boundary points.

The user is asked to select the first two lateral, upper and lower spiral landmark points in the basal turn on only two CT scans, at 0˚ and at 90˚. Based on these selections, the reference data is rotated, scaled and translated in order to fit the projected pathway and search field location of each landmark spiral with greater accuracy. **Figure 3.3** depicts the height profile of the reference data before and after rotation, indicating a noticeable difference in how the relevant landmark points change before and after calibration. A cochlea with an upright and vertical modiolus would display a linear relationship between the height of the lateral spiral point and the angular position or angular length; whereas, the rotated cochlea resembles a higher order curve.

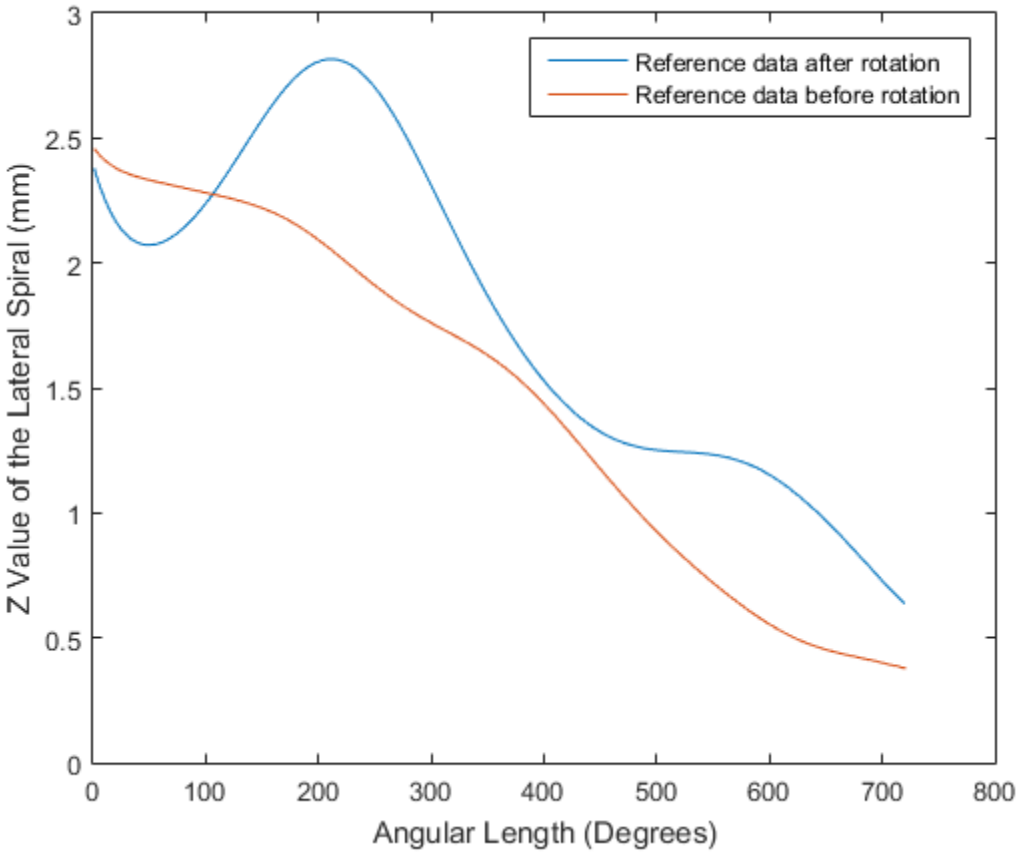

Figure 3.3 – Z-value of the lateral spiral reference data before and after rotation as a result of the manual calibration procedure.

3.2.1.4 Initial detection of the cochlea

Once the reference data and user-specific CT scan images are loaded into MATLAB, the search for the cochlea in the data source can begin. To detect the cochlea, a method was developed to find three main features of a cochlea on a CT scan. These features include the detection of the apical point, the cochlear nerve width narrowing, as well as the evaluation of the tissue material between the narrow nerve width and the apical point.

Create three contrast enhanced images from each CT scan

Slight image enhancement is required at first, as visibility of structures and cochlear walls are limited on each CT scan image. As each image will be converted to a binary image initially, the ability to identify the cochlea boundary becomes crucial. By enhancing the

contrast of the image, the boundaries of the image become more easily identifiable. Since the apical point is the most superior boundary point between the cochlea and the surrounding bone, the conversion of the image to binary allows for improved definition of such a point. The clarity of each image is enhanced by dividing the image into smaller regions, known as tiles, and adjusting the contrast so that 1% of the data is saturated at low and high intensities. By doing so, the bony surrounding of the cochlea is accentuated without significant migration of boundary walls. This technique is only used for initial detection of the cochlea. The image data is used to create three separate images using several built-in functions in MATLAB for image contrast enhancement. A built-in MATLAB image threshold technique, *graythresh*, is utilised to perform an initial form of segmentation based on the grayscale data captured in the images, after which each segmented image is converted to binary image data. Addendum A gives the mathematical formulation of this processing step.

Find all possible apical points on each CT scan image

To find the cochlea on the CT scan, the apical point on each of the CT scans is found by independently identifying all possible apical points through the use of specific point criteria, which apply to the apical point. The apical point, defined as a boundary point, is the point located most superior in the cochlea; therefore, it can be defined as the most superior boundary point. To determine the apical point, specific criteria were created on a binary image. As the apical point can be seen as the most superior point of the cochlea, it can be further described as the most superior boundary point between the cochlea tissue and the bone surrounding the cochlea. By evaluating the apical point as an upper boundary point, the criteria for such a point on a binary image can be defined as follows:

An apical point is defined as a superiorly located binary boundary point with a binary value of 1, with at least 3 points of binary value 0 located directly below that point on a binary image. The x and y coordinates of these points on the CT scan image, identified as possible apical points, are extracted and stored in a matrix. **Figure 3.4** depicts an original CT scan image and the derived contrast enhanced binary image.

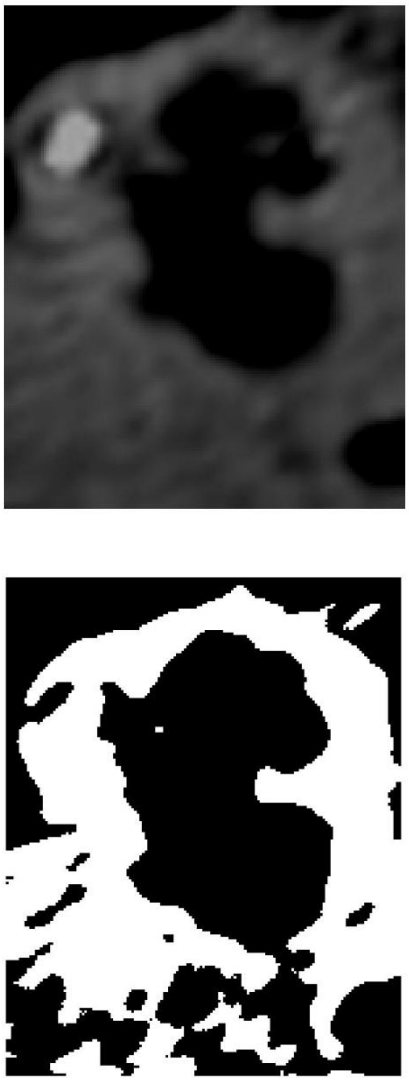

Figure 3.4 – Through the combination of contrast enhanced images the combined binary image (bottom) is derived from the CT scan (top).

The x and y coordinates of all possible apical points are stored in a matrix. **Figure 3.5** depicts an example of the possible apical points of the cochlea, found on a single CT scan image. Refer to Section A2 and A3 of Addendum A for a more detailed description of equations applied.

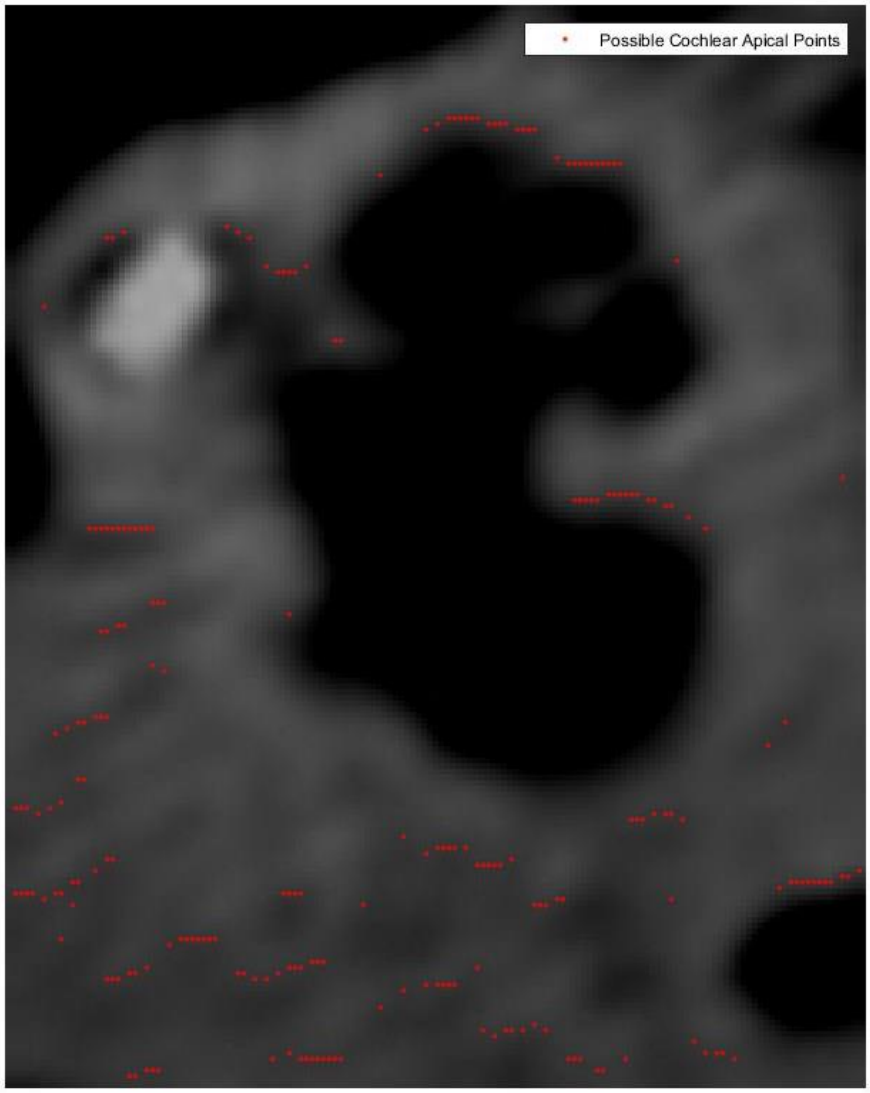

Figure 3.5 – Example of the possible cochlear apical points found on the CT scan.

Evaluate single possible apical point

Once all possible apical points are defined on the CT image, the algorithm continuously filters through these possible points, testing each point for a series of consecutive criteria known as i) the detection of the nerve width narrowing below the apical point, and ii) a check for a majority of soft tissue between the apical point and the nerve width narrowing. These conditions are further discussed in the sections below. If any one of these consecutive criteria are not met at a possible apical point, that point is deemed as invalid and the next possible apical point is tested. The algorithm is designed to continue to test

each point until a point is found that adheres to both criteria i and ii. Refer to Addendum A for a more detailed description of equations applied.

Detect possible nerve width narrowing below possible apical point

The first criterion that a possible apical point must adhere to is the detection of the points at which the minimum nerve width is located. To find these points, the function `nerve_width_detection` was developed in which the mean height of cochleae, as captured in the knowledge database, is used. The data is used to create a search field below the apical point on the contrast enhanced binary image in order to locate the nerve width narrowing of the cochlea. Within the search field, the nerve width narrowing is defined by two boundary points, each on opposite ends of the nerve width narrowing, with the shortest distance between the opposite ends of the nerve width narrowing and a majority of soft tissue between theses points. **Figure 3.6** depicts the data processing workflow procedure followed in this function. Refer to Addendum A for a more detailed description of the equations applied.

Figure 3.6 – Flow diagram depicting the data processing of the developed nerve width detection function.

Evaluate tissue material between possible nerve width narrowing and apical point

The second condition that a possible apical point must adhere to is a majority of soft tissue between the apical point and the nerve width narrowing. This condition evaluates the percentage of soft tissue content between the apical point and the points at which the nerve width narrowing is located. If the percentage of soft tissue between the apical point and the nerve width narrowing is 75% or greater, the second condition is satisfied. The function `soft_tissue_check` was developed to perform this procedure. **Figure 3.7** depicts the logical workflow of how data is handled in this function. Refer to Addendum A for a more detailed description of equations applied.

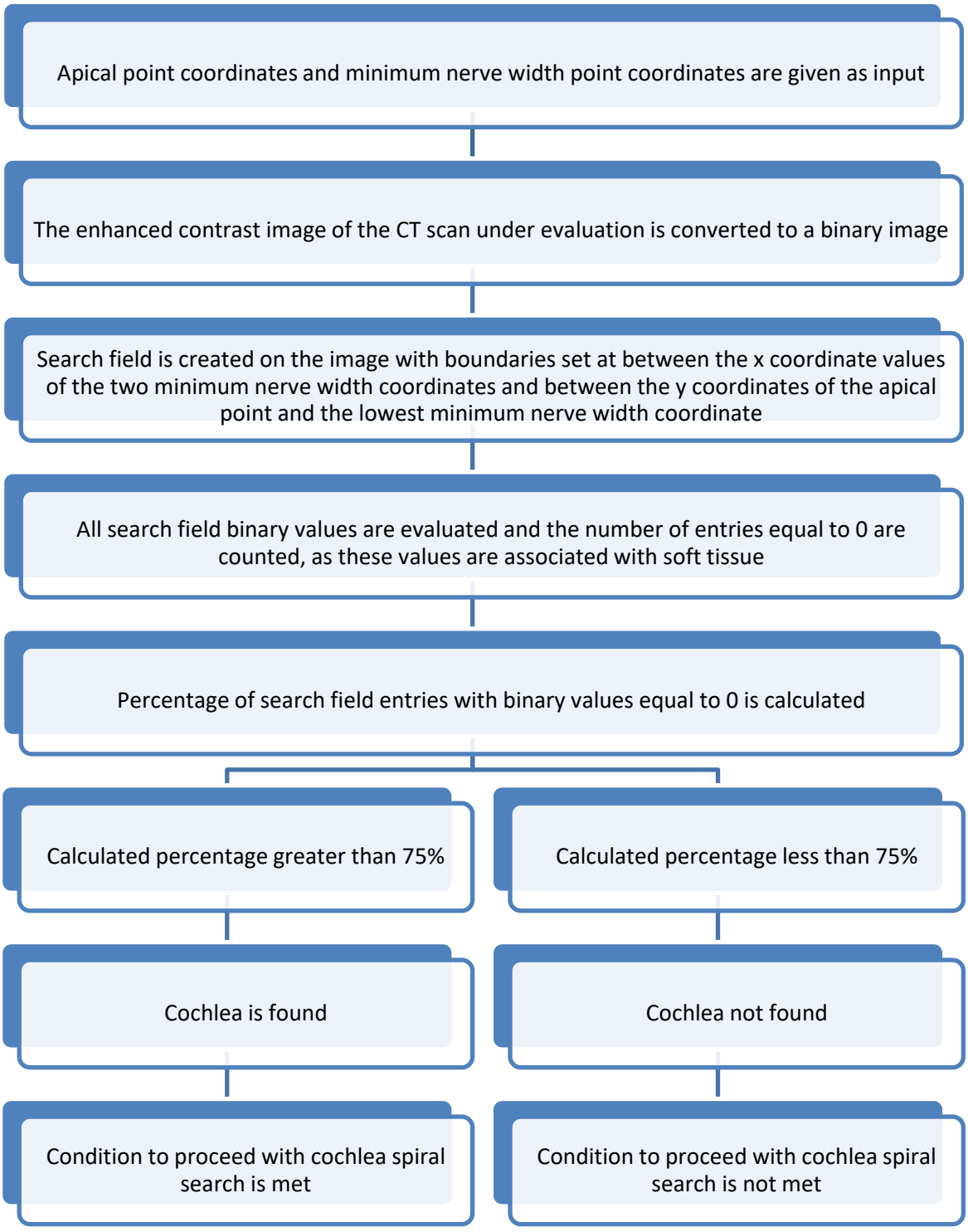

Figure 3.7 – Flow diagram depicting the workflow involved in the developed soft tissue check function.

Once a possible apical point meets all the criteria discussed, the cochlea is considered found and the point is considered as the apical point of the cochlea. This procedure is performed on each CT image slice of the user.

Once the cochlea is found on all CT scan image slices of the user, the mean of the apical point x and y coordinates are calculated and are used for all remaining calculations. The variables x^{apical} and y^{apical} represent the mean x and y coordinate values of the apical point, respectively. The mean apical point serves as the constant point throughout which a vertical centreline, i.e. the modiolus, of the cochlea extends.

3.2.1.5 Detecting cochlear landmarks

With the position of the modiolus calculated, the search for the cochlear boundary wall landmarks is initiated. The cochlear landmarks are detected by means of a KBLDA, while electrode coordinate detection is achieved through an intensity-based image registration technique.

The cochlear landmarks to be found are the most lateral, most superior and most inferior boundary points of the cochlear boundary wall, as depicted in **Figure 3.16**, for both the basal and middle turn on each CT image. These boundary points will subsequently be referred to as the lateral, upper and lower spiral boundary points, respectively.

Cochlear boundary points

As each of the landmark points are seen as a point on the cochlea boundary wall; these points can be defined as boundary points. To effectively find these landmark points, one must first determine all boundary points below the apical point. The function `outline_finder` was developed to determine the boundary points below the apical point. **Figure 3.8** depicts the flow diagram of the `outline_finder` function, which stores all x and y coordinates for each boundary point. Refer to Addendum A for more detailed description of equations applied.

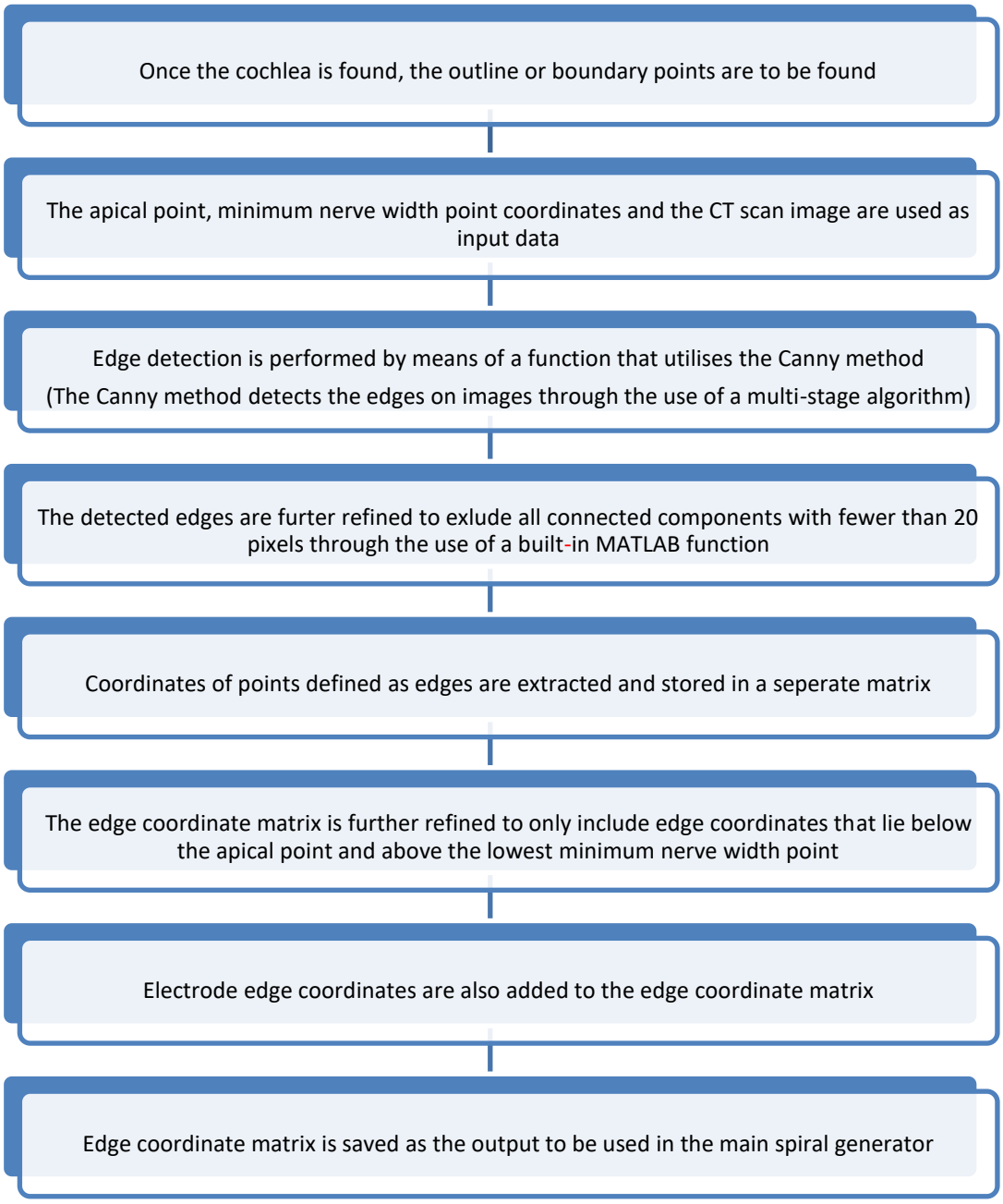

Figure 3.8 – Diagram of the workflow to detect and extract the boundary points on the CT image once the cochlea is found.

This large matrix of boundary points was then further divided into two smaller matrices, one matrix for the coordinates of all boundary points located to the left of the modiolus and the other for all boundary points located to right of the modiolus. In both these matrices, the x and y coordinates are converted to a radius and height value in millimetres,

respectively. This is achieved by calculating the distance between the boundary point and the apical point through which the modiolus extends. Refer to Addendum A for a more detailed description of equations applied.

Search fields for cochlear landmarks

By finding all possible boundary points, a method is required to filter through and determine which of these points are valid landmark points. To achieve this, a search field method was applied. This method acts as a bounded box that searches for each of the landmark spirals at specific locations. The location and size of the search fields are determined by the knowledge database. The initial calibration procedure discussed in section 3.2.1.3 determines the location of the search field on the CT scan below the apical point. The size of the search field, or confining walls, is defined by calculating an error ratio between the boundary points and the reference data for each landmark point, based on the angular interval value of the CT image slice under evaluation. To determine which of the points fall within the search field for the upper, lateral and lower spiral landmarks, limits are defined for the error value between the reference data and the boundary points (landmarks) at the angle of the particular CT slice. This allows only points inside the search fields to be deemed as valid points. If multiple points are found within a search field, the mean coordinate value of all those points are calculated and used as the boundary point value. The error between the reference data and the extracted boundary points are calculated for the basal and middle turn of the cochlea simultaneously on each CT image slice. This is not performed for the apical turn as the lateral, upper and lower spiral points are not typically distinguishable in this turn. By doing so, landmark points can be detected at multiple cochlear turns on each CT scan image.

Figure 3.9 depicts an example of the various search fields on each CT scan as well as the boundary points detected on the CT scan. All boundary points that fall within the relevant search fields are deemed as valid points. As seen in **Figure 3.9**, the middle turn search field for the lateral spiral point, top right green box, does not include the true lateral point, although close neighbouring points are included in the search field. In such a case, the

algorithm will calculate a mean coordinate value amongst the valid points and use that point as the valid point, see section 3.2.1.6.

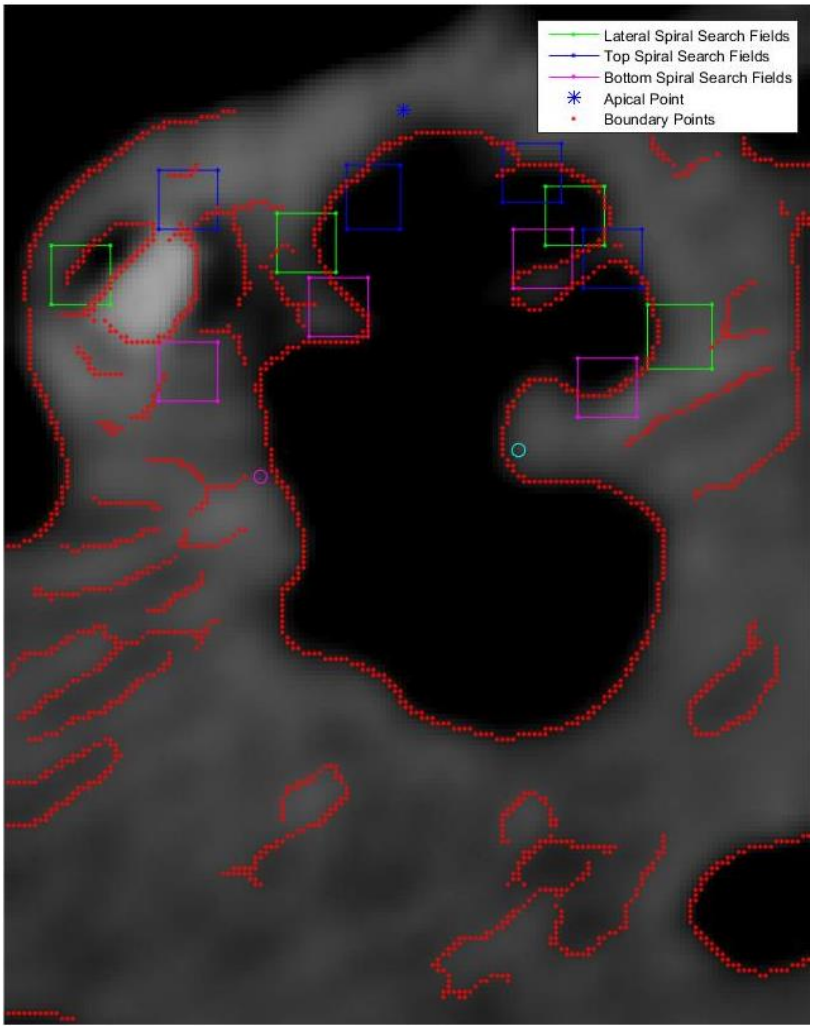

Figure 3.9 – Example of the boundary points detected and the landmark search fields for the relevant landmark spirals.

If no points were found within the small search fields for any of the landmark points of the several spirals, the output is deemed as an invalid point and is assigned a value of [0,0]. Refer to Addendum A for a more detailed description of equations applied.

3.2.1.6 Data processing

When all possible landmark points are detected, extracted and stored for each angular interval CT image, data processing is initiated. The data processing step involves the analysis and refinement of the extracted coordinate datasets as discussed below.

In each of the matrices containing the landmark points, the radius, angular location and height of the landmark point of only the valid points are extracted from the matrices; i.e. the points which are not assigned a value equal to [0,0]. These matrices of valid points are smoothed and interpolated in order to create a continuous set of valid data from the smallest angular position to the highest angular position. The polar coordinates in the matrices are then converted to Cartesian coordinates for ease of use in the development phase. Refer to Addendum A for a more detailed description of equations applied.

3.3 DETECTION, EXTRACTION AND RECONSTRUCTION OF THE ELECTRODE ARRAY

The second essential aspect of the model is the electrode array. The electrode array also follows a user-specific pathway through the cochlea, which cannot simply be predicted through the use of a knowledge database. The electrode array trajectory for each individual therefore requires meticulous reconstruction.

3.3.1.1 Electrode coordinate detection

As no knowledge database can be used to determine the coordinates of the electrode array, the electrode artefact is utilised. Studies showed that the largest artefact on CT images of implanted cochleae emanates from the electrode array (Braithwaite et al., 2016, Razafindranaly et al., 2016); thus, a method was developed that utilises this artefact as a method to determine the electrode array spiral coordinates. To achieve the simultaneous detection of the electrode array alongside the cochlear landmark spirals, intensity-based image processing functions are used to detect and extract the relevant electrode trajectory data from the CT images. To employ the intensity-based method, the function `electrode` was developed to detect and extract the electrode array trajectory coordinates. **Figure 3.10** describes the data processing stages involved in the detection and extraction of electrode trajectory data.

Figure 3.10 - Workflow diagram followed by the developed function to detect the electrode spiral coordinates.

The CT image under evaluation is segmented through a built-in MATLAB function, *multithresh*. This function performs multi-level clustering-based thresholding on the image. The function assigns the various segments on the image with a specific number associated with a colour, of which a maximum of 21 segments can be distinguished with this function. The maximum number of segments is a predefined number of the built-in function, *multithresh*. The colour number associated with the electrode array and its artefact was chosen to be 19 or higher.

All the segments with a colour number of 19 or higher are then isolated and extracted as separate clusters, with each cluster representing an electrode cross-sectional view.

The centrepoint for each cluster is calculated as the respective mean values of the x and y coordinates of the separate clusters. These centrepoint values are then converted to dimensions in millimetres, with the apical point as reference point, and rearranged and assigned to a raw data matrix. The points are rearranged and assigned according the proximity of each centrepoint relevant to the modiolus. If no electrode point is found on the CT image, a value of 0 is assigned to the x and the y coordinates as these values are associated with an invalid point.

At the point where all CT images have been evaluated for electrode points, all valid points in the matrices are extracted, smoothed and interpolated to create a continuous set of coordinates that represent the trajectory of the electrode array.

To determine the deepest point of the electrode array, i.e. the insertion depth, the number of sections through the electrode array (electrode centrepoints) on each CT image is continuously calculated. The number of sections through the electrode array on an image can range from 1 to 4 as elucidated by **Table 3.1**. The table indicates the angular range and the cochlear turn in which the most apical point of the electrode array is located. This step is required as it aids the user in identification of the electrode tip.

Table 3.1- Angular range in which deepest electrode point is located

Average number of sections through electrode array (centrepoints) per CT scan	1	2	3	4
Angular range of deepest point (˚), i.e. insertion depth	0-180	181-360	361-540	541+
Cochlear turn	Basal Turn	Basal Turn	Middle Turn	Middle Turn
Figure illustration	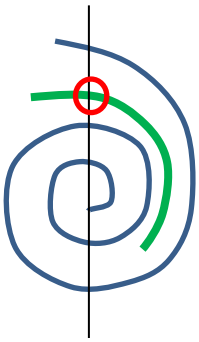	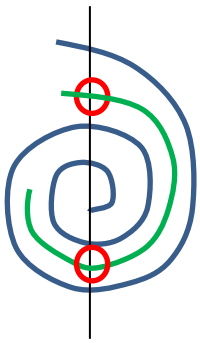	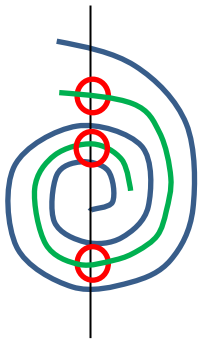	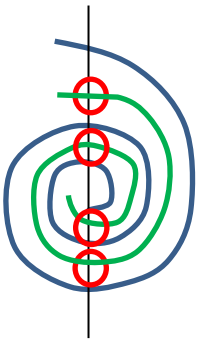
		Electrode array		
		Point of intersection		
		Slice through modiolus		
		Cochlear wall		

An example of the detected electrode points on a CT scan is depicted in **Figure 3.11**, through the use of the above-mentioned method.

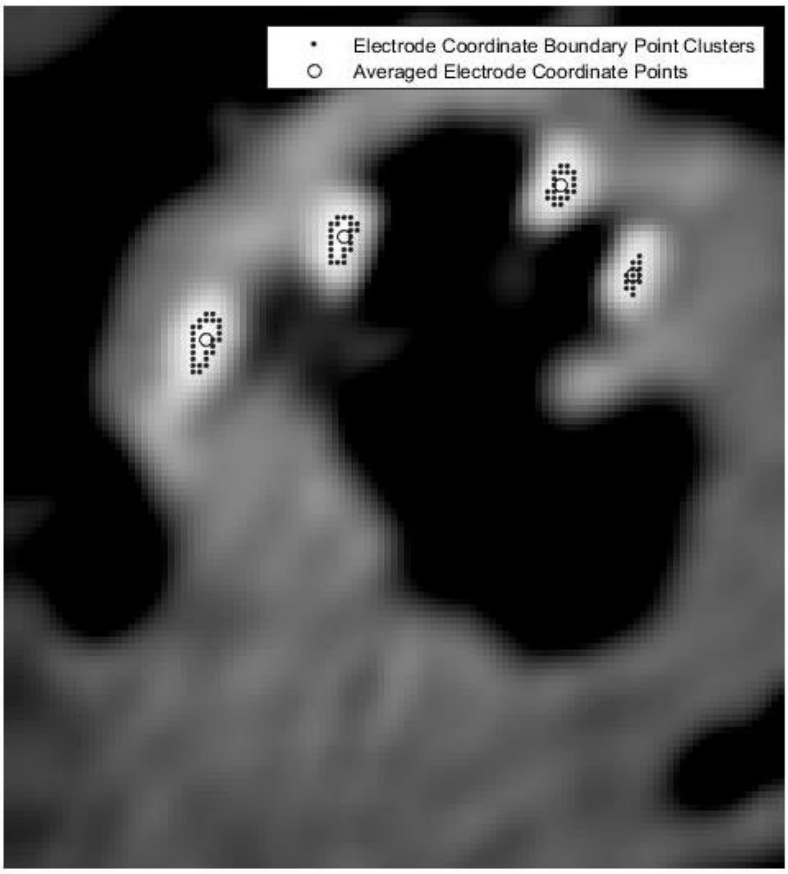

Figure 3.11 – Example of electrode contacts detected on a CT image through intensity thresholding and which are used to construct the spiral coordinates that describe the intra-cochlear trajectory of the electrode array. This electrode was inserted to an angle greater than 541˚.

3.3.1.2 Detection and application of the electrode superior view scaling factor

The electrode superior view scaling is an additional step to verify that the electrode array trajectory coincides from both a radial and superior view. Once the largest range of valid points in the electrode array is extracted, smoothed and interpolated, the superior view scaling factor is determined and applied to the electrode spiral if superior view CT images of the user are available. To determine the superior view scaling factor, the function `electrode_top_scale_pre_rotation` was developed. The researcher is required to ensure that the estimated centre of the cochlea, the modiolus, is as close as possible to the centre of the image by manually cropping the CT image. **Figure 3.12** presents the processing steps to extract data from the superior view.

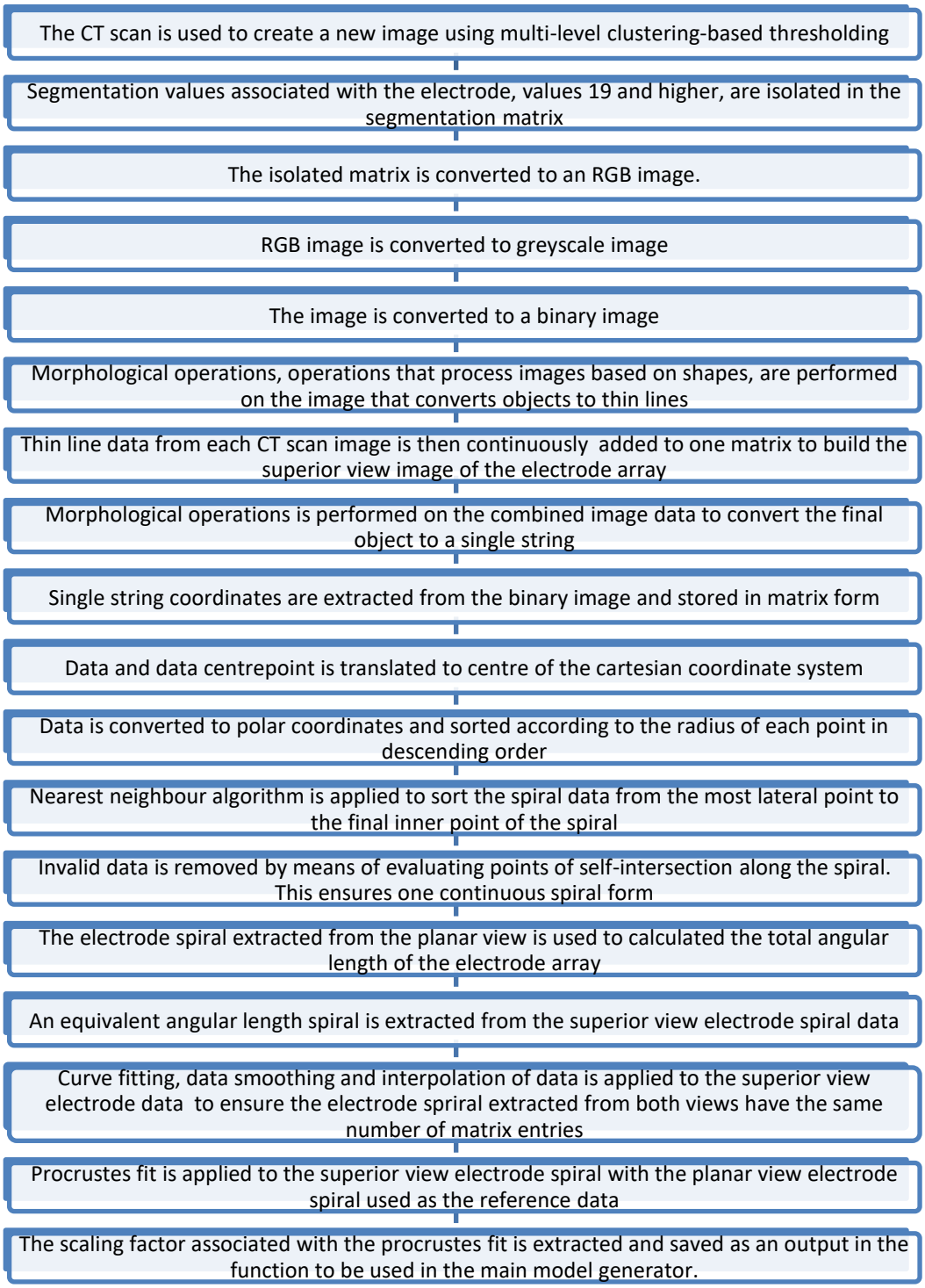

Figure 3.12 – Workflow diagram followed to detect and calculate the electrode spiral and the scaling factor of the electrode, respectively.

A similar approach is followed to extract the electrode coordinates from the superior view CT scan as in the radial view of the CT scans. The description of the processing steps is repeated here for reference.

- A built-in MATLAB function, *multithresh* is used, which makes use of multi-level clustering-based thresholding to segment an image.
- The various levels of the built-in function have a range of 2 to 21, where each level has a specific number and colour associated with it.
- The CT scan images that provide a superior view of the cochlea under evaluation are each converted to a multi-level threshold image.
- The colours of the multi threshold levels associated with the electrode are levels 19 to 21.
- These levels for each image are isolated and extracted and used to create a binary image.
- Built in morphological operations in MATLAB, such as *bwmorph*, are applied to each image to convert the objects, representing the electrode, to lines.
- As each image is evaluated, the single pixel width line data from each image is continuously added to each other.
- At the end of each image evaluation, the morphological operation is applied again to the combined image to create an image with a single line that represents the superior view of the electrode pathway.
- The x and y coordinates of the thin line data are extracted from the image and placed in a matrix.
- The extracted coordinates are translated in such a way that the centre of the image is translated to the 2D Cartesian centrepoint in the xy plane.
- The data points are then rearranged from the largest most lateral spiral point to the most central point, through the use of the Nearest Neighbour algorithm.
- The angular position of each of the superior view electrode spiral points is calculated.
- After the superior view electrode pathway extraction, the superior view data must be compared with the radial view electrode spiral data.

- The angular length of the radial view electrode spiral data is calculated.
- Data from the superior view electrode spiral is extracted from the inner most electrode point to the most outer electrode spiral point, which gives an equivalent angular length to the angular length of the radial view spiral point.
- A curve fit is applied to the superior view electrode spiral points in addition to interpolation. This is done to ensure smoothed data and that the number of data points in the superior view electrode spiral and the radial view electrode spiral are equal.
- A Procrustes data fit is applied to the radial view electrode spiral, with the superior view electrode spiral used as reference data. **Figure 3.13** depicts an example of an extracted electrode from both the superior view and the scaled radial view electrode.
- The scaling factor is extracted from the Procrustes fit and is applied to the electrode spiral coordinates to yield the final computational description of the electrode array's trajectory.

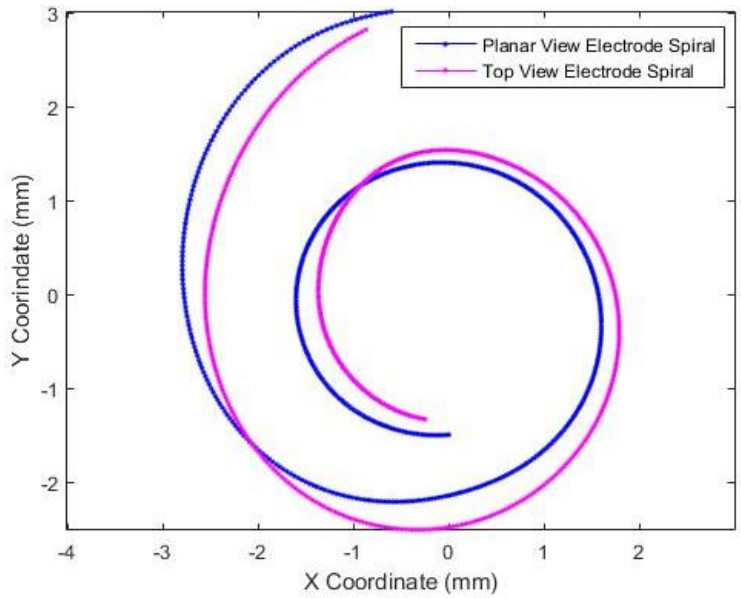

Figure 3.13 – Example of an electrode spiral as measured from the superior view CT scans and the planar view CT scans.

3.3.2 Spiral rotation adjustment

To take into account the orientation of the cochlea, the spiral z values must be evaluated to determine if the measured cochlea was orientated at an angle different than an upright and vertical orientation. In an ideal scenario, the z values of the spirals should mostly increase in a monotonous fashion for a correct estimation of the modiolus.

To counter such errors, the functions `best_fit_rotation` and `best_fit_indicator` were developed. The logical workflows of these functions are given in **Figure 3.14**. The rotation of the measured spirals is treated as an unconstrained optimisation problem with the aim to minimise the cost function. The cost function calculates the combined goodness of fit values of lateral, upper and lower spirals to their respective straight line curves through iteratively rotating all three spirals around the x and y axis with the use of a built-in optimisation function of MATLAB. The angle of rotation which provides the best combined goodness of fit value, associated with the lowest value, is selected as the preferred angle of rotation about the x and y axis. The rotation is then applied to all three cochlear spirals as well as the electrode spiral. All the rotated spirals are then translated to the initial position of the most superior point of the upper spiral.

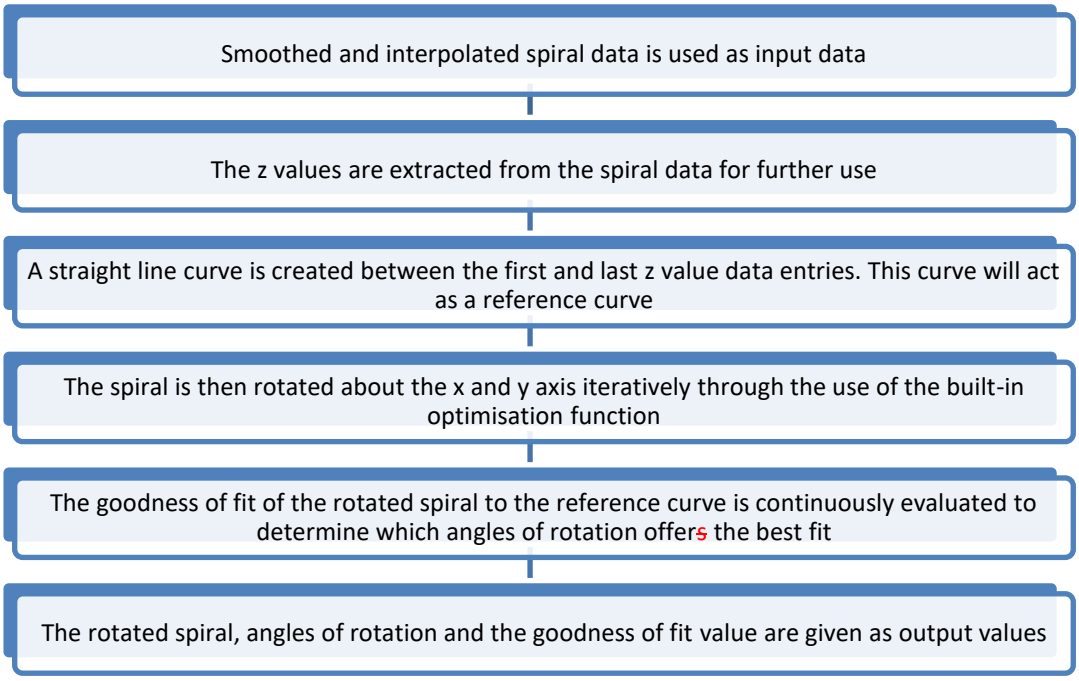

Figure 3.14 – Workflow diagram of the method in which the spiral data is rotated in the developed function.

After all spiral landmark data are extracted, smoothed and rotated, the data can be used to construct the 3D model framework. This process is discussed in the following sections.

3.3.3 Cochlea internal structure template

To create the framework of the 3D cochlea model, a predefined cochlear template must be adjusted according to the three cochlea spirals extracted from the CT scans. The template not only contains points defining the outer boundaries of the cochlea, but also additional points that define further internal structures. The template consists of the following internal structures.

- Vestibular Membrane
- Basilar Membrane
- Auditory Nerve fibres
- Scala Media
- Organ of Corti
- Scala Tympani
- Reissner's Membrane
- Spiral Ligament
- Scala Vestibuli
- Stria Vascularis
- Auditory Nerve

The three extracted spirals are used as reference spirals to which the template data must be rotated, scaled and translated. To perform the scaling of the structures, the function `Internal_Structure_Scalingf` was developed. **Figure 3.15** depicts the logical workflow of how data processing is performed within the function in order to achieve this template scaling and adjustment.

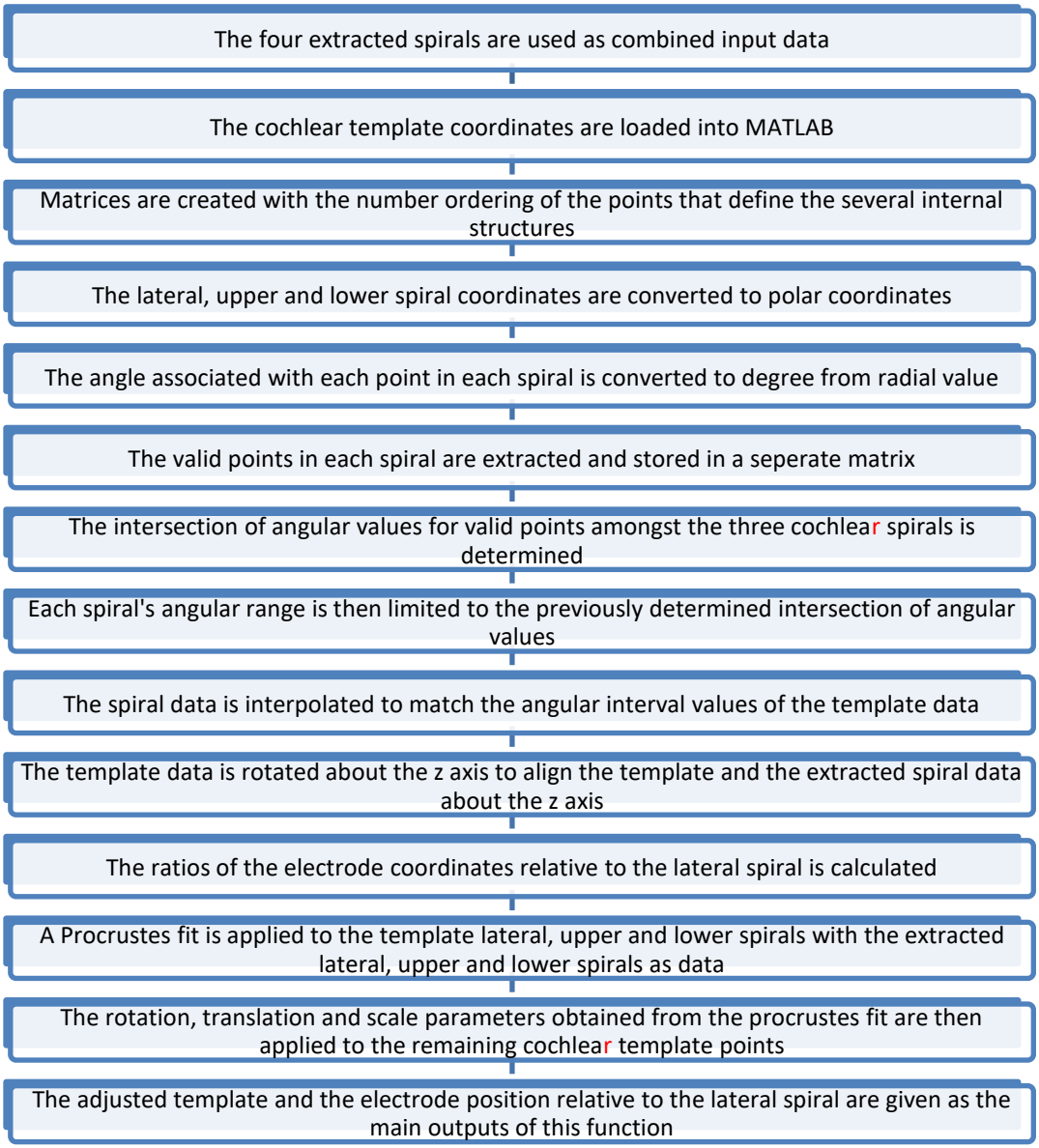

Figure 3.15 – Workflow diagram used to perform the Procrustes fit of the cochlea template to the measured landmark spiral data.

Three specific data points from the template data are used to compare and scale according to the extracted spirals. These data points are numbered points 1, 5 and 7, which represent the lower, lateral and upper spirals of the template data, respectively. These points are indicated in **Figure 3.16**.

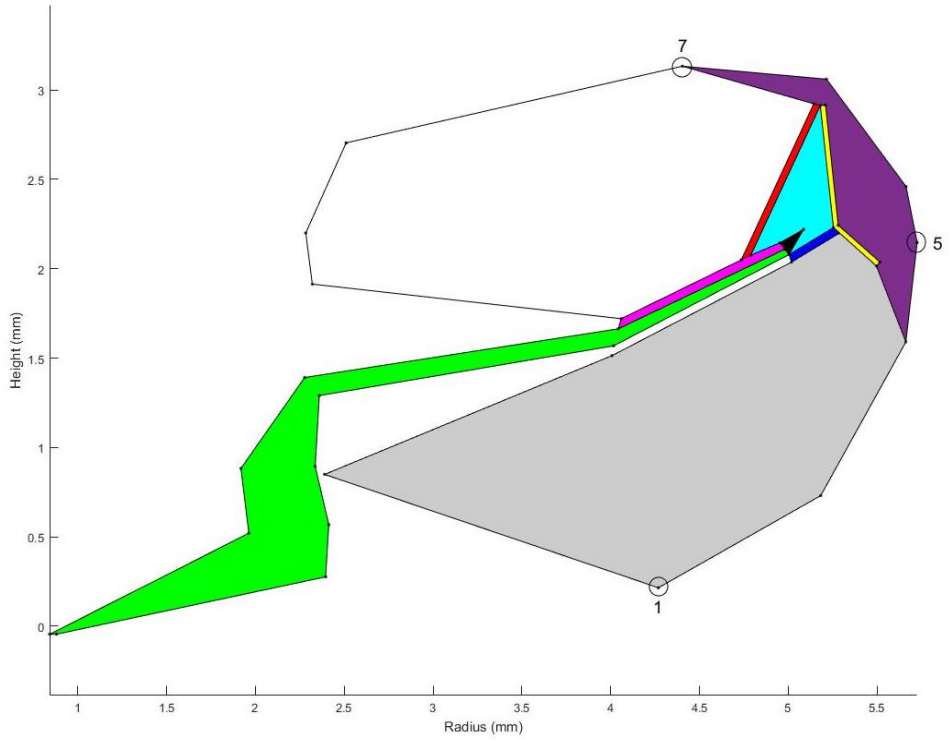

Figure 3.16 – Cross-sectional view of template data fitted to the measured lower (1), lateral (5) and upper (7) landmark spiral points.

A Procrustes fit is performed on the template spirals for each angular interval face of the cochlea. The Procrustes fit makes use of scaling, rotation and translation, calculated with the built-in MATLAB `Procrustes` function, and applied to each angular interval face of the cochlea template. Equation (3.1) is used to perform the Procrustes fit to the template data points. The template data points are seen as the matrix variable($\mathrm{Temp}_{\mathrm{Data}}$), the scale factor is SF, the orthogonal rotation matrix Rot and the translation matrix (Trans).

$$\mathrm{Transformed} = \mathrm{SF} * \mathrm{Temp\_Data} * \mathrm{Rot} + \mathrm{Trans} \tag{3.1}$$

The Transformed matrix is then further used as the framework data points from which the model of the cochlea is constructed.

3.3.4 Reconstruction of electrode array in adjusted template

When fitting the template data to the measured spiral points, the adjusted template data is used as the framework for the cochlear model from this point forward. To ensure the user-specific electrode array trajectory is maintained in the adjusted template, it is necessary to include a processing step to reconstruct the electrode array trajectory within the adjusted template or **Transformed** data. To maintain the relationship of the electrode spiral relative to the measured landmark spirals, the polar coordinate ratios of the electrode spiral relative to the landmark spirals are created.

3.3.4.1 The electrode array trajectory ratio calculation

To reconstruct the electrode array trajectory by taking into account all three spirals the following method was used.

- As the upper and lower spiral radii are very similar, an average radius profile for the upper and lower radius profiles is first calculated, $\bar{\rho}_{LU}$.
- The difference between the measured electrode array radius $\bar{\rho}_{e}$ and the averaged radius, $\bar{\rho}_{LU}$ is then calculated.
- The difference between the measured lateral spiral radius and the average radius is calculated, $\bar{\rho}_{LL}$, after which the ratio between these two distances are calculated and stored in the data array $\overline{\text{Radius\_ratio}}$. This calculation is also given in equation **(3.2)** below.

$$\overline{\text{Radius\_ratio}} = \frac{\bar{\rho}_{e} - \bar{\rho}_{LU}}{\bar{\rho}_{LL}} \tag{3.2}$$

The z value ratio for the electrode array comprises of a similar calculation procedure as indicated above.

- The distance between the electrode z value and the lower z value is calculated, $\bar{z}_{eL}$, and divided by the difference between the upper and lower spiral z values, $\bar{z}_{UL}$,. This calculation is given in equation **(3.3)**.

$$\overline{\text{Height\_ratio}} = \frac{\bar{z}_{eL}}{\bar{z}_{UL}} \tag{3.3}$$

The ratios can now be used to reconstruct the electrode array trajectory within the adjusted template. This reconstructed electrode trajectory is given the variable name Electrode_Final and is used as the final electrode array trajectory from this point forward.

3.3.5 Defining the electrode geometry

Once the electrode array is reconstructed according to the lateral spiral of the transformed template, the user is asked to enter the cochlear implant make and model through the use of the `electrode_geometryf` function. This function was created to define the geometrical characteristics of each of the electrode arrays, based on the type of cochlear implant derived from a reference guide from Cochlear (Cochlear.com, 2016). The reference guide compares the various electrode array models from the Cochlear, Med-El and Advanced Bionics.

The researcher is asked to indicate the make and model of the electrode array from a given list. Each make and model has a specific identity number or value, identity, which is used further in the function as well as additional functions that follow. Based on the researcher's choice of the type of electrode array, the geometrical properties of the electrode array carrier and contact points are used from this point onward. **Figure 3.17** depicts the data handling and processing involved in the function `electrode_geometryf`.

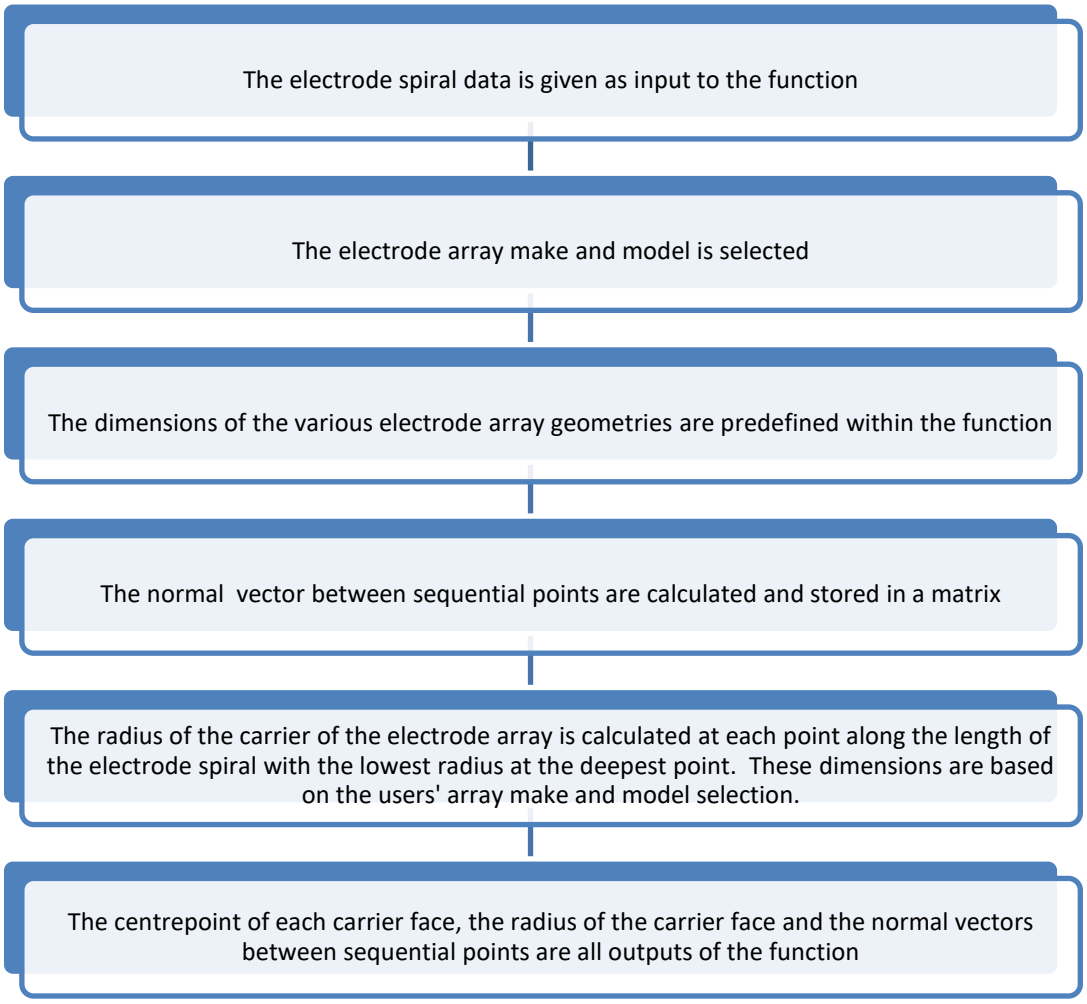

Figure 3.17 – Workflow diagram of the procedure followed in order to calculate the electrode array carrier dimensions, based on the user's input of the make and model of the cochlea.

3.3.6 Electrode array interference with cochlear walls: detection and correction

Once the electrode geometric details have been selected and further calculated, the adjusted template and the electrode array must be inspected for interference. In some instances, the electrode array could protrude the cochlea's outer wall. Such cases must be detected and taken into account as the electrode array cannot lie outside the outer boundary walls of the cochlea due to the human cochlea being enclosed by bone. The cochlea boundary points must therefore be adjusted in such a way that the entire electrode is inside the outer wall of the cochlea or the cochlea boundary. In order to achieve this in an

automated fashion, the function `interference_check_adjustment_electrode_cochlea_opt` was developed, with the logical workflow of the function depicted in **Figure 3.18**.

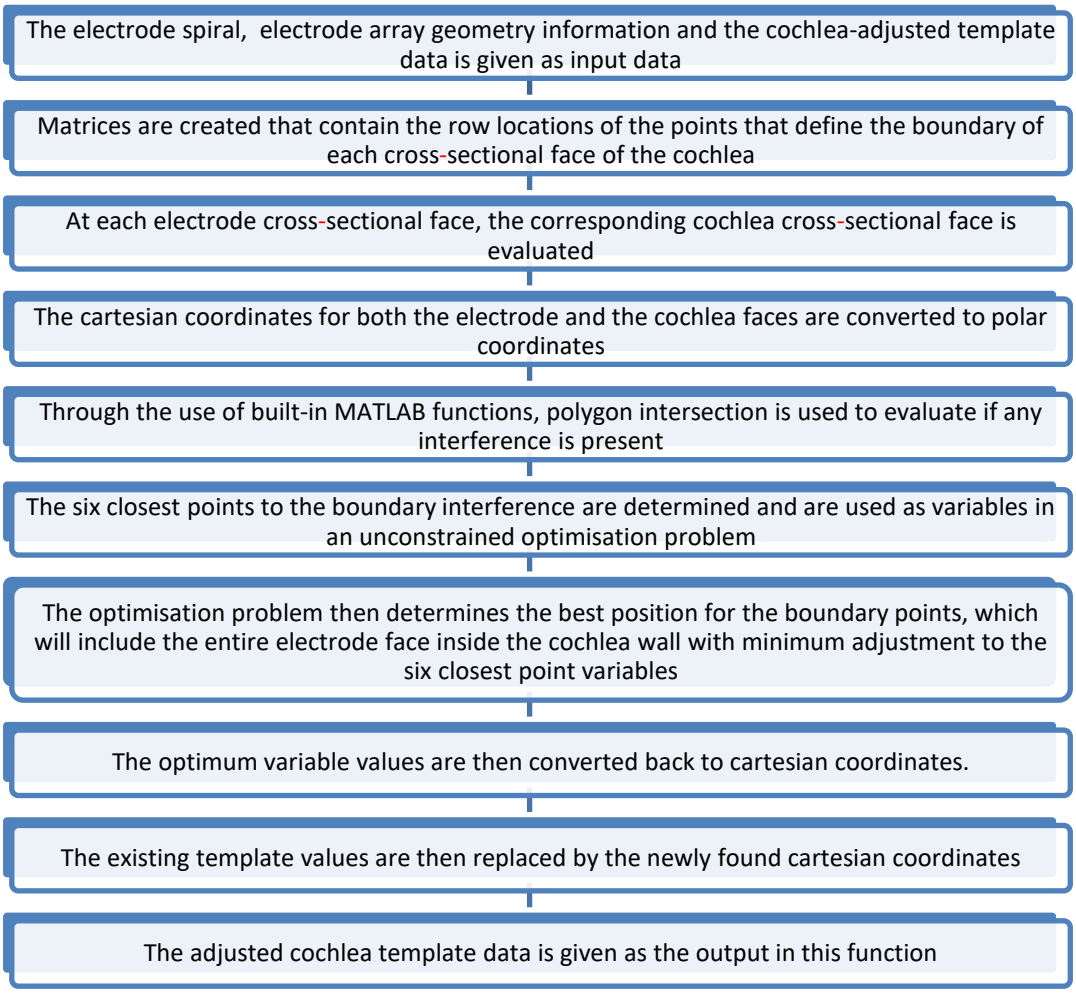

Figure 3.18 – Workflow diagram of the function developed to detect and remove any interference between the electrode and outer wall of the cochlea.

The entire interference check is seen as an unconstrained optimisation problem. This requires a cost function, which the built-in optimisation functions of MATLAB aim to minimise. To change the boundary values in such a way that the entire electrode is included in the cochlea, the cross-sectional view of the cochlea and the electrodes at the same angular positions are evaluated.

- Built-in MATLAB functions, such as “inpolygon”, are used to determine if the polygon created by the electrode cross-sectional face, is situated inside the polygon created by the cochlea cross-sectional boundary points.
- The total number of points that define each electrode cross-sectional face are equal to 629; thus, if the number of points inside the cochlea cross-sectional boundary polygon are less than 629, protrusion of the outer wall is present.
- Once protrusion of the outer wall is detected, the 6 cochlear boundary points closest to the centrepoint of the electrode face are calculated. The x and y coordinates of these six points are seen as the independent variables in the optimisation problem, which are to be adjusted.
- The cost function used in the optimisation problem consists of two parts. The first part consists of maximising the number of cross-sectional points inside the cochlea. The second part is to minimise the goodness of fit value of the adjusted boundary points to the initial position of the cochlear boundary points. The second part of the cost function ensures that the changes made to the cochlea boundary points are made in such a way that the shape of the cross-sectional face is preserved as far as possible.

  The number of points that define the cross-sectional face of the electrode array inside the cochlea at a specific angle, are equal to **in_11** and the goodness of fit value is represented by **GOF**. The cost function is given in equation **(3.4)**.

$$F = -\frac{in\_11}{629} + GOF \tag{3.4}$$

  The cost function aims to minimise the goodness of fit value (the lower the value the better the data fit) whilst maximising electrode cross-sectional points inside the cochlea **in_11**.

  Figure 3.19 shows an example of the possible interference that could occur between the cochlea face and electrode array from a cross-sectional point of view.

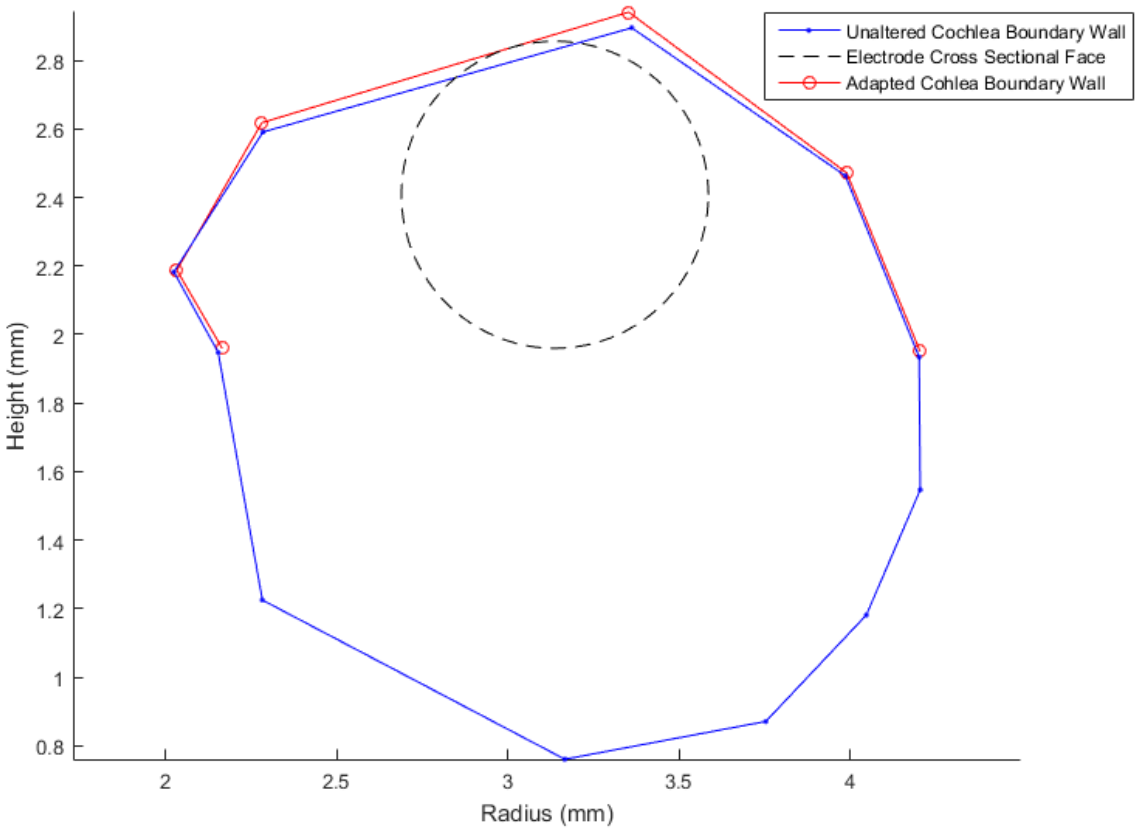

Figure 3.19 – Example of interference that could occur between the electrode and the cochlear boundary wall. For the case at hand, the interference is present at the superior boundary wall of the cochlea. The image shows the adjusted (red) and unaltered (blue) cochlear walls.

3.3.7 Cochlea self-interference detection and adjustment

Additional interference that could occur in the model itself, is the interference of the basal turn with the upper middle turn due to overlapping angular positions. These interferences must be identified and accounted for through the adjustment of the cochlear outer wall points.

To achieve this, the function `Interference_check_adjustment_cochlea` was developed. This function works in a similar fashion as the electrode array interference

function but only evaluates the cochlear structure. **Figure 3.20** describes the data handling process involved in the `Interference_check_adjustment_cochlea` function.

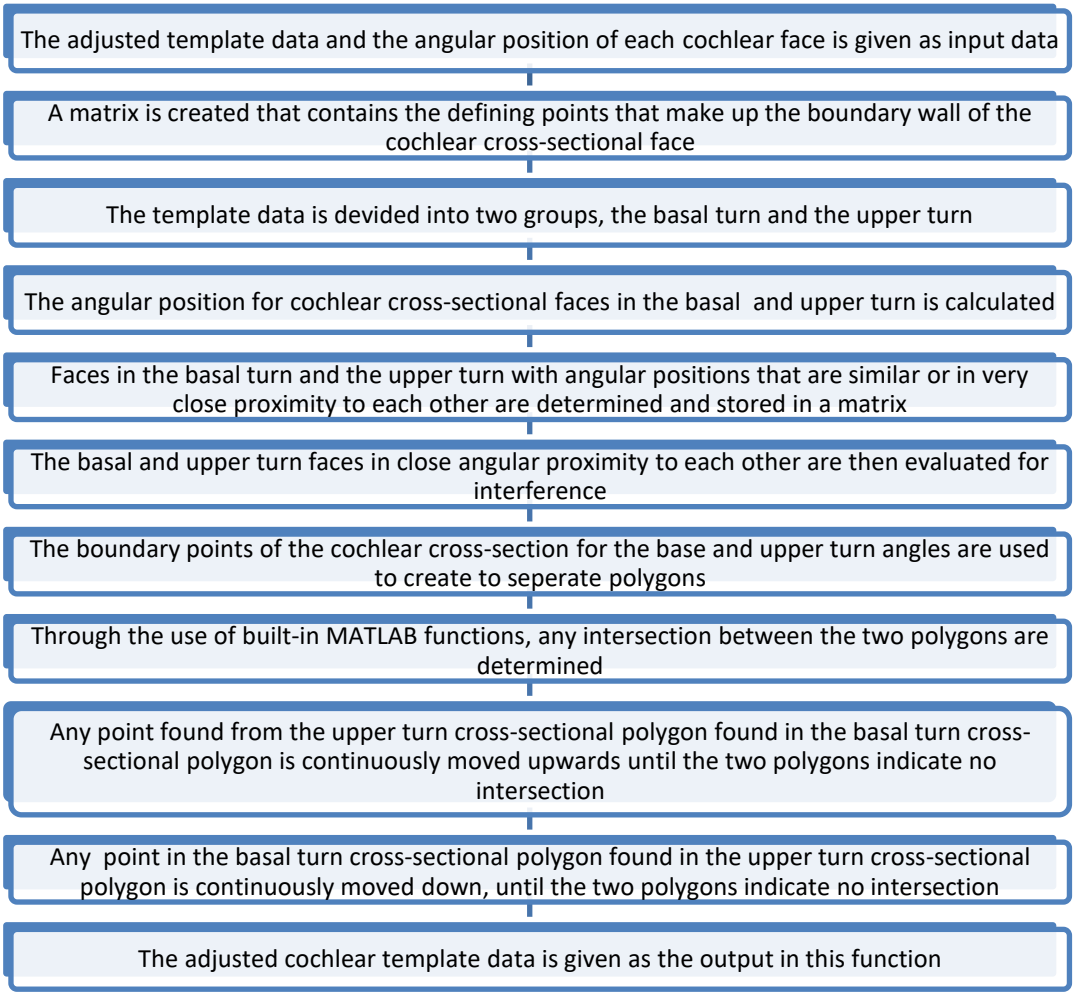

Figure 3.20 – Workflow diagram of the method followed to detect and resolve any interference present between the basal and more apical cochlear turns. If these cochlear turn cross-sectional faces have similar angular positions, interference could exist between such two faces and must be corrected.

The function determines the angular position of each of the several cross-sectional faces of the cochlea. It is then determined which cross-sectional faces in the basal turn have a close proximity to the cross-sectional faces of the upper turn by evaluating angular positions that are very similar.

At each of these angular faces, the cross-sectional faces are evaluated. The outer wall of each cross-sectional face is seen as a closed polynomial curve. Through the use of built-in MATLAB functions, the function evaluates whether any of the two polynomial curves protrude into each other. If such points are found, the points are moved systemically whilst continuously testing if the two polynomials intersect each other. This process is repeated until no intersections are present. **Figure 3.21** shows an example of detected interference between the outer boundaries of the basal and upper turn of the cochlea at a specific angular position as well as the corrected boundary walls.

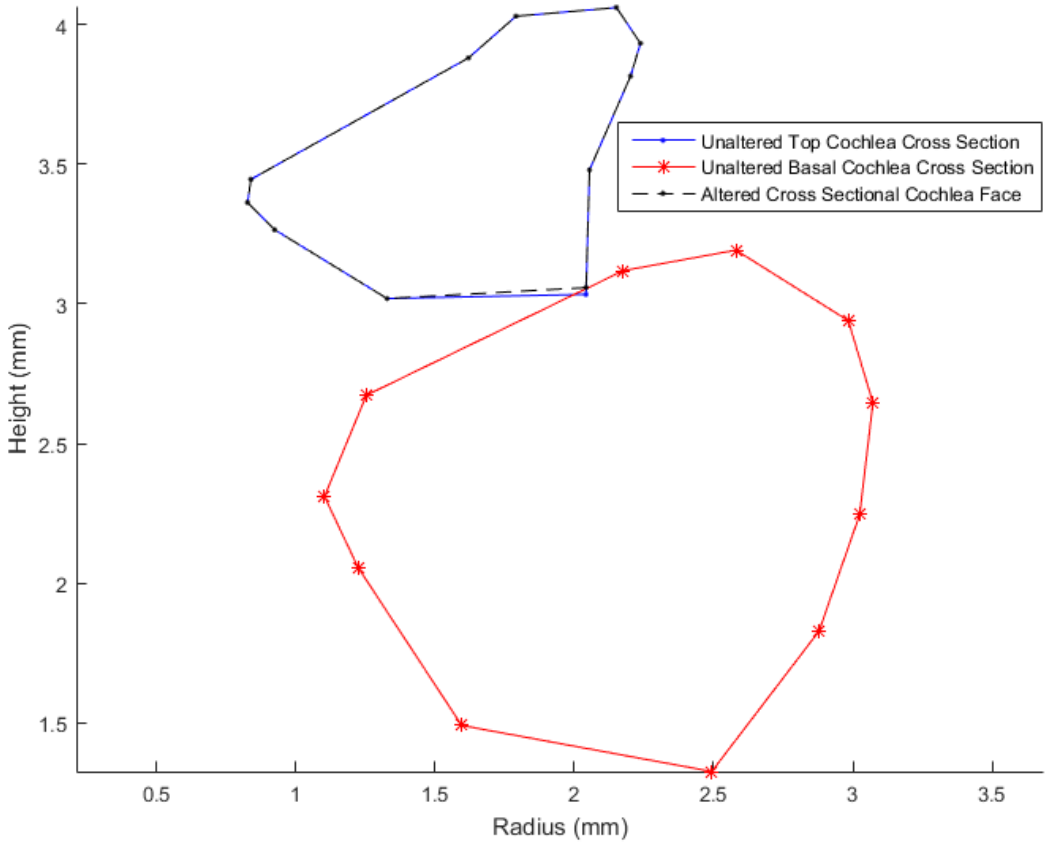

Figure 3.21 – Cross sectional view of an example of cochlear interference that could occur between the basal and apical turns of the cochlea after template adjustment. In the example, the upper turn cross-sectional face protrudes into the basal cochlear face. The apical boundary point inside the basal point is moved to a position outside the basal turn cross-sectional face.

3.3.8 Creation of the 3D volumes of the individual cochlea internal structures

At the stage where all data processing is completed, the model development algorithm enters the generation of the 3D geometric volumes. This is achieved through the integration of MATLAB and COMSOL.

The first objects that are created, are the internal structures of the cochlea itself for which the function *COMSOL_geom_plot_internal_structures* was developed. The logical data handling process for this function is given in **Figure 3.22**.

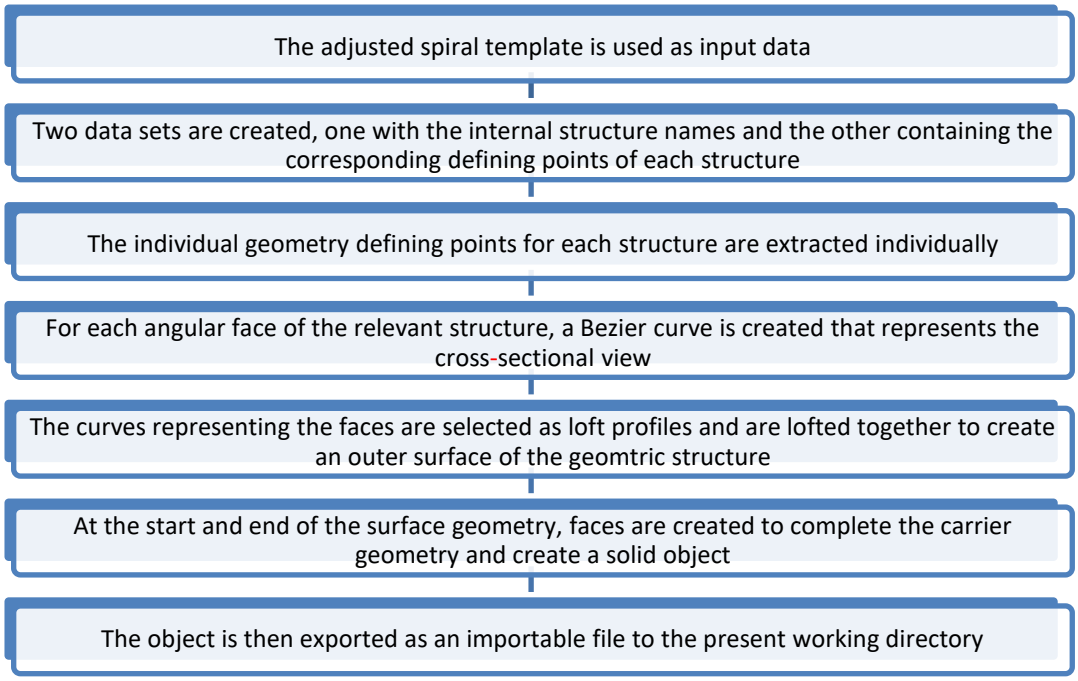

Figure 3.22 - Workflow diagram indicating how the 3D cochlear volumes are created with the developed MATLAB function.

The function uses a specific combination and order of points from the adjusted template to create each internal structure.

- The points for each structure are extracted at each interval angular position.
- From these points a polygon is created that defines the cross-sectional face for the relevant structure at hand, at each interval angular position.

- These faces are then used as template faces in COMSOL's loft function through which a surface structure is created. **Figure 3.23** depicts an example of the creation of the 3D volume of the Spiral Ligament of the cochlea.
- The surface structure is still open at the basal and apical end for which capped faces are created in COMSOL.
- The two cap faces and the surface structure are combined to create a 3D volume
- The volume is then exported as a .mphbin file (COMSOL importable file) with the name of the file the same as the relevant structure.
- This process is repeated until all the internal structures are combined.

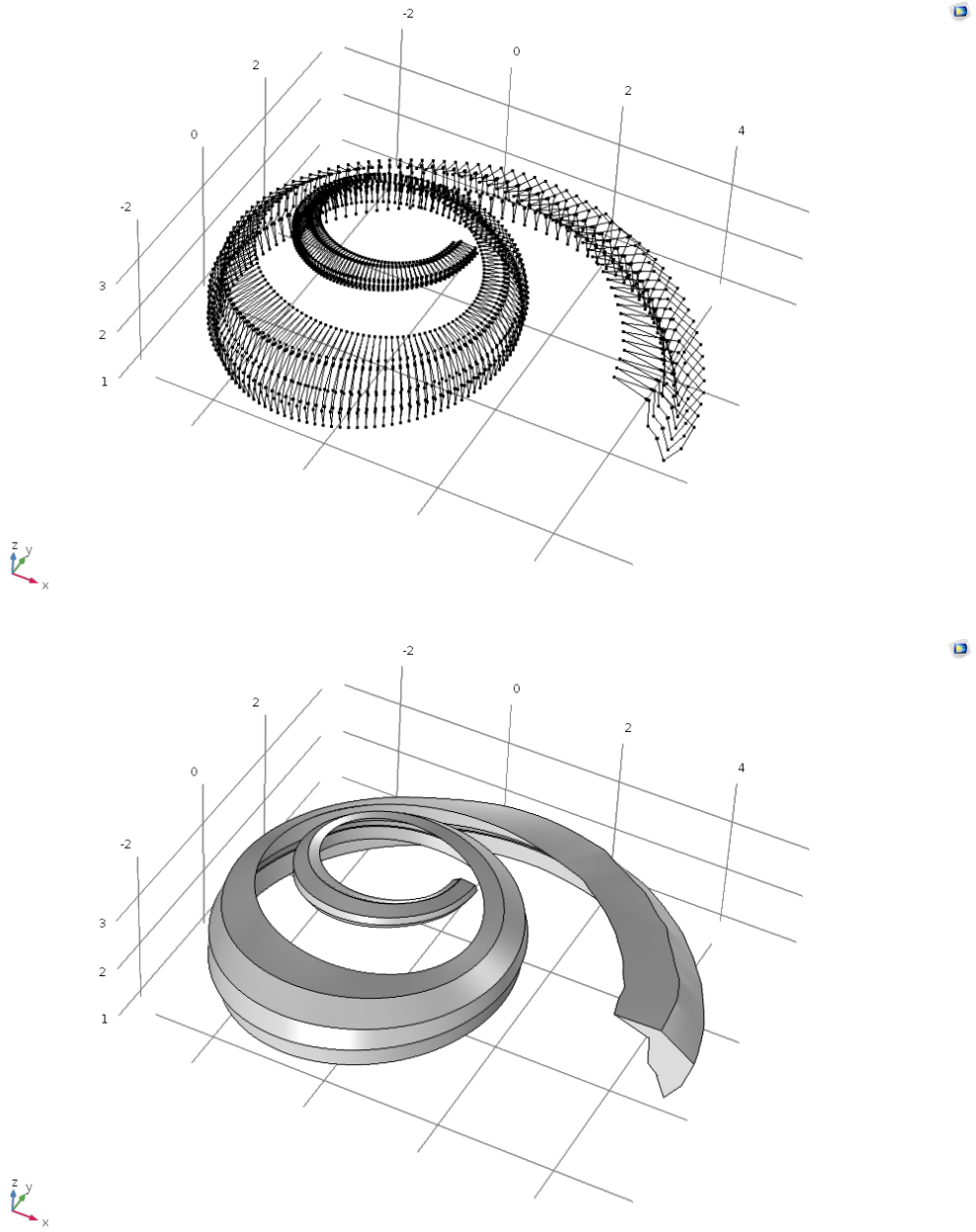

Figure 3.23 – Example of the generation of the 3D volume in COMSOL by first creating a framework of polygon cross-sectional faces (top) and resultant lofted solid volume (bottom).

3.3.9 Creation of the electrode array 3D volume structure

The penultimate stage of the model development workflow is the creation of the electrode array 3D volume file. To create this structure, the function

COMSOL_geom_plot_electrode was developed. The workflow of data handling and volume creation in the function is given in **Figure 3.24** below.

Figure 3.24 – Workflow diagram indicating the method involved in the creation of the 3D electrode array volume.

Based on the identity value of the electrode array, the type of electrode contact is determined, which is either a half band or a full band contact.

- The initial step creates 629 points, which define the cross-sectional carrier face of the electrode at each angular interval point along the electrode spiral.

- Each of these cross-sectional sets of coordinates are rotated in such a way that the normal vector of the cross-sectional face coincides with that of the normal vectors at each interval point along the length of the electrode spiral.
- From these points, a polygon is created that defines the cross-sectional face for the electrode array at each interval angular position along the length of the electrode spiral.
- These faces are then used as template faces in COMSOL's loft function through which a surface structure is created.
- The surface structure is open at the basal and apical end for which capped faces are created in COMSOL.
- The two cap faces and the surface structure are combined to create a 3D volume
- At this stage, the carrier 3D volume is created to which the electrode contacts must be added.
- From the most apical point of the electrode array, the contact plates are added at the specific locations based on the comparison sheet of Cochlear (Cochlear.com, 2016), with the specified electrode contact plate lengths and characteristics.
- The contact points and the carrier volumes are combined through the use of the partition function in COMSOL.
- The electrode volume is now complete and is exported as a .mphbin file (COMSOL importable file) with the name of the file the same as the relevant structure.

The final stage of the model generation algorithm creates a COMSOL .mph file in which all the 3D cochlea internal structures and the electrode volumes are imported and assembled. This file can then be further used by the user to perform the required simulations within COMSOL. **Figure 3.25** depicts an example of an electrode array generated as a 3D volume in COMSOL, using the method at hand.

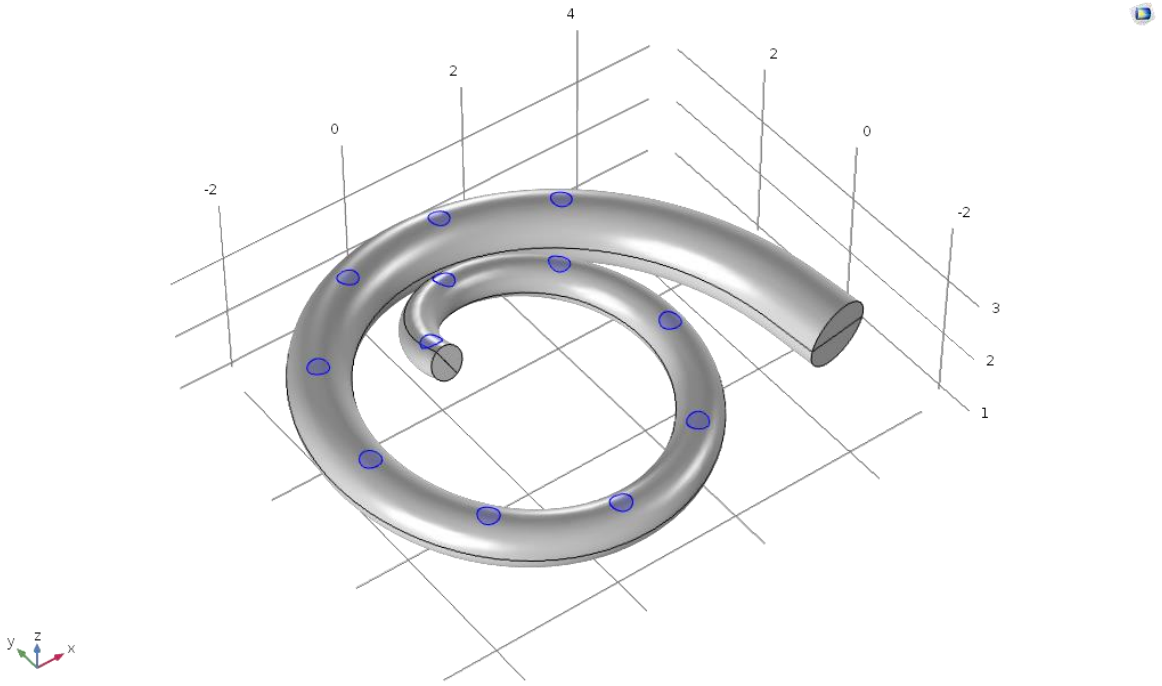

Figure 3.25 – 3D volume of a cochlear implant electrode array created in COMSOL. The electrode array is a Med-El Combi 40 Medium electrode array. The circular structures highlighted in blue are the electrode contact points.

3.3.10 Final COMSOL simulation file creation of combined model

Once the internal cochlear structures and the electrode array are successfully created, the structures are automatically imported and combined to form a single model. A 15mm diameter sphere is created, which acts as the surrounding bone structure as well as the electrical ground source. **Figure 3.26** depicts an example of a combined cochlear model created with the automated method. The surrounding sphere, representing the surrounding bone, is disabled in this view to make the modelled cochlea and electrode array visible.

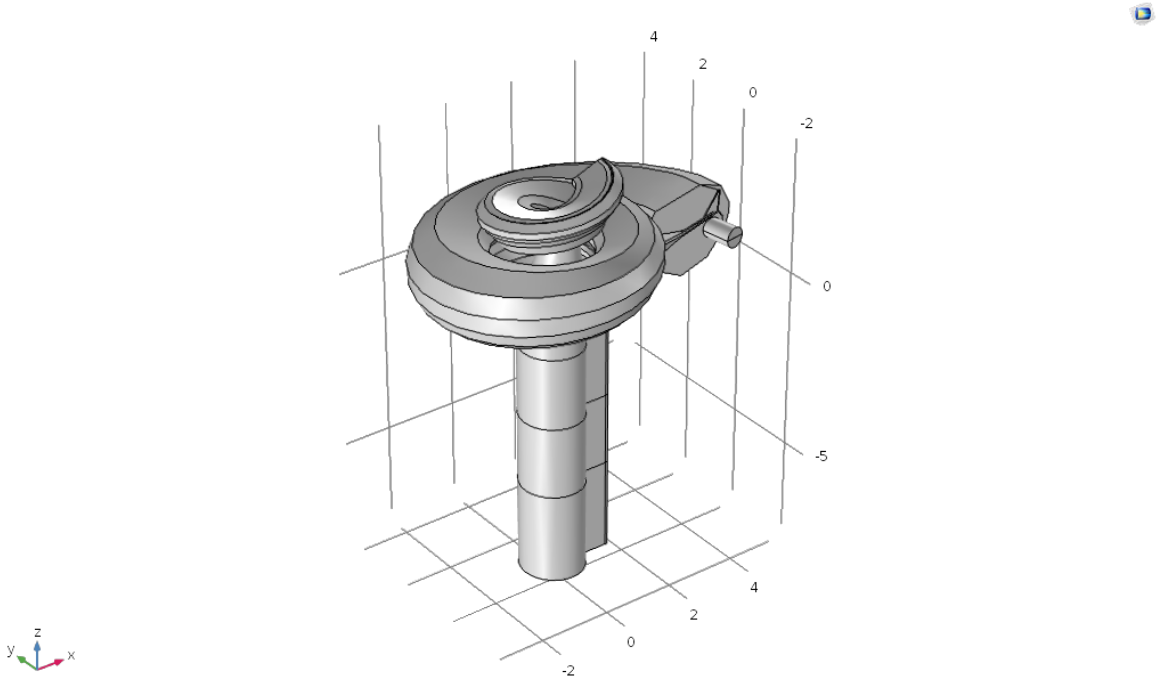

Figure 3.26 – Combined cochlea model with the electrode array in COMSOL, all of which were developed with the automated method developed in this study.

3.4 SIMULATION CONDITIONS

A total of 6 cochlea models were created based on anatomical data obtained from three patients, all of whom were implanted with bilateral cochlear implants. **Table 3.2** provides further information regarding the cochlea models.

Table 3.2 – User model number and electrode information

User cochlea number allocation	Left or Right Ear Cochlea	User Number	Electrode Array Type
S13 L	Left ear	S13	Cochlear™ Contour Advance
S13 R	Right ear	S13	Cochlear™ Contour Advance
S3 L	Left ear	S3	Cochlear™ Contour Advance
S3 R	Right ear	S3	Cochlear™ Contour Advance
S30 L	Left ear	S30	Med-EL Combi Compressed
S30 R	Right ear	S30	Med-EL Combi 40 Medium

Each of the generated models contains a cochlear structure and an electrode array, all of which are surrounded by a sphere of equal diameter for all the models. Each of the models are exposed to the same simulation conditions and are indicated below.

3.4.1 Material Properties

For each simulation, the "Electric Current" Multiphysics equations and conditions are applied. By using these equations, the electric conductivity of each anatomical structure is required and are given below in **Table 3.3**. The same material properties used in the study of Malherbe et al. (2016), are applied to cochlear structures of both the manual and automated models. Due to the material properties of the model assumed to be purely resistive (i.e., no capacitive effects), Ohm's law dictates the voltage at any point in the model to be linearly related to the stimulating current because of the geometry and material properties between the stimulating electrode and the point (Malherbe et al., 2016).

Table 3.3 - Cochlear structure conductivities used in the models.

Cochlear Structure	Conductivity [S/m]
Scala Tympani	1.43
Scala Vestibuli	1.43
Scala Media	1.67
Bone Surrounding the Cochlea	0.01553
Auditory Nerve	0.3333
Stria Vascularis	0.0053
Spiral Ligament	1.67
Reissner's Membrane	0.000098
Organ of Corti	0.012
Silicone Rubber	1
Metal Electrodes	1000
Basilar Membrane	0.0125

3.4.2 Stimulation Conditions

In this study, only a constant current monopolar stimulation protocol was included in the investigation, as this was sufficient to compare model predictions made with automated and manual model development strategies. Monopolar stimulation involves applying a current source to a single electrode contact while connecting the ground to a structure outside the cochlea. For this study, the outer boundaries of the spherical bone volume surrounding the cochlea were used as the ground. This allowed the current to flow from the stimulating electrode through the relevant structures of the cochlea to the outer boundaries of the surrounding sphere under steady state conditions. The use of steady state conditions, such as a constant current source, reduces the computational time when compared to time-varying simulation (Gross, 2017). Electric potential distributions across the nerve fibres were then predicted by COMSOL under steady state model conditions.

CHAPTER 4 RESULTS

4.1 CHAPTER OBJECTIVES

This chapter first assesses the accuracy with which cochleae are initially detected through the automated method, after which the landmark similarities with manual methods are evaluated. The geometrical differences between the manual and automated models are shown and the predicted electric potential distributions are compared between the two modelling approaches.

4.2 APICAL POINT DETECTION AND FINDING THE COCHLEA

The initial detection of the cochlea is a crucial step in the automated model development strategy, and it is therefore imperative that the automated method is able to successfully detect the cochlea on a CT scan image. For each user, each CT image was evaluated to find the apical point of the cochlea on the slide, after which a mean apical point was calculated for each user. **Figure 4.1** and **Figure 4.2** show the mean apical points found for the cochleae as listed in **Table 3.2**.

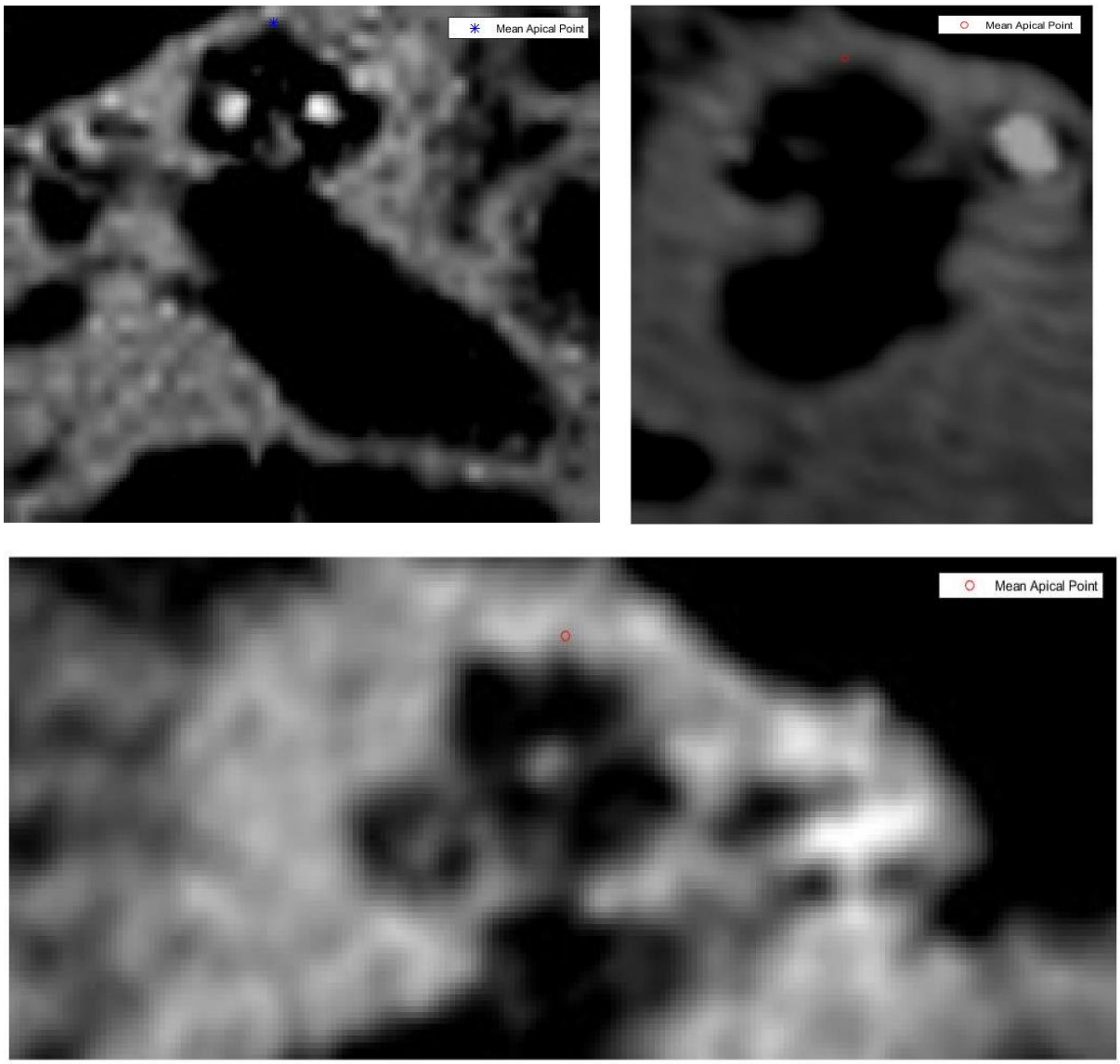

Figure 4.1 – Position of the mean apical point detected with the automated method for S13 L (top left), S3 L (bottom) and S30 L (top right).

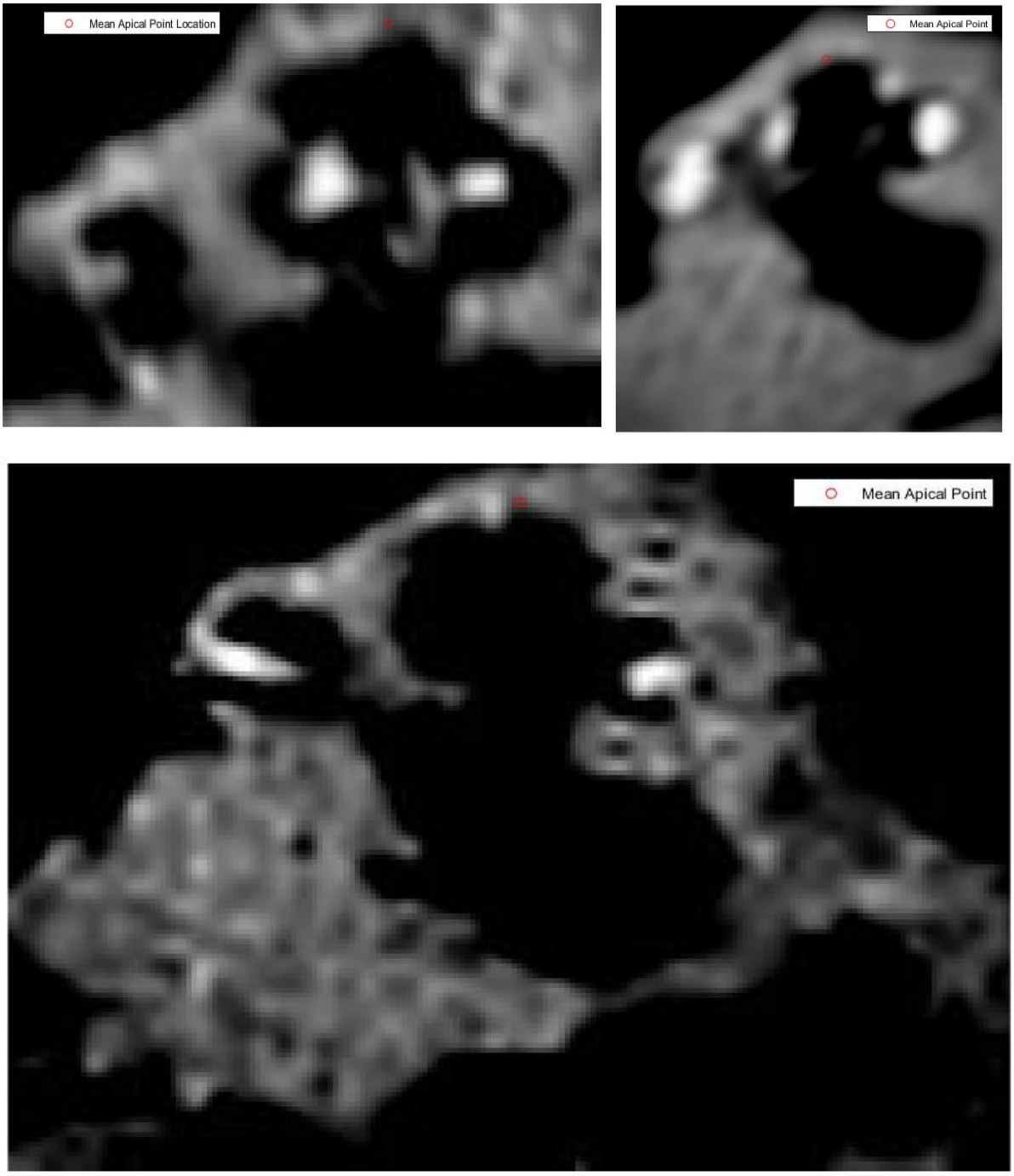

Figure 4.2 - Position of the mean apical point detected with the automated method for S13 R (bottom), user S3 R (top left) and user S30 R (top right).

In order to maintain a constant reference point on all CT images of each user, a mean apical point was used for each cochlea evaluated. This mean apical point position was

used in subsequent steps of the model development workflow as the vertical centreline, i.e. modiolus, around which the cochlea is rotated.

Table 4.1 is a summary of the standard deviation (STD) of the x and y coordinates of the apical point as detected on each of the radial CT images, as well as the percentage of CT images on which the automated method was able to identify the cochlea. Model S30 R showed the highest percentage of CT scan images on which the cochlea was found, whilst S3 L showed the lowest number of CT scans on which the cochlea was detected, as seen in **Table 4.1**. The cochlea was detected on a mean value of 95.87% of all CT images that were processed.

The larger variation seen in the x coordinates can be attributed to the position of the apical point as one rotates around the modiolus of the cochlea. The apical point remains at a constant superior position on the y axis, but moves with the rotation of the cochlea on the x axis. This is due to the apical point x coordinate and the modiolus not always coinciding. The apical point therefore revolves around the modiolus and by calculating the mean apical point position, the position of the modiolus or axis of rotation can be found.

Table 4.1 - Cochlea Detection

	X – Coordinate STD (Pixels)	**Y – Coordinate STD (Pixels)**	**X – Coordinate STD (mm)**	**Y – Coordinate STD (mm)**	**% CT Scans on which Cochlea was found**
User S13 L	9.15	0.98	0.8791	0.0977	94.44
User S13R	19.05	1.1	1.689	0.098	92.22
User S3 L	26.7	2.39	2.377	0.213	91.66
User S3 R	5.81	1.42	0.516	0.126	98.89
User S30 L	3.72	0.27	0.27	0.055	99
User S30 R	5.216	0.689	0.498	0.066	99

4.3 COMPARISON BETWEEN MANUAL AND AUTOMATED MEASUREMENTS

The spiral landmark measurements made through the automated model development algorithm and the manual method are compared in **Table 4.2** to **Table 4.3** and **Figure 4.3** to **Figure 4.7**. The unaltered manual measurements made for user S13 R was not attainable and was therefore excluded in the comparisons made in section 4.3.1.

4.3.1 Similarity between the automated and manual methods

Table 4.2 and **Table 4.3** give the normalised root mean square error (NRMSE) and the correlation percentage, respectively, between the manually and automatically detected landmark points for the four primary spirals (lateral, upper, lower and electrode).

Table 4.2 - Calculated NRMSE between the automated and manual method landmark measurements.

			User				
			S13 L	**S3 L**	**S3 R**	**S30 L**	**S30 R**
NRMSE	**Radius**	Lateral Spiral	0.08	0.07	0.09	0.14	0.13
		Upper Spiral	0.18	0.24	0.14	0.19	0.09
		Lower Spiral	0.17	0.14	0.31	0.17	0.14
		Electrode Spiral	0.18	0.05	0.36	0.16	0.32
	Height	Lateral Spiral	0.08	0.22	0.17	0.12	0.09
		Upper Spiral	0.07	0.14	0.06	0.07	0.08
		Lower Spiral	0.18	0.44	0.11	0.24	0.23
		Electrode Spiral	0.06	0.19	0.12	0.13	0.13

The mean NRMSE for all spiral radii measurements presented in **Table 4.2** are 0.168 (similarity of 83.2% between manually and automatically detected landmarks), and 0.147 for all height measurements (similarity of 85.3% between manually and automatically

detected landmarks). When combined, the overall similarity between the automated and manual measurements equate to 84.3 %.

Table 4.3 - Calculated correlation percentage between the automated and manual method landmark measurements.

			User				
			S13 L	**S3 L**	**S3 R**	**S30 L**	**S30 R**
Correlation Percentage	**Radius**	Lateral Spiral	96.82	98.85	94.02	96.4	95.66
		Upper Spiral	94.10	93.57	95.6	94.39	98.31
		Lower Spiral	88.58	82.12	75.17	94.22	92.16
		Electrode Spiral	88.41	99.5	70.24	83.79	76.93
	Height	Lateral Spiral	89.07	84.24	90.38	96.6	97.51
		Upper Spiral	95.68	84.12	97.41	94.01	95.66
		Lower Spiral	91.94	61.27	99.09	94.64	94.57
		Electrode Spiral	99.49	96.34	92.38	21.14	98.68

Table 4.3 indicates an overall correlation percentage for manually and automatically detected radii of 90.44% and 88.71% for the cochlear height. The total correlation percentage between the two measurement methods is 89.58%, suggesting a high similarity between the manual and automated landmark detection data. The highest overall similarity of 87.5% was seen for the data of user S13 L. The comparison between the automated and manual measurement methods can be seen in **Figure 4.3**.

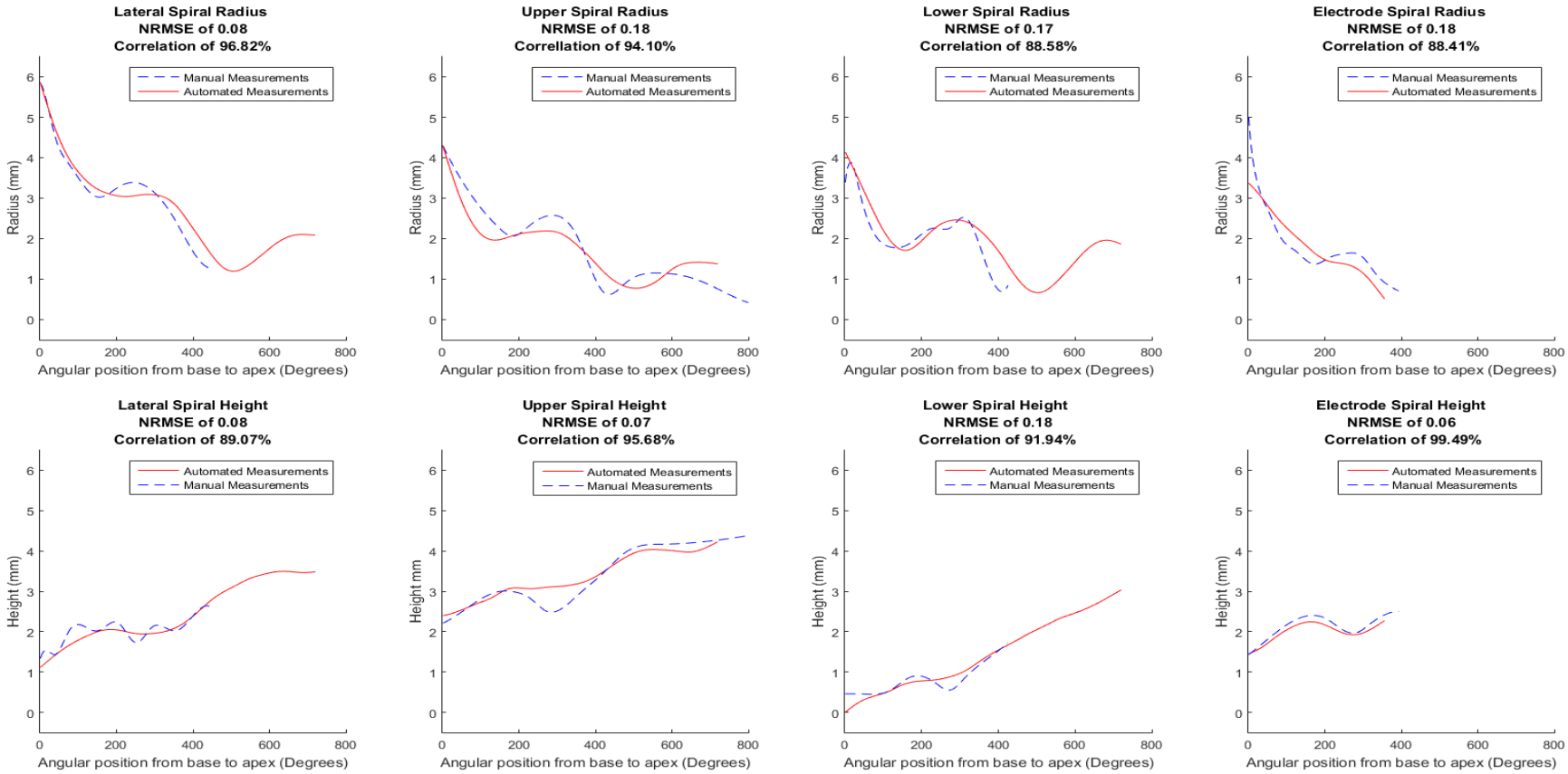

Figure 4.3 – Comparison of the measurements made with the manual and the automated methods of the three cochlear landmark spirals and the electrode spiral for user S13 L.

4.3.2. Deviations between automated and manual method measurements

Noticeable differences between the two measurement methods were also seen and identified on landmark spirals of markedly high NRMSE values and low correlation percentages, as highlighted in **Table 4.2** and **Table 4.3**. These differences and deviations are discussed further in the following section.

Figure 4.4 presents the comparison of results obtained for user S3 L. The highest NRMSE value was calculated for this user for the height measurement of the lower spiral, indicating the lowest similarity between the two methods. As seen on **Figure 4.4**, the lower spiral manual measurements were only done up to 345 degrees, possibly due to limited visibility of the lower spiral point to the naked eye, whereas the automated method was able to continue, as intensity-based thresholding is able to detect points not always visible to the naked eye. At 202 degrees, the radius of the lower spiral indicates a manually measured upper turning point, whereas the automated measuring method does not. The maximum absolute difference at this point is equal to 0.554 mm; this indicates that the automated method search field was either positioned closer to the modiolus or too small to detect any boundary points. The automated method is then required to interpolate across the range of valid detected points to predict the missing data entries, which does not always predict local turning points seen in the manual measurements. This relates to significant dissimilarities between the two methods and decreased correlation percentages.

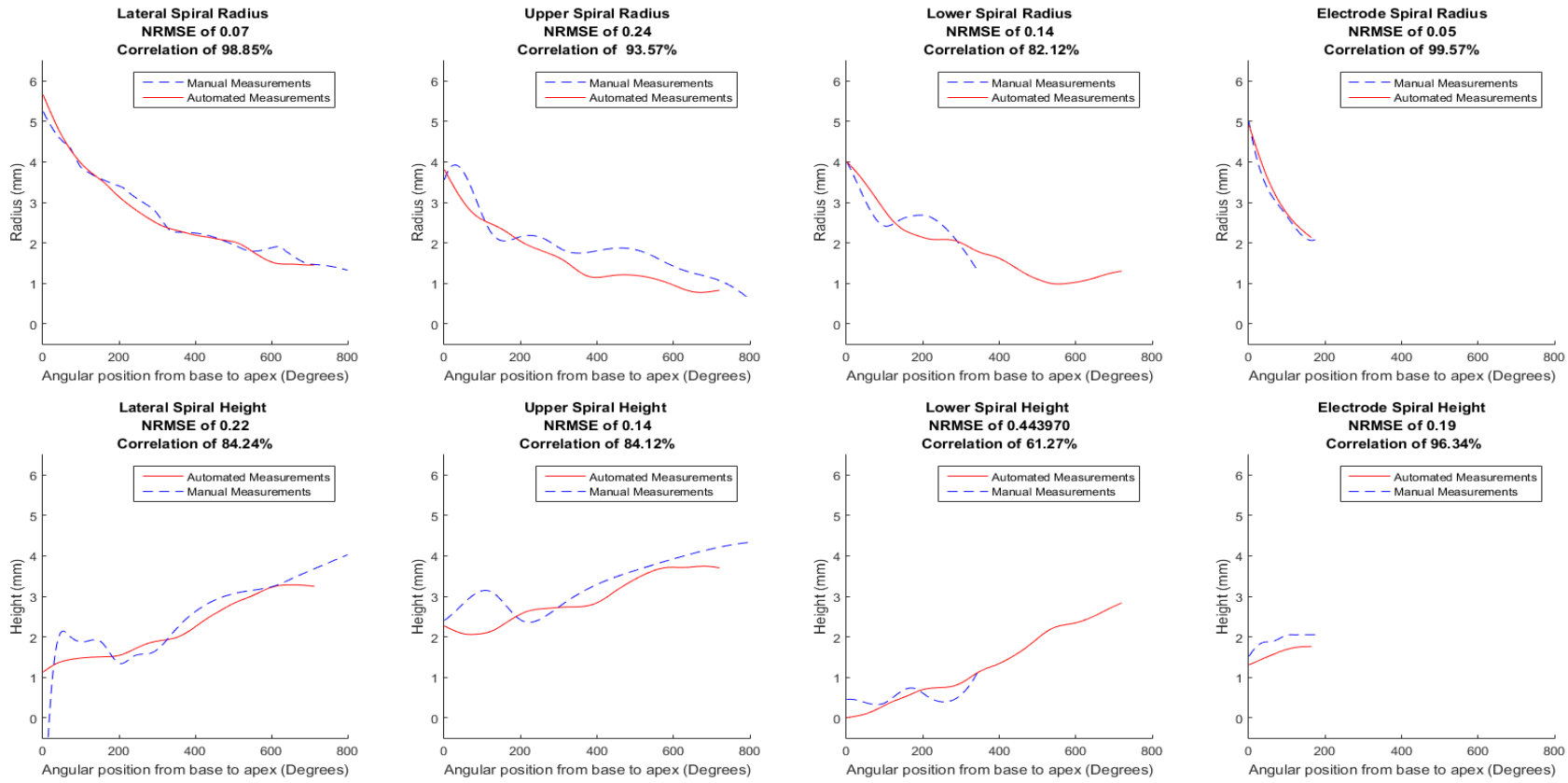

Figure 4.4 - Comparison of the measurements made with the manual and the automated methods of the three cochlear landmark spirals and the electrode spiral of user S3 L.

Figure 4.5 presents the comparison of results obtained for user S3 R. Two similar differences are seen for the lower spiral and the electrode spiral of this user, which is a low correlation percentage accompanied by a high NRMSE value on the same spiral. By viewing the information given in **Figure 4.5**, the lower spiral differences can be attributed to the poor visibility of the inferior boundaries of the cochlear wall, specifically at in the basal turn. The CT images show the inferior boundaries with interrupted visibility along the length of the basal turn. As a result, the automated method compensates for the interrupted visibility by either detecting points within the search fields that do not reflect the true inferior boundary of the cochlea, or interpolates across a range too large, resulting in deviations from manual methods of compensating for such situations. The electrode spiral differences are caused by the visibility of the electrode array just outside of the cochlea as it approaches the round window among the first 70 CT images. The electrode array is visible to the naked eye, but the artefact is too small to be detected by intensity-based thresholding. The missing data points are then predicted in the automated method with extrapolation, which do not always reflect such extreme trends in data as seen at the onset or end of the cochlea electrode array.

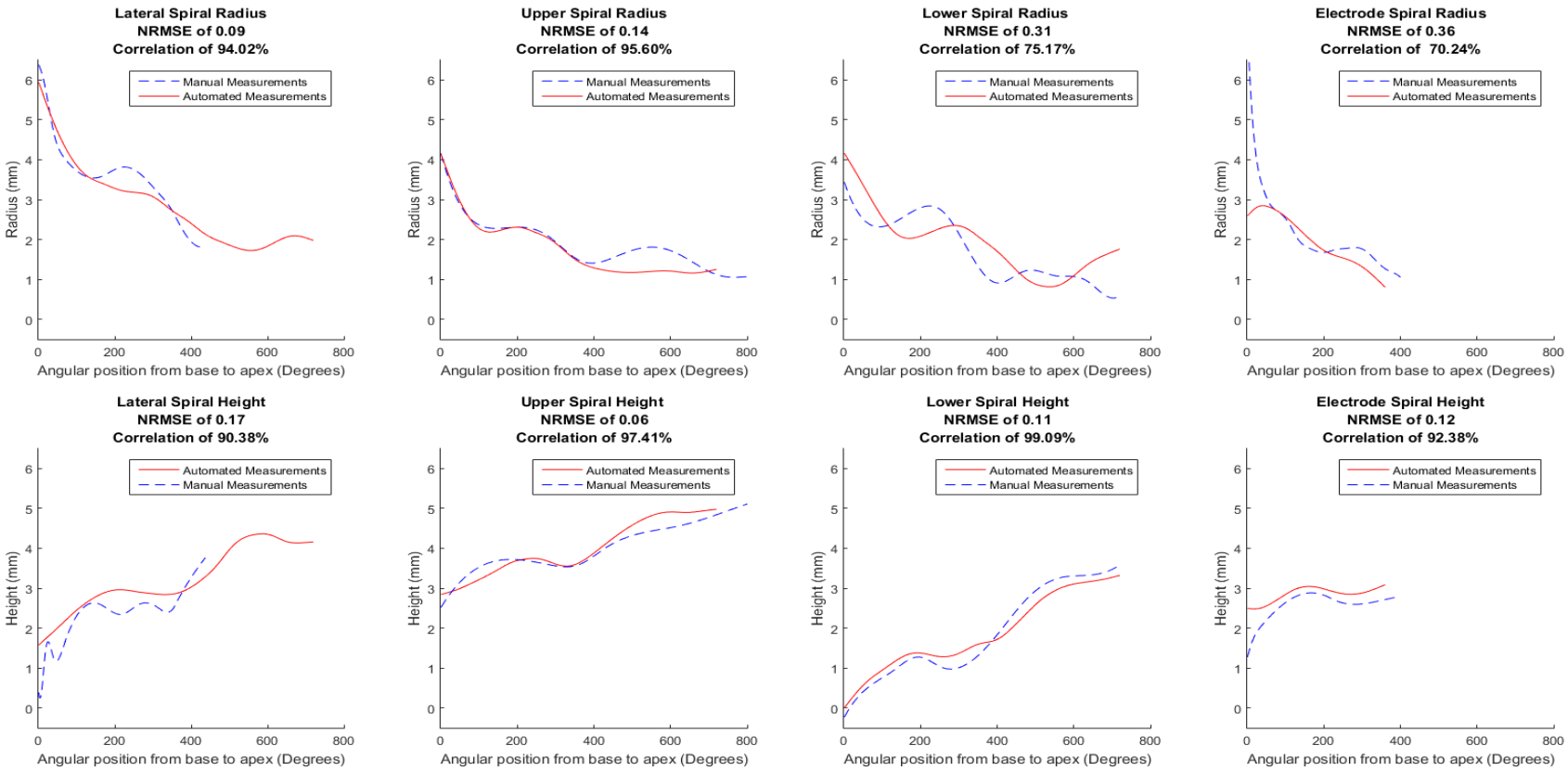

Figure 4.5 - Comparison of the measurements made with the manual and the automated methods of the three cochlear landmark spirals and the electrode spiral of user S3 R

Figure 4.6 presents the comparison of results obtained for user S30 L. The high NRMSE value calculated for the height profile of the lower spiral indicates dissimilarity among the measurement method. This dissimilarity is seen in measurements in the basal turn from 0 degrees to 200 degrees. The automated method detects a cluster of boundary points in the search field for which a mean coordinate is calculated. This mean coordinate is situated at the centre of the cluster, often positioned more superior to the more inferior points in the cluster. It can be observed in **Figure 4.6** that the turning points in the lower spiral height data trend resemble that of the manual measurements despite shallower turning points, allowing a 94.64% correlation despite the higher NRMSE value. The lower correlation percentage of the electrode array height measurement is the result of the intensity-based thresholding, which separates the layers of artefact intensity not always visible to the naked eye. This reveals the centre of the electrode array artefact with greater precision. A similar reason applies for the larger NRMSE and lower correlation percentage seen for the right ear cochlea electrode array for user S30.

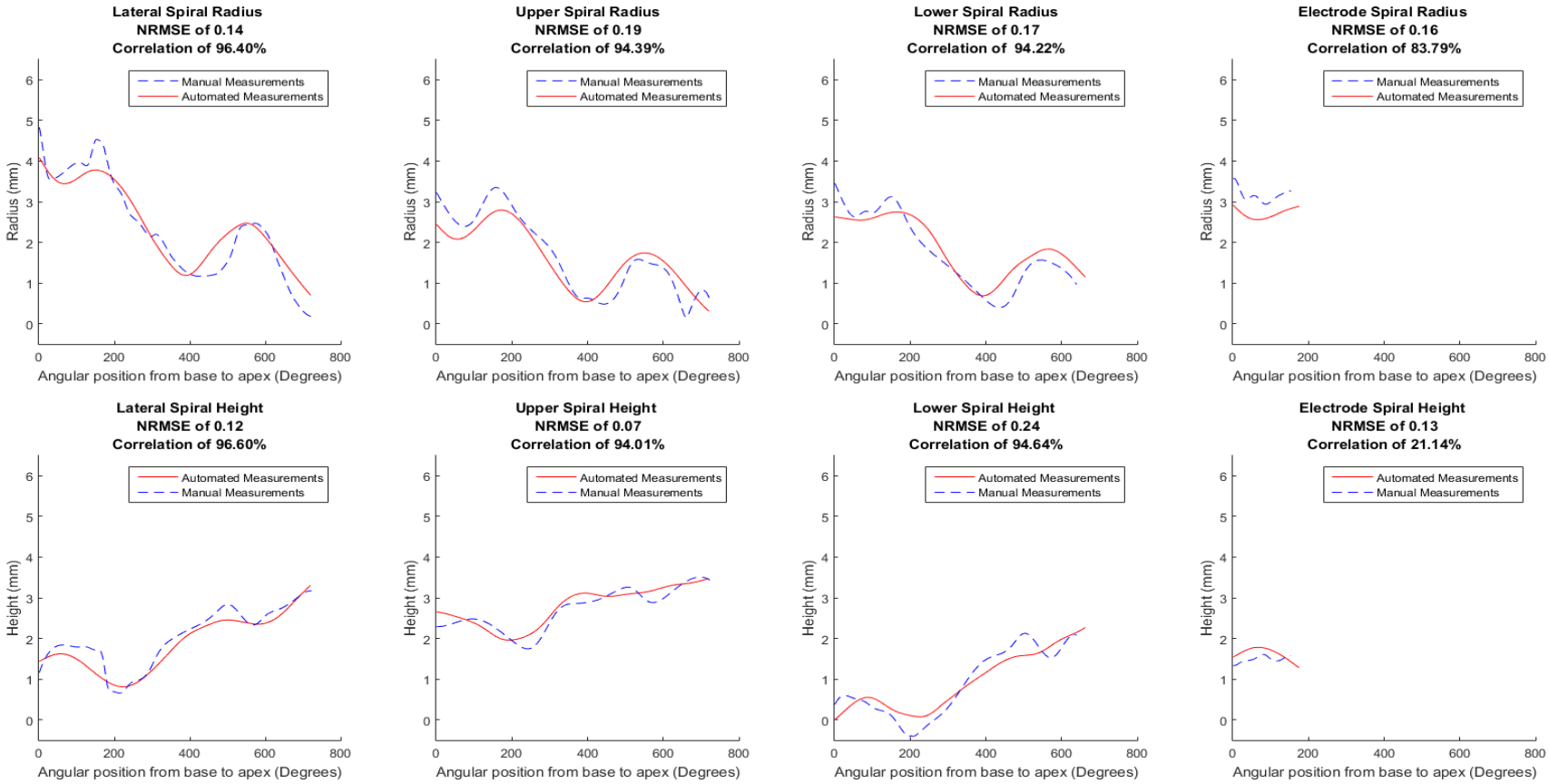

Figure 4.6 - Comparison of the measurements made with the manual and the automated methods of the three cochlear landmark spirals and the electrode spiral of user S30 L.

Figure 4.7 presents the comparison of results obtained for user S30 R. The higher NRMSE value seen for the lower spiral height in **Table 4.2** can be attributed to the automated method search field positioned in such a way that the actual boundary points are excluded from the search field, resulting in interpolation across valid points to predict such missing entries. By interpolating over a large range of data that does not indicate the promise of a turning point in data trend lines, such trend line features are then excluded.

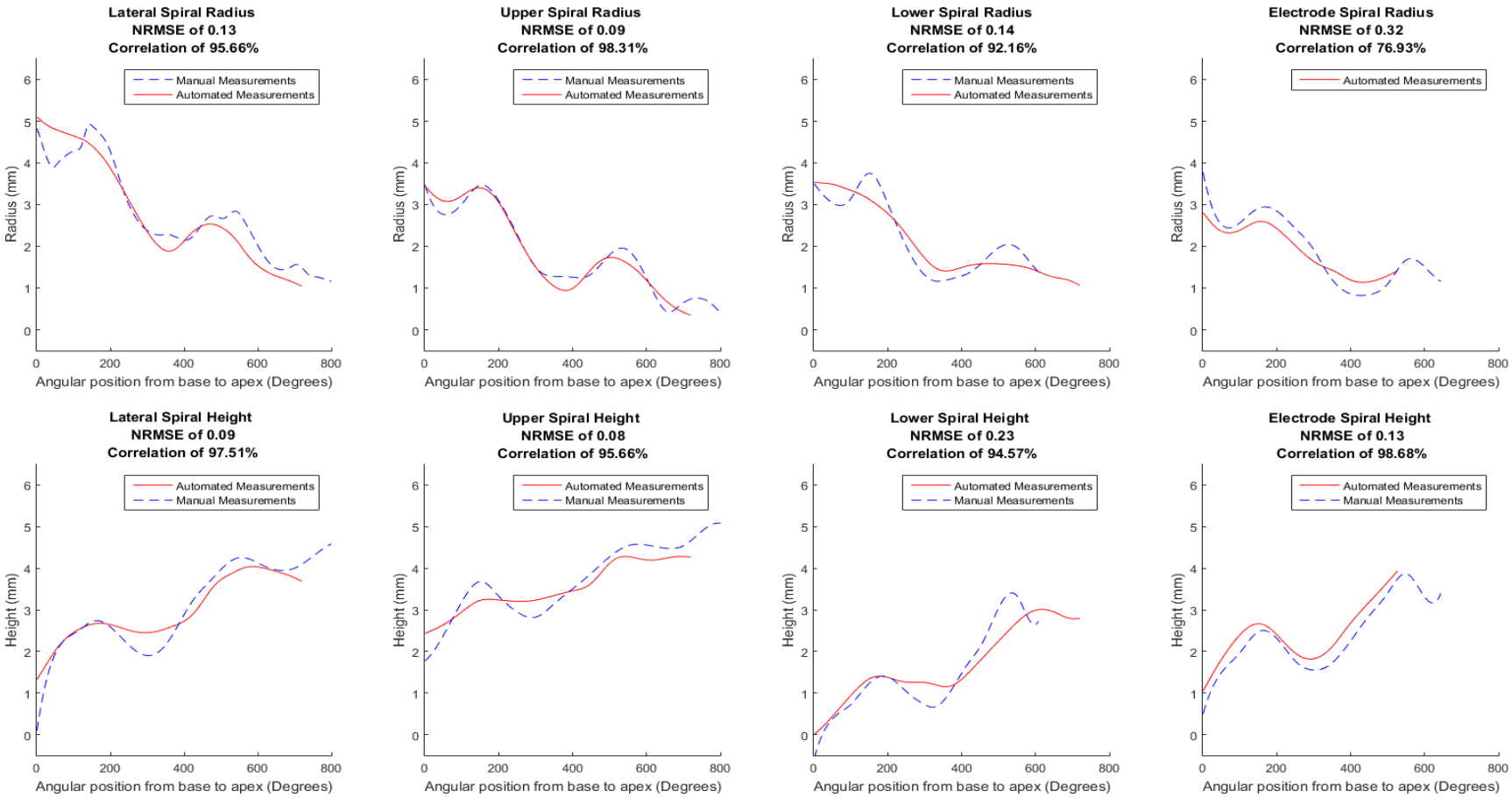

Figure 4.7 - Comparison of the measurements made with the manual and the automated methods of the three cochlear landmark spirals and the electrode spiral user S30 R.

In summary, the spirals that were best detected by the automatic method compared to the manual method were seen for user S13 L. This was due to decreased electrode artefact and improved visibility of the cochlear boundaries, which aided in distinguishing between the upper, lateral and lower landmark points. The worst detected spirals were seen for user S3 L, as a result of electrode artefact affecting the visibility of the cochlear boundaries.

4.4 GENERATED MODEL SIMILARITIES AND DIFFERENCES

Once the data processing was completed for each user, a COMSOL model was generated with both the automated and the manual measurement procedure.

4.4.1 Cochlea 3D geometry

One key difference between the manual and the automated model development methods is how the actual models are generated. The manual measurement method only utilises one of the three spirals, the lateral spiral, to find a best fitting template from a small database of cochleae. The automated measurement method however, incorporates all three measured spirals and adapts one template according to these three spirals through a Procrustes fit. The Procrustes fit involves the rotation, scaling and translation of each angular interval face of the template data to match the corresponding automatically measured landmark spirals.

By incorporating the upper and lower measured spiral in conjunction with the lateral spiral, a more detailed cochlea geometry can be defined. By evaluating the 3D geometries of the cochlear models created with each method for each user, the following results were obtained.

A smaller cochlea cross-sectional area was seen through the use of the Procrustes fit, which aims to adapt the lateral, upper and lower spirals of the template data to match the measured landmark data. **Figure 4.8** depicts an example of the cross-sectional view of the cochlea at 0 degrees for the automated method model for the left ear cochlea of User S13. This decrease in cross-sectional area of the cochlea is visible along the entire length of the cochlea.

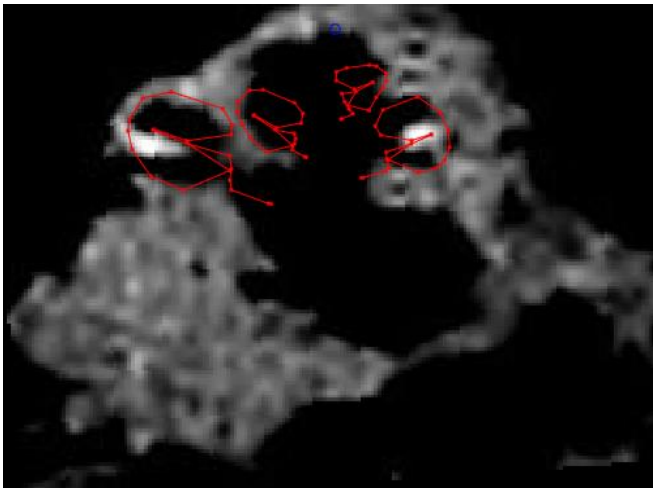

Figure 4.8 – Cross-sectional view of the combined cochlea models generated with the automated method at 0 degrees of user S13 L

This decrease in the cross-sectional area also leads to a reduction in the volume of the automated models, as can be seen in **Table 4.4** below. The volumes of the cochlear models generated with the automated method are markedly lower than the manually created models. The reduced volume resulted in a higher combined resistance of the model, which resulted in increased electric potentials under constant electric stimulation conditions, compared to the manually created models.

Table 4.4 – Predicted volumes of cochleae based on the 3D models for the automated and manual methods

	Volume (mm^3)	
User model	**Automated Method**	**Manual Method**
S13 L	76,98	159,8
S13 R	83,51	164,9
S3 L	65,82	139,3
S3 R	92,41	173,33
S30 L	84,84	172
S30 R	122,6	223,7

Research has also shown that as one moves along the length of the cochlea toward the apex, the cochlear inner structures tend to rotate inwards, towards the centre of the cochlea (Gibson et al., 2012). By using all three landmark spirals, rather than only one, to scale

and rotate the template models, detail such as the rotation of the cochlear structures along the length of the cochlea, become more visible.

4.4.2 Electrode Geometry

All geometrical data used to recreate the electrode arrays with the automated method was obtained from the data comparison sheet created by Cochlear™ Ltd (Cochlear.com, 2016), which contains the cochlear implant geometrical information of all the relevant electrode arrays used in this study. The comparison sheet includes geometrical properties for cochlear implants from Med-El, Cochlear™ Ltd and Advanced Bionics®.

The Contour Advance Electrode array from Cochlear™ was implanted the following users, and recreated in their respective 3D models.

- S13 L and S13 R
- S3 L and S3 R

All of the above-mentioned models had a carrier base and apex diameter of 0.8 mm and 0.5 mm, respectively. Both models possessed half band type contact bands. With the automated method, each contact plate width was 0.25 mm with a carrier width of 0.45 mm between electrode contact points, up to an electrode length of 8 mm starting from the most apical point of the electrode. After 8 mm, the carrier width between electrodes decreased to 0.4 mm with an electrode contact width of 0.3 mm. The manual method electrode contact widths remained constant throughout the entire length of the electrode at 0.3 mm with a constant carrier width between each electrode contact of 0.5 mm.

The Combi Compressed electrode array from Med-El was implanted and recreated in the 3D model for the left ear cochlea of user S30 L. The manual method models selected a constant carrier diameter of 0.5 mm from the base to the most apical point of the electrode array. The electrode contact points for this series of Med-El electrode arrays are round contact plates and were recreated as cylindrical entities of 0.2 mm diameter. The carrier width between two electrodes was equal to 0.9 mm. These measurements did not correlate with the dimensions given on the electrode array comparison page, as the carrier width

between electrodes are equal to 0.7 mm with a 0.3 mm diameter for the electrode contact face. Despite the differences on the comparison sheet, from the CT scan superior view, only 7 electrodes were clearly visible inside the cochlea. These differences could be the result of a previous electrode array design implanted in the user with a revised design given on the electrode array geometrical data source.

The electrode array produced by the automated model had a selected apical carrier diameter of 0.5 mm and a basal diameter of 0.9 mm, with the intermediate diameters determined through linear interpolation. The circular face of each electrode contact was modelled with a diameter of 0.3 mm. In order to keep the number of electrodes inside the cochlea consistent with that of the manual measurement method, the carrier width between the electrode contacts were also changed from 0.7 mm to 0.9 mm. By making this change, both the automated and the manual method electrode arrays contained 7 electrodes.

The right ear cochlea of the user S30 R contained a Combi 40 Medium implant from Med-El. The same electrode array was recreated in the 3D Model. The manual measurement method recreated the Med-El electrode array with a 0.2 mm diameter electrode contact and a carrier width of 1.82 mm. The carrier width used in this model differs from the width indicated on the electrode array comparison data sheet of 1.5 mm. The electrode carrier diameter also remained constant at 0.5 mm along the length of the array in the manual method model. The electrode contact diameter of 0.3 mm, and a carrier width between electrodes of 1.5mm was measured from the data comparison sheet. The diameter of the electrode carrier increases linearly from 0.5 mm at the most apical point, to 1 mm at the most basal point.

4.4.3 Electrode Pathway

The following section discusses the similarities and differences between the two methods regarding the electrode trajectory relative to the cochlear internal structures.
The electrode trajectory for the following users followed a similar path relative to the internal structures of the cochlea.

- User S3 L - The electrode array is located primarily in the Scala Vestibuli, closer to the later wall of the cochlea rather the spiral ganglion. Trauma is observed along the length of the of the cochlea as the electrode array pierces trough Reissner's membrane, with a small part of the electrode array cross section visible in the Scala Media. The deepest points of the electrode array extend upwards into the Scala Vestibuli. The automated model bares close resemblance to the pathway followed by the manually created electrode array. The electrode array is located very close to the lateral wall of the cochlea in the upper region, closer to the Scala Vestibuli, causing trauma to spiral ligament and the stria vascularis, initially. As the electrode extends deeper into the cochlea, the array turns further into the Scala Vestibuli, away from the lateral wall towards the centre of the cochlea.
- User S3 R - The electrode array created with the manual method maintains a pathway in the Scala Vestibuli throughout the entire length of the electrode array. At the most basal point, the electrode array is closer to the lateral wall of the cochlea. As the electrode extends deeper into the cochlea, slight trauma is caused to Reissner's membrane and the spiral ligament. The electrode array turns inward, closer to the modiolus as the array extends deeper in the apical region of the cochlea. The electrode array generated with the automated method follows a very similar path to its manually created counterpart. At the most basal point of the cochlea, the electrode is located inside only the Scala Vestibuli, closer to the lateral wall of the cochlea as opposed to the modiolus, with no trauma present at this stage. As the electrode array extends deeper into the cochlea, trauma is caused to Reissner's membrane and the spiral ligament; although damage is minor, it is still visible. The electrode array also moves away from the lateral position and closer to the modiolus as it extends into the more apical regions of the cochlea, very similar to the pathway described for manual method electrode array.
- User S13 L - At the most basal point of the electrode array created with the manual method, the electrode is located in the Scala Vestibuli. At this initial position, the array is closer to the lateral wall of the cochlea, causing trauma to Reissner's membrane and extending into the Scala Media. As the electrode array extends

deeper into the cochlea, the trauma visibly reduces to none and the array itself turns away from the lateral wall and moves closer to the modiolus of the cochlea. The automated method electrode array follows a very similar pattern although the trauma seen at the onset of the array at base of the cochlea is slightly different. The visible trauma is seen in a small region of the most lateral points of the auditory nerves as well as in Reissner's membrane. As the array extends further into the cochlea, the electrode is located in the upper region of the Scala Vestibuli with visibly less trauma. Closer to the more apical regions of the cochlea, the electrode array turns away from the lateral side of the cochlea and moves inwards, closer to the modiolus of the cochlea.

- User S13 R - The manually created electrode array is initially located in the lateral section of the Scala Tympani, with no visible trauma present. The electrode array remains in the lateral region of the Scala Tympani and extends towards the lower lateral region of the cochlea. The electrode array protrudes the Scala Tympani lateral wall at the array's deepest point. By protruding the lateral wall of the cochlea, the electrode is located outside of the cochlea. The electrode array generated with the automated method is located in the upper lateral region of the Scala Tympani at the most basal point of the cochlea, with no visible trauma present. When evaluating the electrode array deeper inside the cochlea, the array starts to slowly traverse towards the lateral region of the Scala Vestibuli and protrudes through the organ of Corti, the basilar membrane, Reissner,s membrane, and a small section of the most lateral auditory nerve sections.

The following users showed noticeable differences in electrode trajectory, relative to internal structures between the manual and automated methods.

- User S30 L - The electrode pathway followed in the manually created model also travels only in the Scala Tympani with no trauma caused to the cochlea. The electrode is located closer to the modiolus of the cochlea rather than the lateral walls, with seven electrode contacts present inside the cochlea. The electrode array in the automated model is located at a centralised position closer to the lateral wall

of the cochlea. Trauma is visible in the Spiral ligament, the basilar membrane, a small part of the auditory nerve, and the stria vascularis as well as Reissner's membrane. The electrode then traverses upwards into the Scala Vestibuli where the majority of the electrode cross-section remains until the electrode array terminates at 178 degrees. Minor trauma is caused to Reissner's membrane and the stria vascularis further along the length of the cochlea.

- User S30 R - The electrode trajectory created with the manual process remains inside the Scala Tympani with no translocation into the neighbouring scalae. However, the trajectory of the electrode generated with the automated process differs notably from that of the manually generated array. The electrode array at the basal turn is more centrally located than the manually generated array with the larger majority of the electrode face in the Scala Tympani and the lesser area in the Scala Vestibuli. Along the length of the cochlea, the electrode traverses completely to the Scala Vestibuli and then travels back down to a more centralised position, similar to what was seen at the basal turn. The automated model indicates a great deal more trauma present within the cochlea as the more centralised position causes damage to the Scala Media, the basilar membrane, organ of corti and some of the smaller membranes. When the electrode traverses to the Scala Vestibuli and back down to the more central position, trauma is caused to the basilar membrane and auditory nerve extensions.

Due to poor visibility, the internal structures of the cochlea cannot be determined directly from CT images, but require data fusion to estimate the structures' positions relative to the landmark spirals. The poor visibility of the internal structures further complicates model development as the electrode position cannot be determined by simple inspection of the CT image and must also be defined by estimating the position. As surgeons aim to reduce trauma during the insertion of an electrode array, it is not completely avoidable. The main differences between the manual and automated methods are the assumptions made regarding the electrode array trajectory and its position relative to the cochlear internal structures. The manual method aims to reduce overlapping of existing structures in the cochlea model by adjusting the position of the electrode in such way as to minimise trauma

throughout the travel distance of the cochlea. The automated method does not aim to reduce or increase the trauma, but rather ensure that the position of the electrode array relative to the measured landmarks is maintained. The electrode trajectory differences seen between the two methods for user S30 is a clear indication of the effect of the two different approaches.

4.5 NERVE FIBRE POTENTIALS AND ACTIVATING FUNCTION PREDICTIONS

4.5.1 Background information

After the various models were created in COMSOL, a parametric sweep simulation was completed for each model. The simulation involved the creation of a variable for each of the electrode contact points located inside the cochlea. The variables were labelled as ‘e1’, representing the most basal electrode contact point, up to a value of ‘e22’, representing the deepest or most apical electrode contact point. The deepest electrode contact point variable name is dependent on the number of electrodes inside the cochlea. The ‘Electric Current’ Physics equations were used in each of the relevant models, which enabled the assignment of current sources to specific points in the model. These points were selected to each be on an electrode contact point with the value equal to the variables assigned to each respective contact point. By doing so, a scenario could be simulated where each electrode contact point would be turned on individually, with all remaining electrode contact points turned off. The sphere surrounding the cochlea was modelled as an infinite element and acted as the electric ground source in the simulation. For the electrodes that were turned on in each instance, a value of 1A was assigned, with 0A assigned to the remaining electrodes.

Once all the model simulations were completed, the electric potentials were extracted at specific coordinates along the length of the nerve fibres for each simulation. Each model consists of an internal structure defined as the nerve fibre. A radial cross-sectional view of this structure is given in **Figure 4.9**. This structure runs along the length of the cochlea from base to apex and when viewed in isolation, the structure can be rolled out into one flat

surface. In this rolled out view, the axon of the nerve fibre is located closer to the inferior edge and the dendrite is located closer to the superior edge with the soma region located between these two sections. For each model, the nerve volume was divided into 444 equally spaced nerve fibres along the length of the cochlea. Each of the nerve fibres consisted of 47 nodes at specific lengths along the nerve fibres, representing the dendrite, soma and axon locations along the length of the nerve fibre itself, obtained from the work of Rattay et al. (2001). **Figure 4.9** gives an example of the nerve fibre nodes located in the cross-section of the nerve fibre. The potential distribution is of importance as it aids in estimating which nerve fibres are most likely to fire.

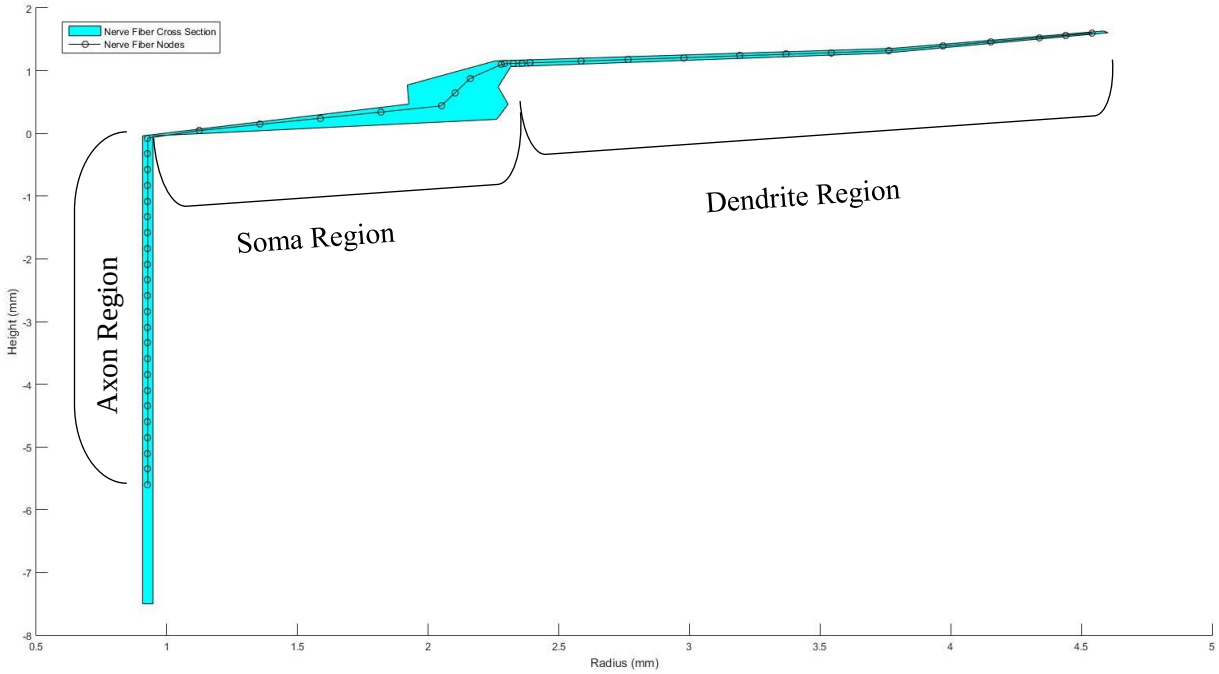

Figure 4.9 – Cross-sectional view of the nerve fibre volume and the nerve fibre nodes locations and regions

To investigate the effect of potential distribution across the nerve fibres, one must look at the level of nerve fibre excitement and stimulation. The stimulating influence of an extracellular potential along the length of a nerve fibre is given in equation (4.1) below, known as the activating function. The activating function is only used to give an indication of the predicted neural excitement, for comparison between the automated and manual method models. This approach does not incorporate the intensive calculations used within

a full active membrane neural model, but is useful in providing insight into predicted neural excitation.

$$f = \frac{V_{e,n-1} - 2V_{e,n} + V_{e,n+1}}{\Delta x^2} \tag{4.1}$$

The activating function f is the second order derivative of the extracellular potential along the fibre and is used as a first approach to determine the influence of extracellular electrodes on nerve fibres, as the value f is responsible for activating a fibre by extracellular electrodes (Rattay, 1989, Rattay, 1999). The value V_e represents the extracellular potential produced by the stimulating electrode, with n representing the segment at which the extracellular potential is measured with Δx the value of the equally spaced nerve fibre node distances.

By dividing the nerve fibre nodes into equally space nodes along the length of the fibre, the potentials could then be used in equation (4.1). When evaluating the various models and their activating function values f, one can gain further insight into the nerve fiber activity produced as a result of such stimulation cases. For activating function values of $f > 0$, the extracellular electrode shows a higher probability of exciting the fibre at that segment. The highest value of the activating function is also a good indicator of the compartment, which is most likely to be excited generally, although isolated activating function spikes may not cause excitation.

Through inspection of the activating function values across all nerve fibres for each simulation of each stimulation case, one could also determine the nerve fibres on which the most compartments are excited (Rattay, 1989, Rattay, 1999).

4.5.2 Electric potential and activating function predicted distributions

The potential distribution plots obtained from the electric stimulation of the respective models are shown in **Figure 4.10** to **Figure 4.15**. Since each model was subjected to monopolar stimulation, the potential distribution of only the most basal, middle and most apical electrode stimulations are given for convenience.

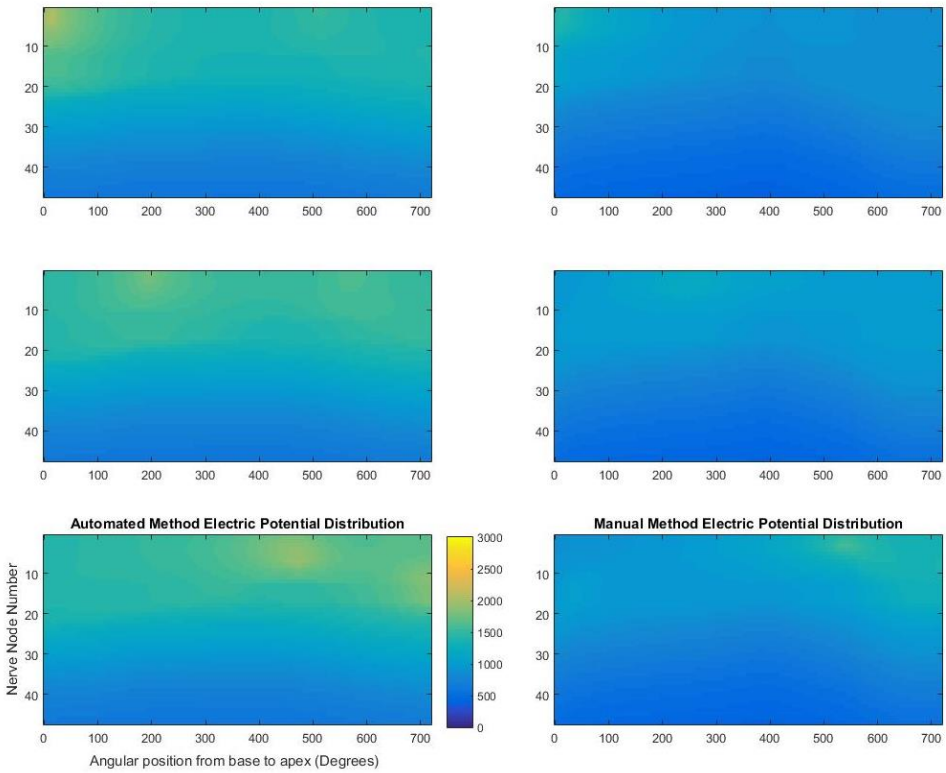

Figure 4.10 – Simulated electric potential distribution as a result of electrical stimulation of the 3D cochlea model with electrode e1 (top row), e11 (middle row) and e22 (bottom row). The cochlea model used in the simulation was user S13 L. The scale on the figure indicates the values in Volts (mV).

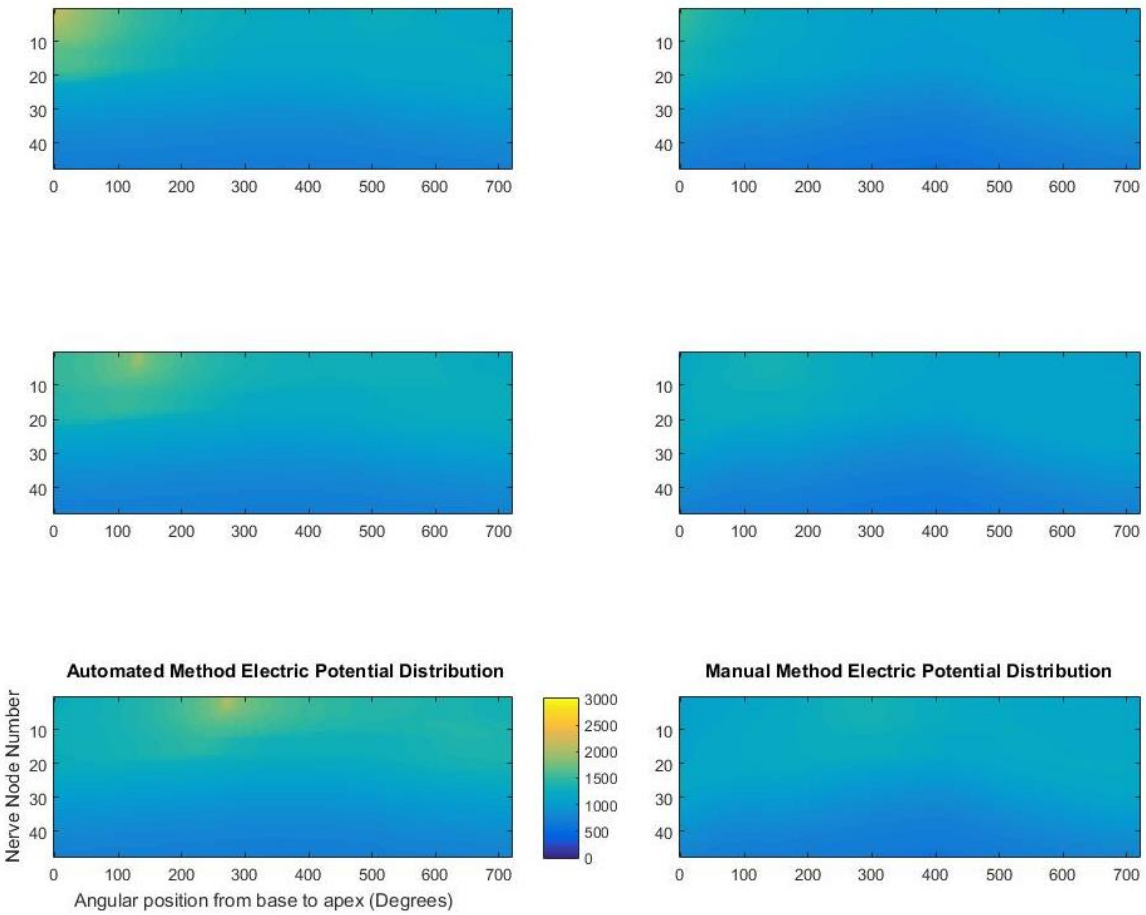

Figure 4.11 - Simulated electric potential distribution as a result of electrical stimulation of the 3D cochlea model with electrode e1 (top row), e8 (middle row) and e17 (bottom row). The cochlea model used in the simulation was user S13 R. The scale on the figure indicates the values in Volts (mV).

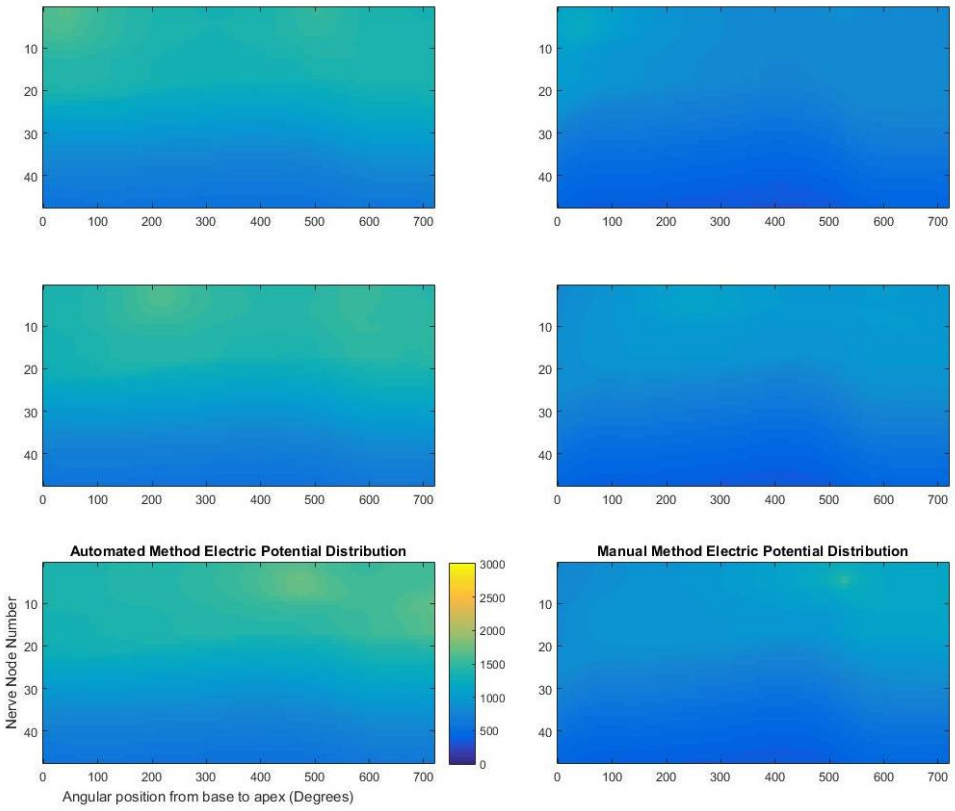

Figure 4.12 - Simulated electric potential distribution as a result of electrical stimulation of the 3D cochlea model with electrode e1 (top row), e11 (middle row) and e22 (bottom row). The cochlea model used in the simulation was user S3 R. The scale on the figure indicates the values in Volts (mV).

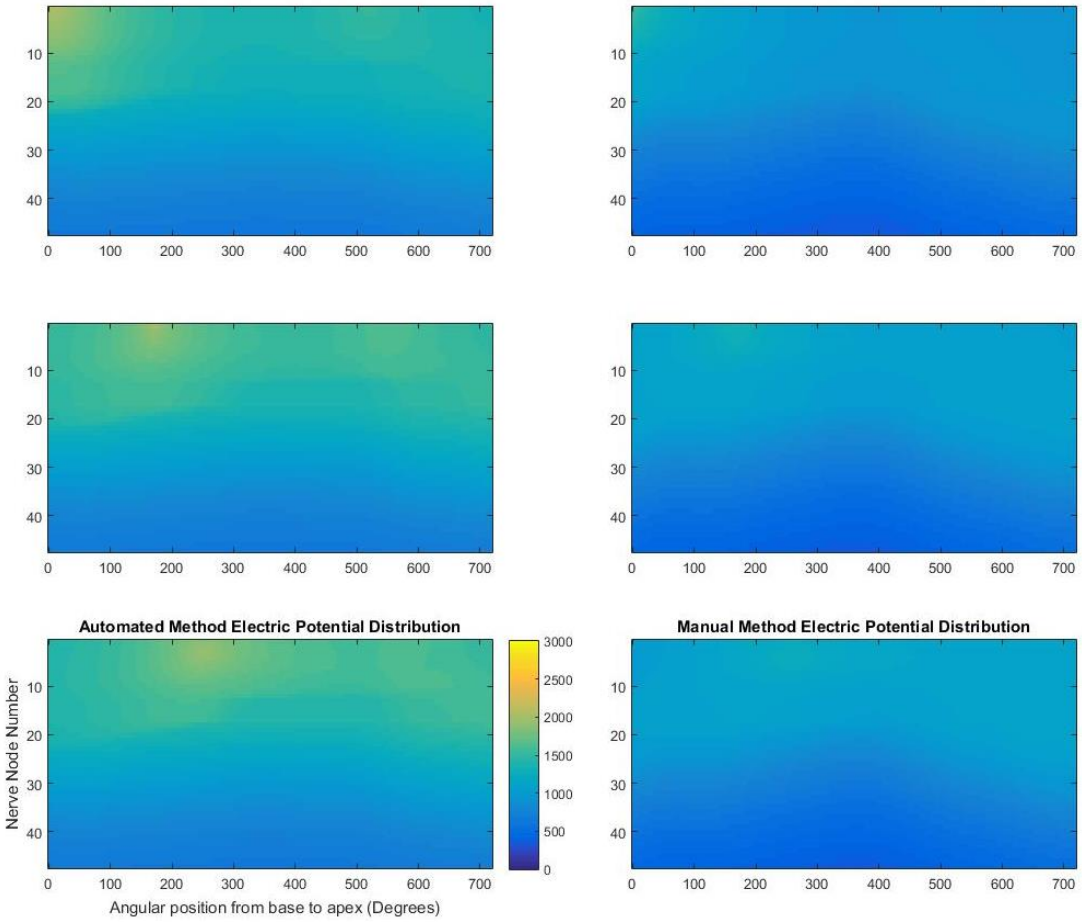

Figure 4.13 - Simulated electric potential distribution as a result of electrical stimulation of the 3D cochlea model with electrode e1 (top row), e8 (middle row) and e15 (bottom row). The cochlea model used in the simulation was user S3 L. The scale on the figure indicates the values in Volts (mV).

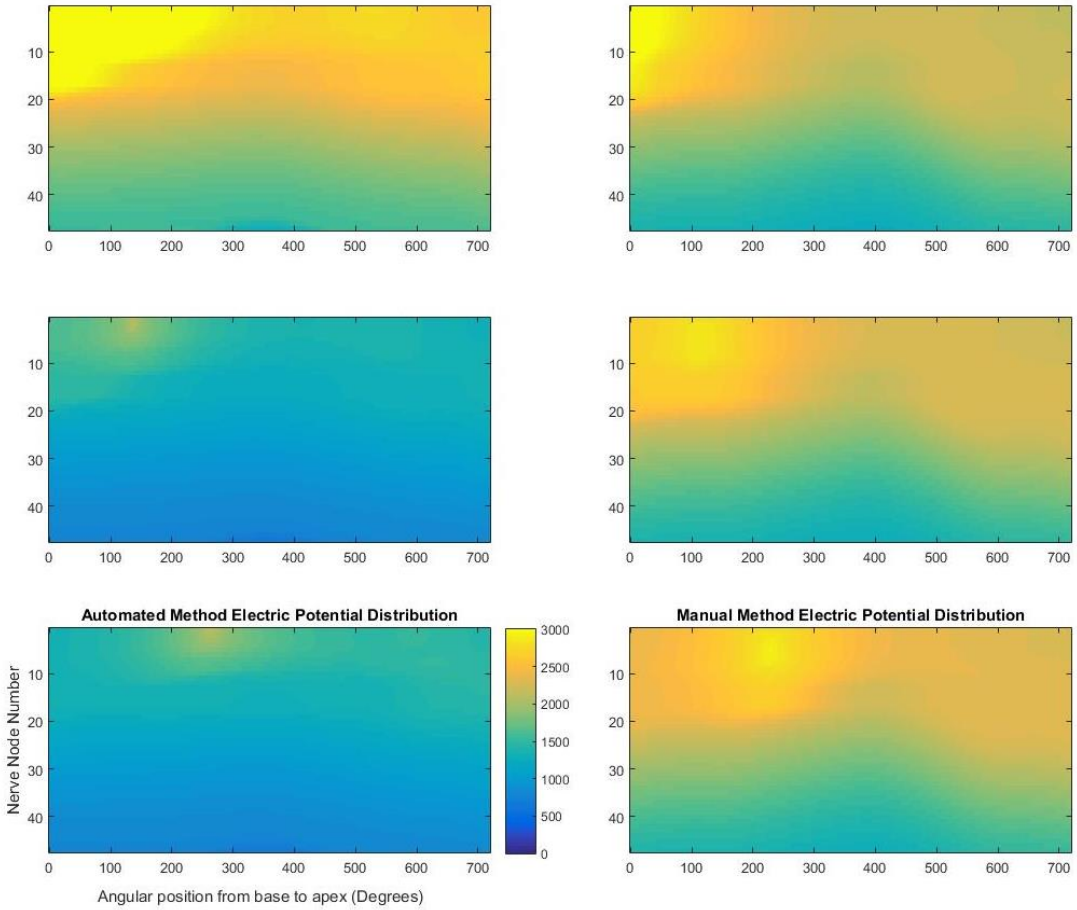

Figure 4.14 - Simulated electric potential distribution as a result of electrical stimulation of the 3D cochlea model with electrode e1 (top row), e4 (middle row) and e7 (bottom row). The cochlea model used in the simulation was user S30 L. The scale on the figure indicates the values in Volts (mV).

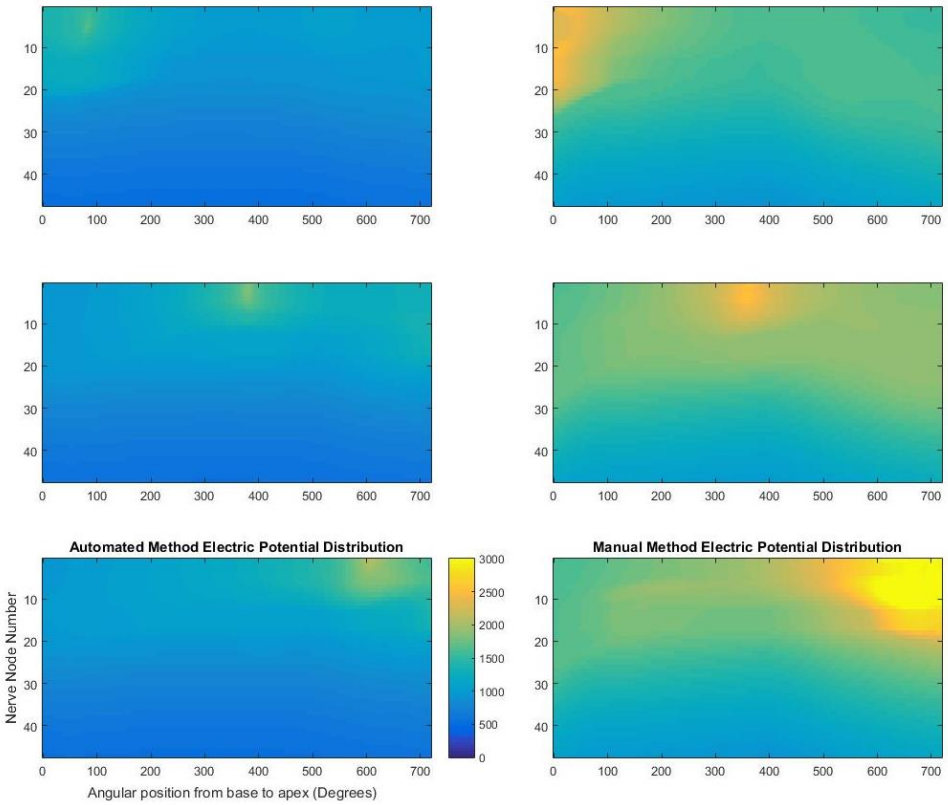

Figure 4.15 - Simulated electric potential distribution as a result of electrical stimulation of the 3D cochlea model with electrode e1 (top row), e6 (middle row) and e12 (bottom row). The cochlea model used in the simulation was user S30 R. The scale on the figure indicates the values in Volts (mV).

The monopolar stimulation cases indicated that the potentials predicted by the automated method models were higher than that of the manual method models for all models of users S13 and S3, while the manual models for user S30 showed higher potentials. The higher potentials seen in the results of user S30 may be attributed to i.) the method in which the metallic electrode contacts were modelled and ii.) the different application of stimulation applied in the manual method models. At each electrode contact position, the metallic contact was modelled as two separate cylinders, one superior and one inferior. During simulation, a node current was applied on each cylinder instead of one single point, which resulted in higher current stimulation. The higher potentials predicted in the automated models may be attributed to lower volumes of the automated method models when compared to the manual method models. A smaller cochlear volume results in a larger

combined resistance for the cochlea, which in turn causes a higher potential under constant stimulation conditions.

The location of highest potentials in both the automated and the manual method models bared close resemblance as a result of the electrode array contact point locations. To further investigate this resemblance, the nerve fibre number with the highest electric potential was determined for each model of each user, as depicted in **Figure 4.16**.

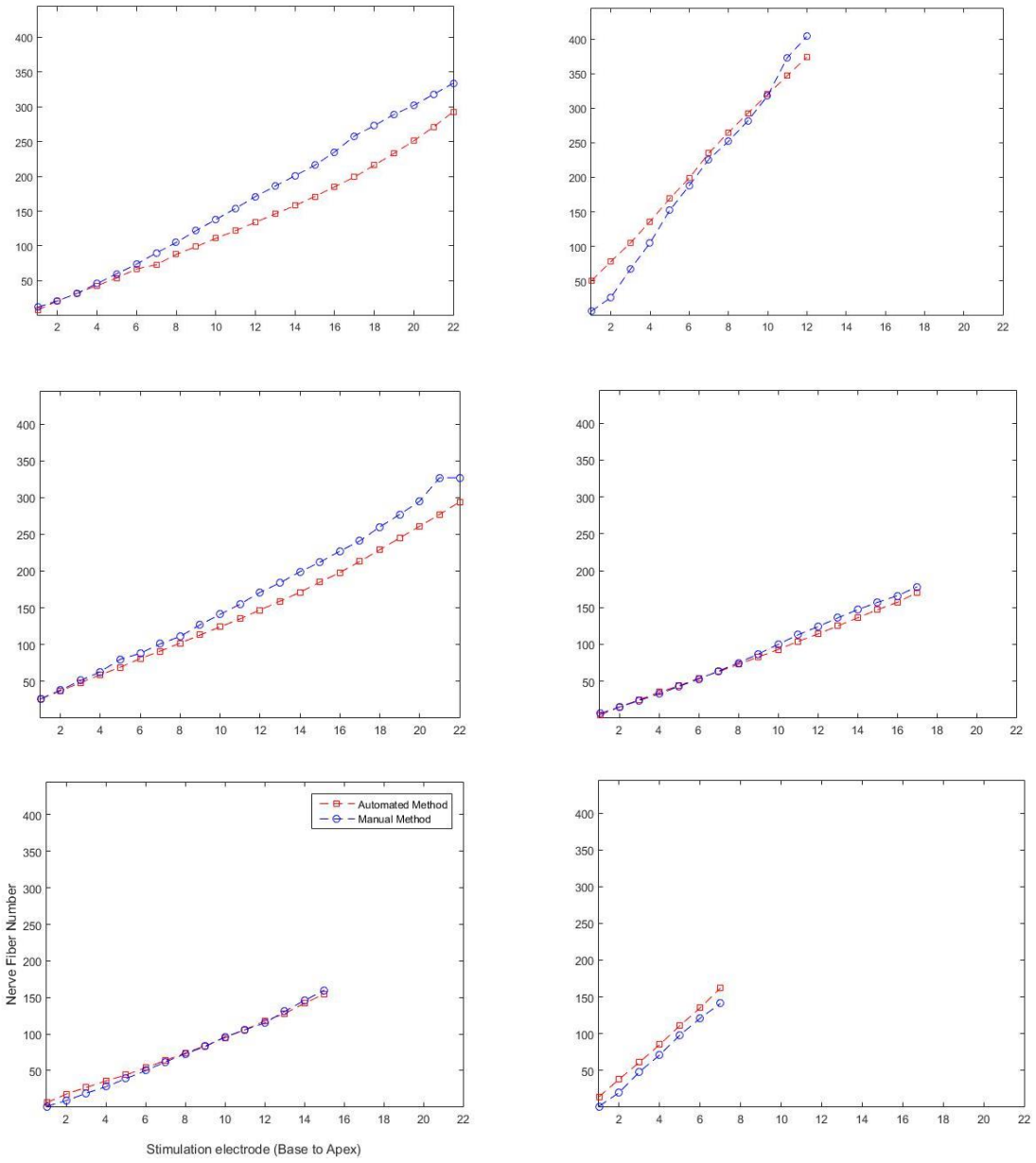

Figure 4.16 - The nerve fibre number with the highest electric potential as a result of monopolar stimulation of each electrode for each model, user S13 L (top left), user S30 R (top right), user S3 R (middle left), user S13 R (middle right), user S3 L (bottom left) and user S30 L (bottom right).

The differences viewed in the location of highest potential can be attributed to the differences in the location of the stimulating electrode between the automated and manual method. As the position of the stimulating electrode is determined from both the geometrical properties of the type of electrode array and the insertion depth of the array

inside the cochlea, the resultant effect of the differences between the two methods can be seen in **Figure 4.16**.

Figure 4.17 to **Figure 4.22** depict the activating function values calculated from the potential distribution predictions, including the activating function values at each node along the length of each cochlear nerve fibre (seen as values ≤ 0 mV/μm^2).

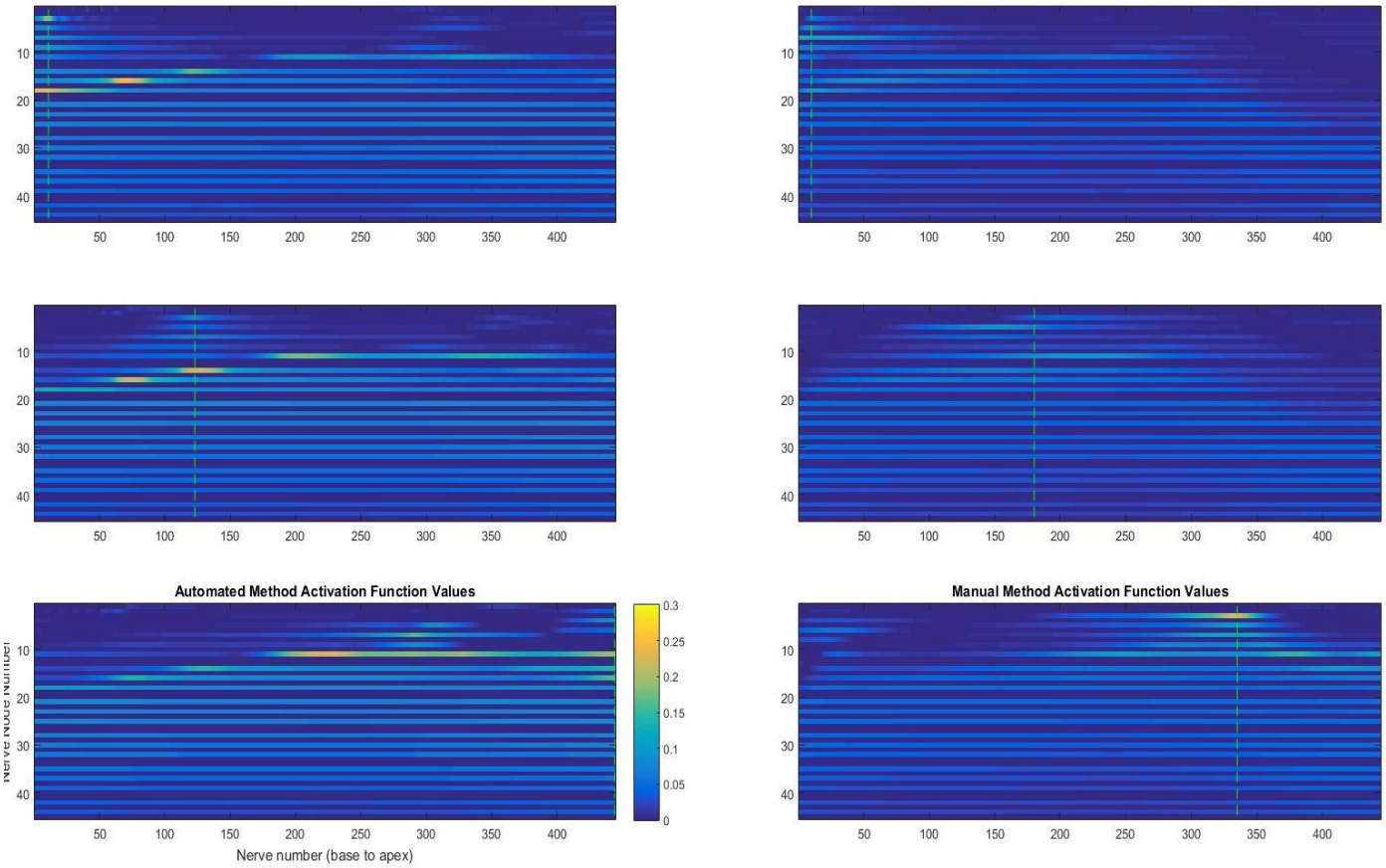

Figure 4.17 - Simulated activating function distribution across the nerve fibres as a result of electrical stimulation by electrode e1 (top), e11 (middle) and e22 (bottom). These results are shown for both the automated (left) and manual (right) methods. The results were obtained from the model created for user S13 L. The scale on the figure indicates the values in $mV/\mu m^2$.

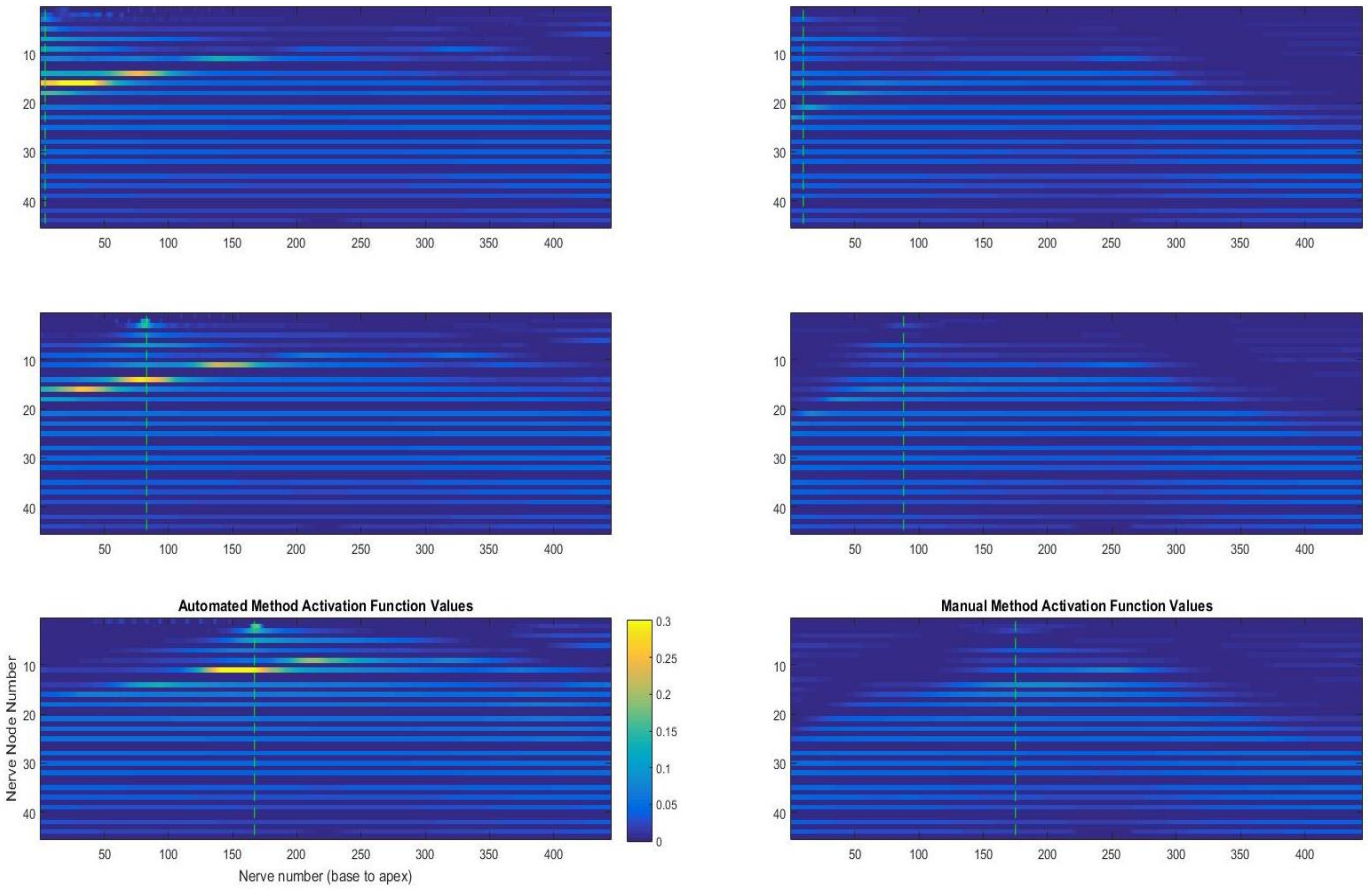

Figure 4.18 – Simulated activating function distribution across the nerve fibres as a result of electrical stimulation by electrode e1 (top), e8 (middle) and e17 (bottom). These results are shown for both the automated (left) and manual (right) methods. The results were obtained from the model created for user S13 R. The scale on the figure indicates the values in $mV/\mu m^2$.

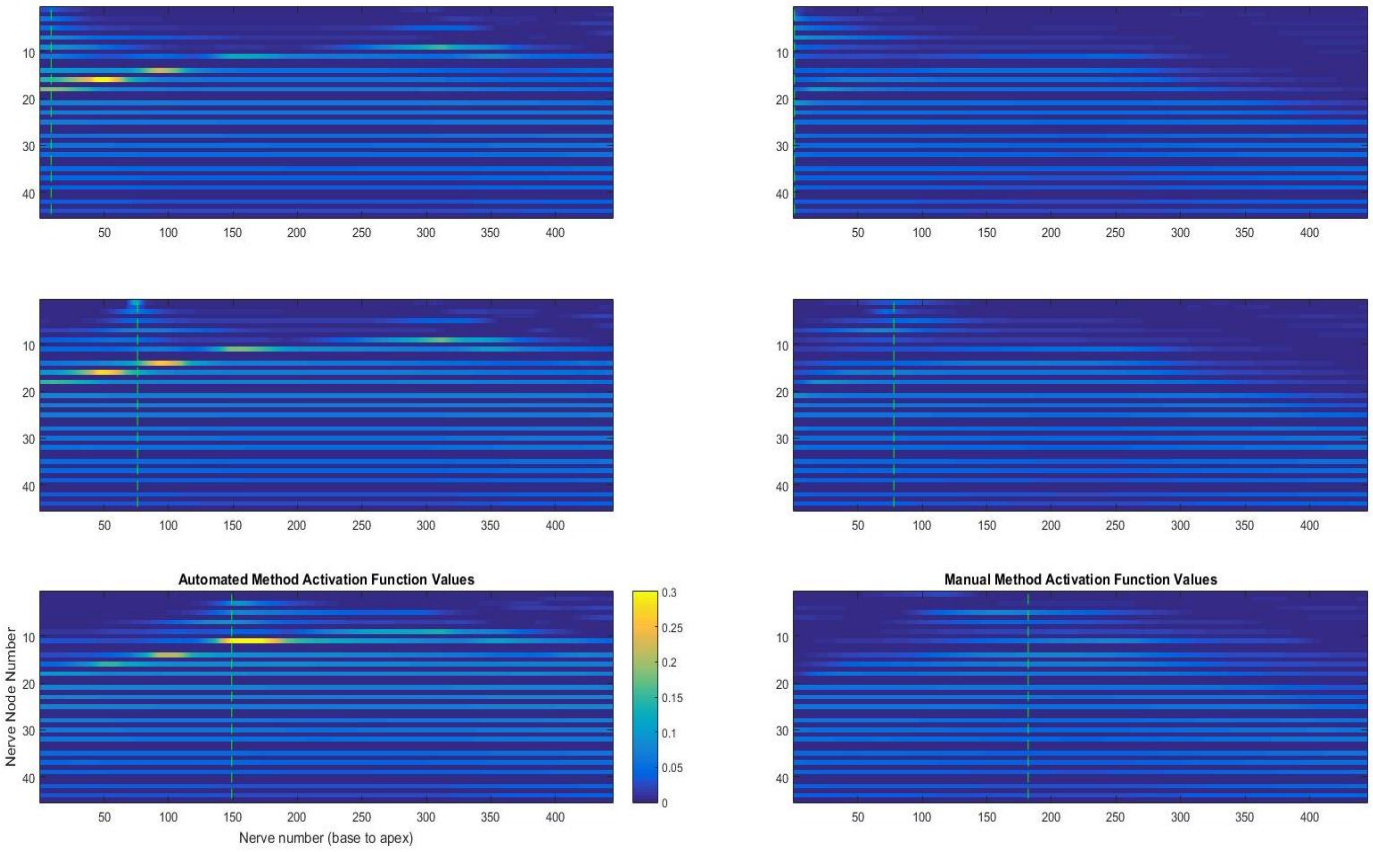

Figure 4.19 - Simulated activating function distribution across the nerve fibres as a result of electrical stimulation by electrode e1 (top), e7 (middle) and e15 (bottom). These results are shown for both the automated (left) and manual (right) methods. The results were obtained from the model created for user S3 L. The scale on the figure indicates the values in $mV/\mu m^2$.

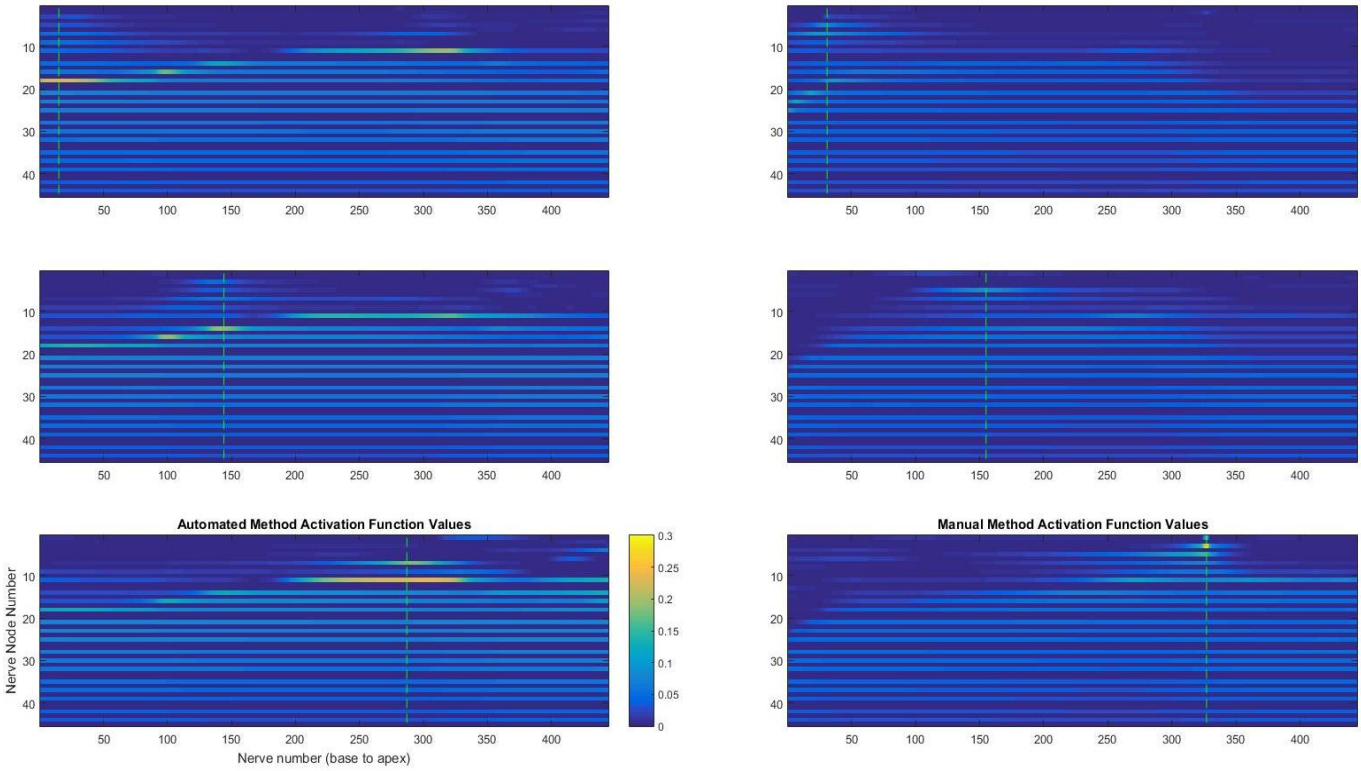

Figure 4.20 - Simulated activating function distribution across the nerve fibres as a result of electrical stimulation by electrode e1 (top), e11 (middle) and e22 (bottom). These results are shown for both the automated (left) and manual (right) methods. The results were obtained from the model created for user S3 R. The scale on the figure indicates the values in $mV/\mu m^2$.

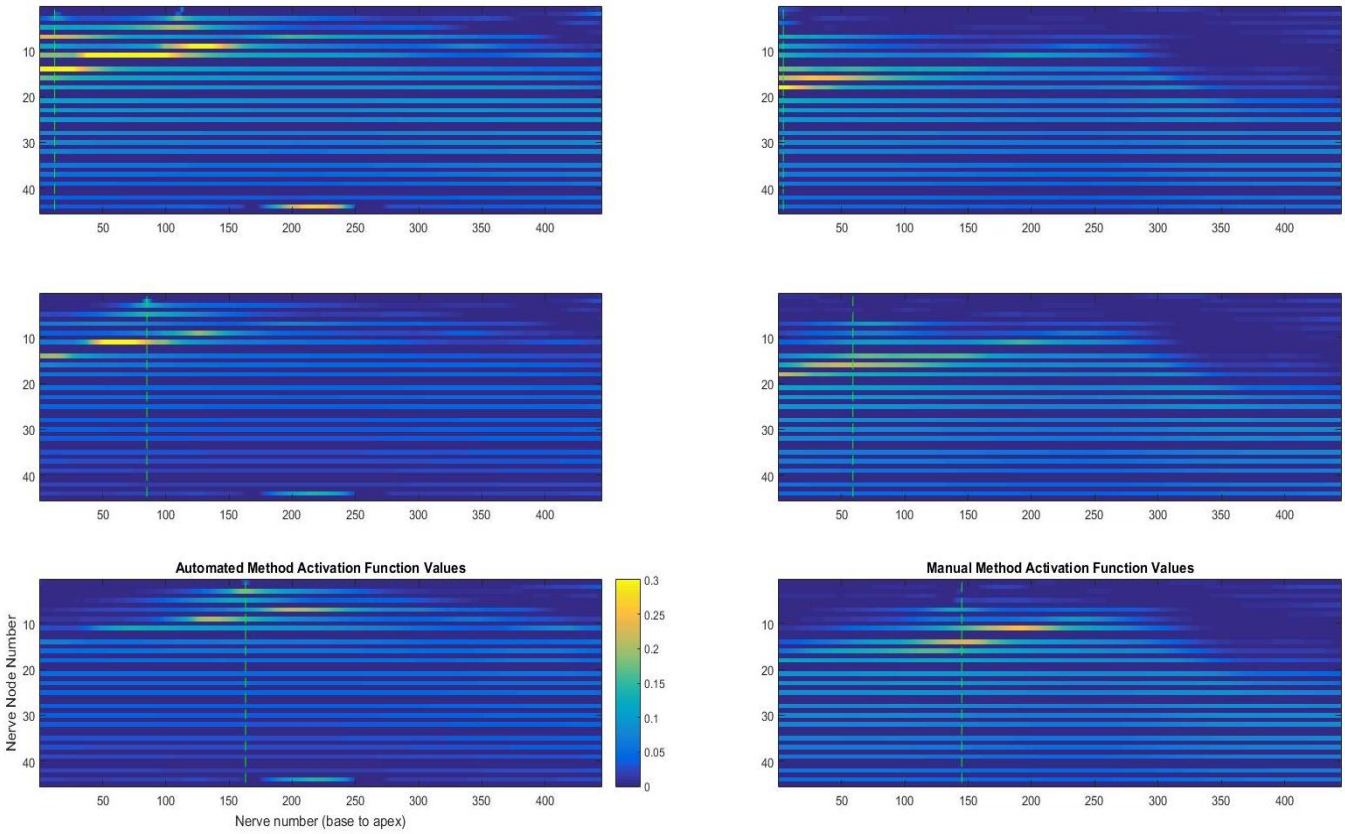

Figure 4.21 - Simulated activating function distribution across the nerve fibres as a result of electrical stimulation by electrode e1 (top), e4 (middle) and e7 (bottom). These results are shown for both the automated (left) and manual (right) methods. The results were obtained from the model created for user S30 L. The scale on the figure indicates the values in $mV/\mu m^2$.

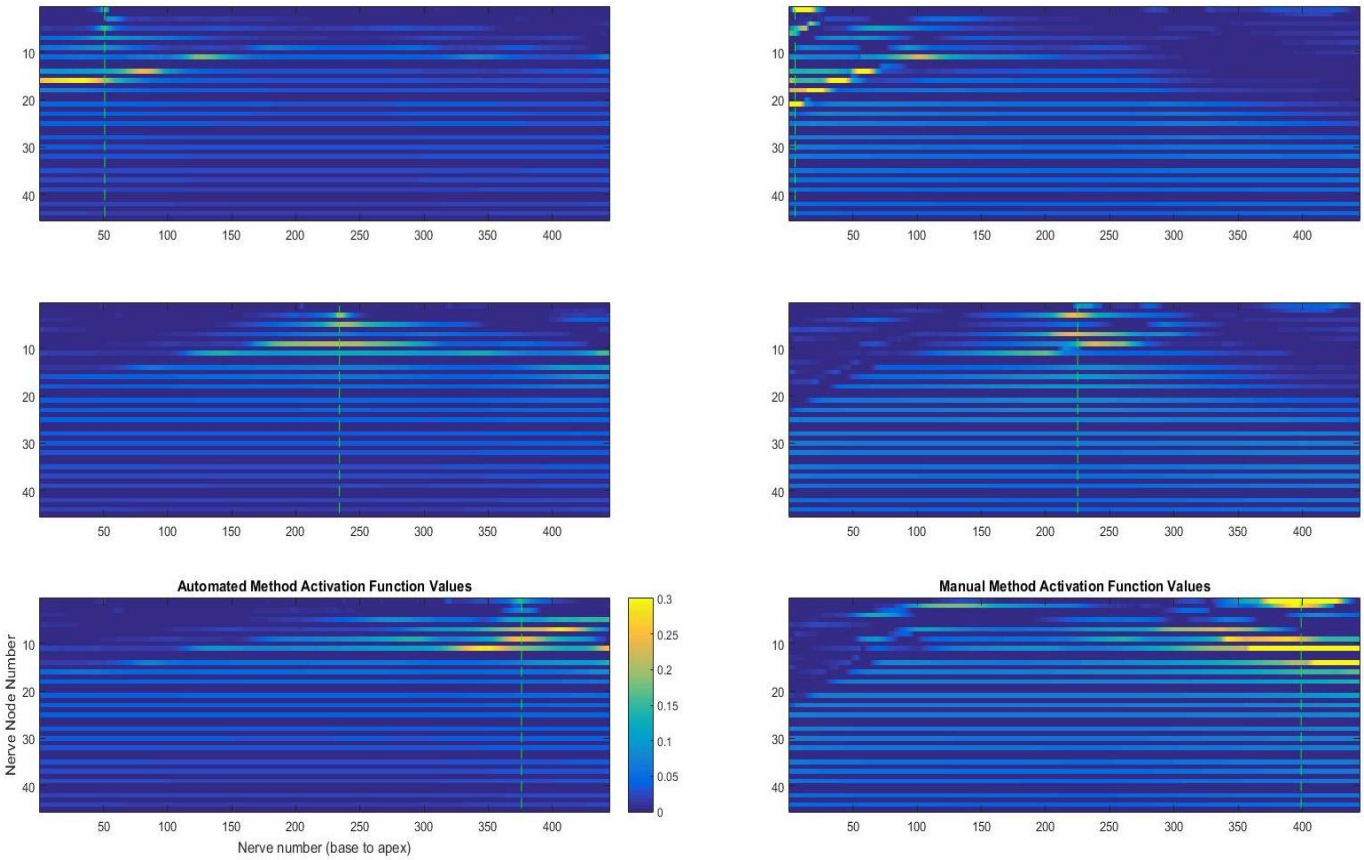

Figure 4.22 - Simulated activating function distribution across the nerve fibres as a result of electrical stimulation by electrode e1 (top), e6 (middle) and e12 (bottom). These results are shown for both the automated (left) and manual (right) methods. The results were obtained from the model created for user S30 R. The scale on the figure indicates the values in $mV/\mu m^2$.

Common similarities between results include the close proximity of neural excitement to the stimulating electrode as well as higher activating function values in the dendrite region of the models. For all models of user S3 and S13, the activating function values for the automated method models are higher than the manual method model values in the dendrite region with similar values closer to the axon. The higher values seen only in these regions indicate a more abrupt change in nerve fibre electric potential, which may indicate that under similar stimulation conditions the automated method models show increased predicted neural excitement when compared to their manual method model counterparts. The vertical dashed green lines on **Figure 4.17** to **Figure 4.22** indicate the nerve fibre with the largest number of stimulated compartments and the highest activating function values

along the length of the nerve fibre. For each of the models under every stimulation condition, the position of this nerve number (the vertical dashed green line in **Figure 4.17** to **Figure 4.22**) was extracted and is indicated in **Figure 4.23**.

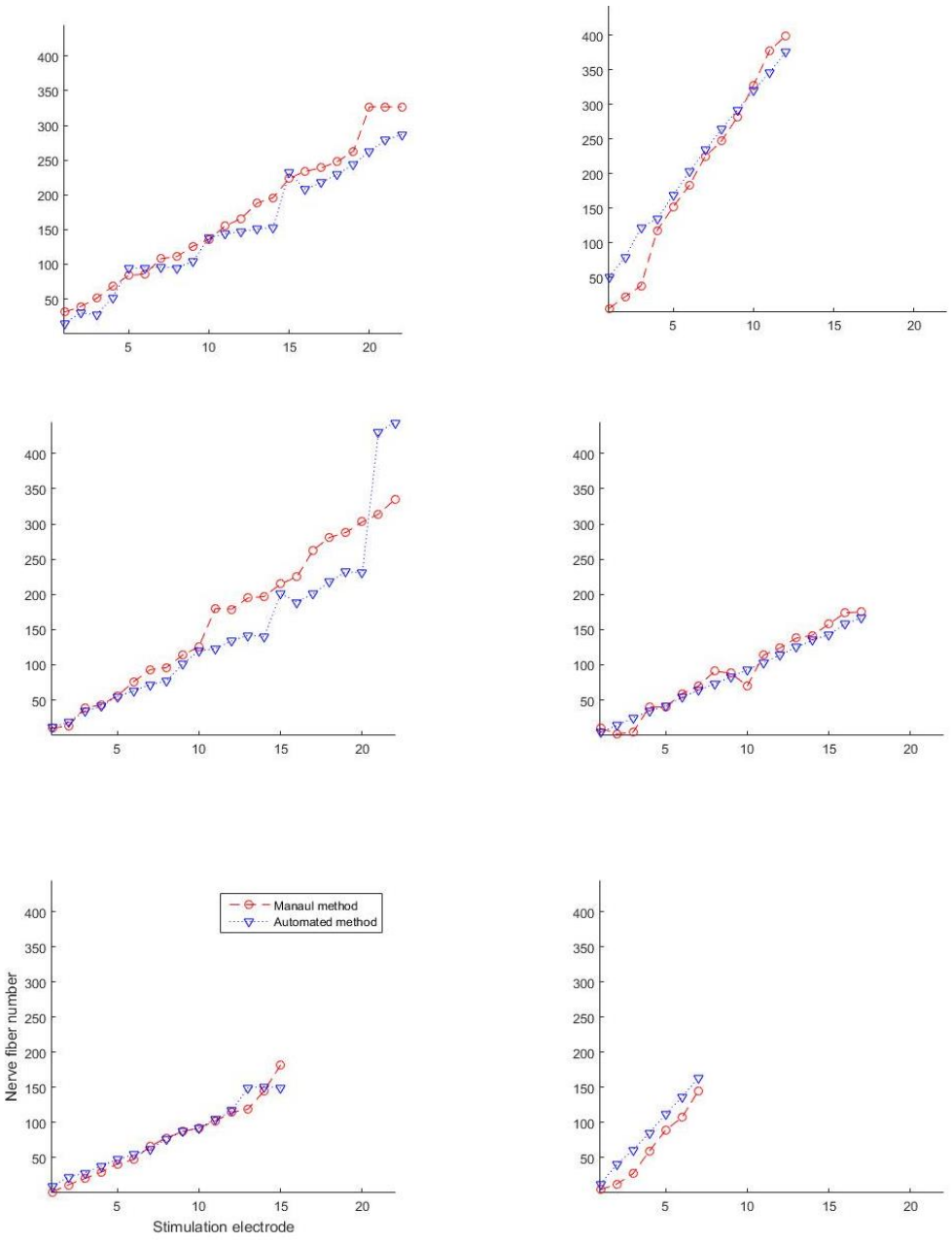

Figure 4.23 - The nerve fibre number with the largest number of stimulated compartments and the highest activating function values for each model, user S3 R (top left), user S30 R (top right), user S13 L (middle left), user S13 R (middle right), user S3 L (bottom left) and user S30 L (bottom right).

The values depicted in both **Figure 4.23** and **Figure 4.16** can be equated to an overall similarity percentage of 64.18%, and a correlation percentage of 94.88% ($p<0.001$) between the automated and manual method. The potential distribution values and the activating function values are generally higher when using the automated method as opposed to the manual method as a result of the smaller volumes of the automated cochlea models. These values give an initial indication that the use of all three measured landmark spirals to create the 3D cochlear model does have a significant effect on the predicted model potential distribution as well as the neural excitement. Further research is needed to establish whether or not this effect is beneficial with the use of a more detailed neural model to determine which of the model predictions are more comparable to physically measured data.

4.6 SUMMARY

This section gave a summarised overview of the results obtained through the various models that were applied. The methods showed a high accuracy in the initial detection of the cochlea, which included the detection of the apical point and the nerve width narrowing. The landmark detection showed a marked similarity between the results obtained through purely manual methods and the automated method presented in this study. The geometries constructed from these landmarks showed the overall 3D volumes of the generated cochlea models to be smaller than the manually created 3D cochlea models. The electric potential distribution of the automated method models showed a higher and more pronounced distribution pattern than the manually created models under similar stimulation conditions. The nerve fibres at which the highest electric potential is measured also showed similarities and when evaluating the nerve fibre excitement as a result of electric stimulation, the automatic method models presented a higher level neural activity compared to the manually created models under similar stimulation conditions. The final discussion of all the results is given in the following chapter.

CHAPTER 5 DISCUSSION

5.1 CHAPTER OBJECTIVES

This study created a method that aimed to generate 3D cochlear models by means of applying automation techniques. The results presented in the previous chapter are further discussed, and the findings of this study are presented in this chapter.

5.2 DISCUSSION OF RESEARCH QUESTIONS

5.2.1 Is it possible to automate the model development workflow?

The study showed that when isolating the various steps involved in the model development workflow, full automation is achievable with the following steps:

- Initial detection of the cochlea, which involves detection of the apical point and the nerve width narrowing.
- Detection of the electrode array spiral trajectory.
- Data processing to create smooth data sets by automatically identifying and removing outlier values.
- Data interpolation and extrapolation to fill interval data voids for which no landmarks were detected on CT images.
- Rotation of the extracted cochlear data to an upright and vertical centreline.
- Data fusion to fit higher detail template data to the extracted landmark trajectory spirals.
- Recreation of electrode array geometric framework using an extracted electrode array spiral.

- Search, detection and correction of cochlear spiral multi-level interference, such as overlapping of basal and apical boundaries.
- Detection and correction of electrode protrusion of the cochlear wall.
- Construction of individual internal structures of the cochlea and assembly of the structures to create the cochlea model.
- Reconstruction of the electrode array in 3D and inclusion of array into cochlear model.
- Export of user-specific cochlear model in a format compatible with finite element software for electric volume conduction simulations.

Manual intervention is required in the following workflow stages:

- The creation of the knowledge database, known as the reference data, is a manual step performed only once in this study. The process involves the manual measurement of the relevant landmarks and geometrical data of 15 separate cochleae.
- A calibration procedure is required at the onset of the automated method in order to align the reference data centreline to the user data captured on the CT image.

5.2.2 Is data fusion required to define smaller anatomical structures?

In this study, data fusion was used to define a higher level of detail in the models. As the smaller, internal cochlear structures are not always visible on CT scans, the only information that was consistently possible to extract was the landmark spirals located on the cochlear walls. These landmark points were then used to mould a template model containing smaller cochlear structures not visible on CT images to the macro structure of a specific user's cochlea. The cochlear template boundary was altered in such a way to match the extracted landmark spirals and by doing so, the geometrical dimensions of the internal structures of the template were also adapted to fit the new macro structure.

5.2.3 Can an automated model provide similar type of results to manually created models?

5.2.3.1 Initial detection of the cochlea

The average percentage of the total number of scans on which the cochlea was detected, was 95.87%, which equates to 172 CT scan images of the 180 images per CI user. In comparison to the total number of CT scans per user, the number of scans on which the cochlea is detected remains high, indicating the level of error (incorrect detection of the cochlear landmark positions) to be small.

5.2.3.2 Comparison between automated and manual landmark measurement data

The averaged NRMSE value across all the models between the two methods was 0.1566, indicating a similarity percentage between the two methods of 84.34% across all six models. The automated method showed an 89.71% correlation to the predicted trends obtained with the manual method. The significant differences seen in the measurements can be attributed to two main causalities. The first cause of measurement deviations is attributed to the search field location for boundary points in an area for which no boundary points are detected. In such cases, the values were determined through interpolation. When interpolating across data regions, intricate details, such as turning points, could be present in such regions which are not always captured through interpolation. This leads to larger deviations in such sections.

An alternative reason for the deviations is the wrongful location of the search field. When searching for boundary points in regions outside the cochlea, the algorithm could detect boundary points not associated with the boundaries of the cochlea and wrongfully add these points to the field of valid points. The measurements on **Figure 5.1** depict an example of one of the significant differences discussed for the lateral spiral measurements for the right ear cochlea of User S30. The automated method detected a greater majority of boundary points on the outside of the actual cochlea boundary wall and considered these points as valid.

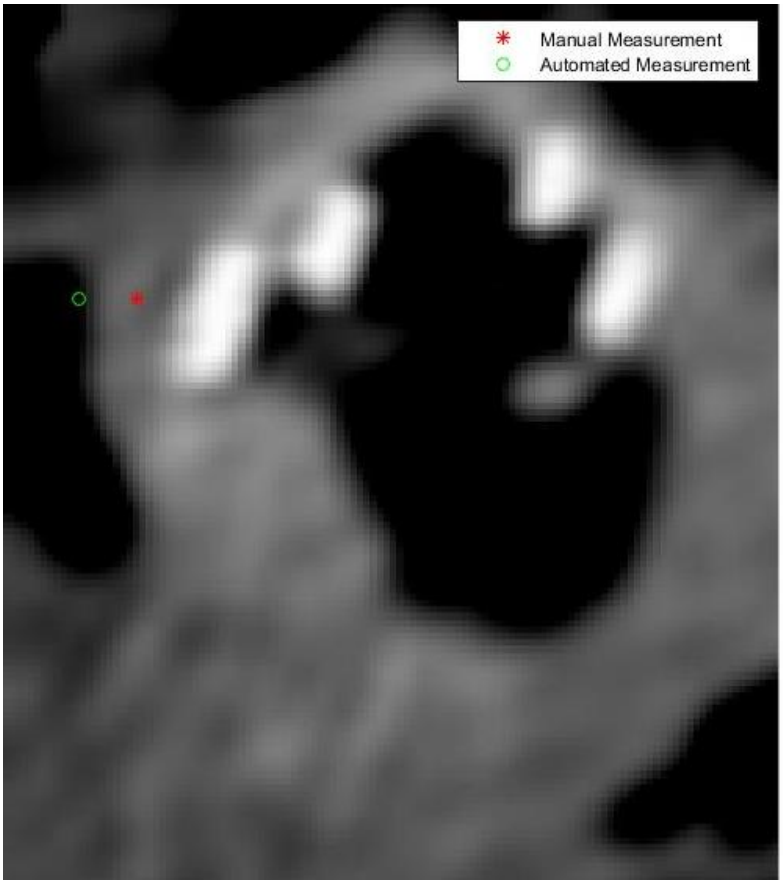

Figure 5.1 – Measurement comparison between the manual and automated methods for one landmark point of the lateral spiral of the right ear cochlea of the User S30.

The difference in electrode array detection of the right ear cochlea of User S3 was seen as a result of the manual measurements detecting the coordinates of the electrode array outside the cochlea. On the same slide, the automated method could not identify the electrode artefact, i.e. the electrode location, since the colour intensity value was lower than the identification threshold. The electrode location was only identified after a few more slides where it was located inside the cochlea.

It is clearly seen that a small variation in pixels on a CT scan relates to a much larger dimensional difference in the model itself. A difference in measurements of one pixel for the case presented in **Figure 5.1**, is equivalent to approximately 0.1 mm due to the low resolution of the images. A value of 0.1 mm variation per pixel is considered to be a large

change in dimensional value when working with very small anatomical structures such as the cochlea. The largest difference between the manual and automated measurements was equivalent to 0.88mm, located at 409 degrees of the left ear cochlea of User S13, which translates to approximately 9.7% of the average 9 mm total width of the cochlea. By converting this value back to a difference in pixel format, this is equivalent to a change of only 9 pixels. This indicates that even the small change in pixel selection could relate to a high dimensional difference, as viewed in all models used in this study. It is therefore evident that the translation of landmarks to model dimensions is very sensitive to the exact placement of landmark points on a CT scan, whether by the manual or automated method. This sensitivity is amplified by the low resolution of the CT scans that result in poor visibility of landmarks and residual artefacts that may distort or mask the location of landmark points.

5.2.3.3 Cochlea model geometry comparison

The models developed with the manual and automated methods differed in terms of visual appearance, as the automated models have much smaller cross-sectional face sizes compared to the manual method models. This difference is caused by the different procedures by which each of the methods generate a model. The manual method relies on the use of only one spiral, the lateral spiral, to determine a best fitting template from an array of templates, which is then further adjusted to more closely fit to the measured spiral. Although such a method adds user-specific traits to a model, the basis for such a model mainly relies on only one characteristic landmark. The outer shape of the cochlea thus relies on the lateral spiral only, and the template to which it shows the closest resemblance. The automated method approaches the model generation procedure from a different point of view as the measurement of the lateral, upper and lower spirals add two additional landmark spiral data sets that are specific to each cochlea measured. The use of all three spirals to adapt a template cochlea to match the measured spiral data for each cross-section, ensures that the cochlea's outer wall morphology can be determined with a greater level of user-specificity. The use of the three measured landmark spirals allows additional characteristics, such as the trajectory of more apical ducts, to be taken into account. Information such as this is difficult to estimate from only the lateral spiral profile. In short,

the use of three landmark spirals, rather than one, to develop a cochlear model adds an additional level of detail and user-specificity to the 3D model.

5.2.3.4 Electrode array geometry comparison

The electrode geometries were similar in terms of the carrier diameters in the apical and basal regions in addition to the change in electrode size along the length of the electrode carrier. The only models that showed a significant difference in carrier diameters were seen in the models created for the left and right ear cochleae of the User S13. The carrier dimensions for the manually created models remained constant along the length of the electrode, whilst the automated model increased in radius from the apical electrode region to the basal region, as indicated on the electrode dimensional data sheet (Cochlear.com, 2016). The majority of geometrical differences were seen in terms of the spacing between electrodes and the electrode contact widths. These differences could have occurred as a result of different interpretations of the electrode array data sheet as the spacing between electrode contact points are difficult to interpret from the data sheet. The diameters of the carrier at the base and the apex are specifically given on the data sheet and therefore, the carrier diameter values across the models are much more consistent between the models.

The reasons for differences in the predicted electrode pathways among the two methods are twofold, and once again caused by the different approaches followed in the two model development methods. The first cause of such differences is the difference between the two methods when recreating the electrode. After adjusting the best fitting template according to the lateral spiral, the manual method recreates the electrode spiral based on the position of the electrode position relative to the lateral spiral position. The automated method also recreates the cochlea pathway in the adjusted template in a similar fashion, but by taking into account the electrode position relative to all three measured landmark spirals, thus taking into account the upper, lower and lateral regions of the cochlear wall boundaries. The second reason for the observed differences is caused by how each method adjusts the electrode position. Once the model is generated, the manual method will, in some cases, manually adjust the electrode spiral positions to remove electrode intersections with other cochlear geometries as far as possible (Malherbe et al., 2013, Malherbe et al., 2015), thus minimising apparent insertion trauma which most likely is not present. The

automated method however, does not aim to specifically add or remove any trauma (i.e. overlap of the electrode array with cochlear structures) as a result of electrode array insertion. Although research has indicated that trauma can be caused during electrode insertion (Nadol J.B et al., 2001, Finley et al., 2008, Verbist et al., 2009), evidence of such trauma cannot be established from CT scan images alone, since these images have poor visibility. The addition of such trauma is an added level of user-specific detail that could lead to a variation in results, although the ability to determine insertion trauma bears further investigation.

5.2.3.5 Electrode array angular length differences

Amongst the differences in the electrode array, the most apparent difference is seen in the angular length difference between automated and the manual measurement methods. The reason for such differences may once again be attributed to the difference between approaches followed between the manual and automation model generation methods. The automated method relies on the detection of the electrode array by tracking the centre of a specific range of highest colour intensity values, caused by an electrode artefact, to determine the electrode pathway. The manual measurement relies on the visibility of the small area of artefact created by the electrode. The centre of this region is then determined by inspection, and is continuously selected until such an artefact region is not present, resulting in the end of the electrode array. Beyond this end of the highest electrode artefact, an artefact region can still be seen, which to the naked eye, looks very similar to the previous artefact regions, although this colour intensity decreases to below the intensity-based threshold. Any increase in the intensity-based threshold limit range results in too much residual artefact surrounding the cochlea for it to be detected. The centrepoint of the electrode array is difficult to determine with the naked eye, especially in a large cluster of electrode artefact. By dividing such a large cluster of artefact into intensity-based values, the centrepoint of the electrode contact is more distinguishable; not only from an automated method point of view, but also from a manual measurement perspective.

5.2.3.6 Model-based potential distribution

Once the user-specific 3D model is created in COMSOL, that model is used to simulate and predict the electric potential distribution within the cochlea when stimulated by an electrode. The electric potentials predicted by the finite element models were the higher at closer regions to the stimulating electrode for all models and under all simulated conditions. The electric potential values then decreased as distance from point of simulation increased, i.e. the stimulating electrode. The model outputs were used only for comparison in this study; therefore, the models were simplified to reduce computational calculation time by using a sphere as the surrounding bone material of the cochlea. The outer boundaries of the sphere acted as electrical ground. The potential at the electrical ground is equal to 0V whilst closer to the stimulation electrode, a higher potential is predicted as a result of the electric field created between these two regions. As a result, the points of measurement closest to the stimulating electrode will be at a higher potential value. These points of measurement on the nerve fibres that are closest to the stimulating electrode are dependent on (i) the electrode type itself as well as (ii) the location of the electrode. In this study, these points were found to be located closer to the dendrite region of nerve fibres, as can be seen from the results.

In four of the six models, the overall predicted potential values of the automated models were noticeably higher than those for the manual method, whilst the manual method model of user S30 predicted higher or similar potential distribution values compared to the manual method models. The higher potentials predicted by the automated models can be attributed to the difference in the cochlea volumes of the the manual and automated models. When creating the cochlear models, the upper, lower and lateral spirals are taken into account to determine the location of the cochlear walls as opposed to only the lateral spiral. This leads to a smaller overall cochlear model volume. The smaller cochlear volume results in an overall lower conductivity, i.e. higher predicted potential values under constant current conditions. The higher potentials predicted by the manual method models of user S30 can be attributed to the nerve fibre volumes being similar to, or smaller than that of the automated method nerve fibre volumes as well as the electrode contact modelling and simulation method applied.

The difference between the automated and manual methods for the nerve number at which the maximum electric potential is located, is caused by the difference in geometric measurements of the electrode array. As indicated earlier, electrode contact face widths, the carrier widths between contact points, and the varying insertion depths of the electrode arrays for the various models all play a role in the stimulation region at which maximum potentials are observed. This difference, combined with the accumulated differences in the electrode geometry measurements, lead to more apically-located regions of nerve fibres in the cochlea being stimulated.

5.2.3.7 Activation function predictions

To provide a rudimentary interpretation of the neural activity that is most likely to be predicted by each model for various stimulation parameters, the nerve fibre activating function (Rattay, 1989) was used.

The automated models predicted overall higher activating function profiles when compared to those predicted by the manual models. These higher activating function values can be attributed to the lower cochlea volumes produced by the automated method.
As the activating function is directly proportional not only to the potential values themselves, but to the difference between the electric potentials along the length of each nerve fibre, the overall higher electric potential, coupled with a more abrupt change in potentials in the automated results, lead to higher activating function values.

It has been specified that the activating function values give an indication of the probability of excitation on nerve fibres, and it was evident that the nerve fibres with the highest probability of excitation were generally located closest to the stimulating electrode. The larger the activating function values are at a point on a nerve fibre, the larger the level of excitement at that specific point is. The results of the higher activating function values of the automated model indicate that under the same stimulation conditions, the automated models predict a higher probability of excitation in similar nerve fibre regions than the manual model predictions. This also means that a lower stimulation applied to the automated model can yield similar activating function values than those perceived in

manual models. The automated method could therefore, potentially produce cochlea models with lower auditory nerve fibre excitation threshold values than their respective manual method counterparts. To further investigate the validity of the automated model predictions, a normalised model was created for user S13 L by increasing the model volume to a volume closer to that of the manual method model, by using the method discussed in section 5.2.3.8.

5.2.3.8 Normalised model predictions

An additional model was created to further investigate and verify the model predictions by using an adapted version of the automated method to recreate the cochlea model of user S13 L based on the same model development method followed by Malherbe et al. (2015), i.e. using only the lateral spiral as a point of reference to adjust the template data; this additional model is referred to as the normalised model from this point forward. The electrode array was also recreated using only the lateral spiral. By doing so, the normalised model volume increased from 76.98 mm^3 to 129.1 mm^3, which predicted the potential distributions and activating function values as indicated in **Figure 5.2** and **Figure 5.3**, respectively.

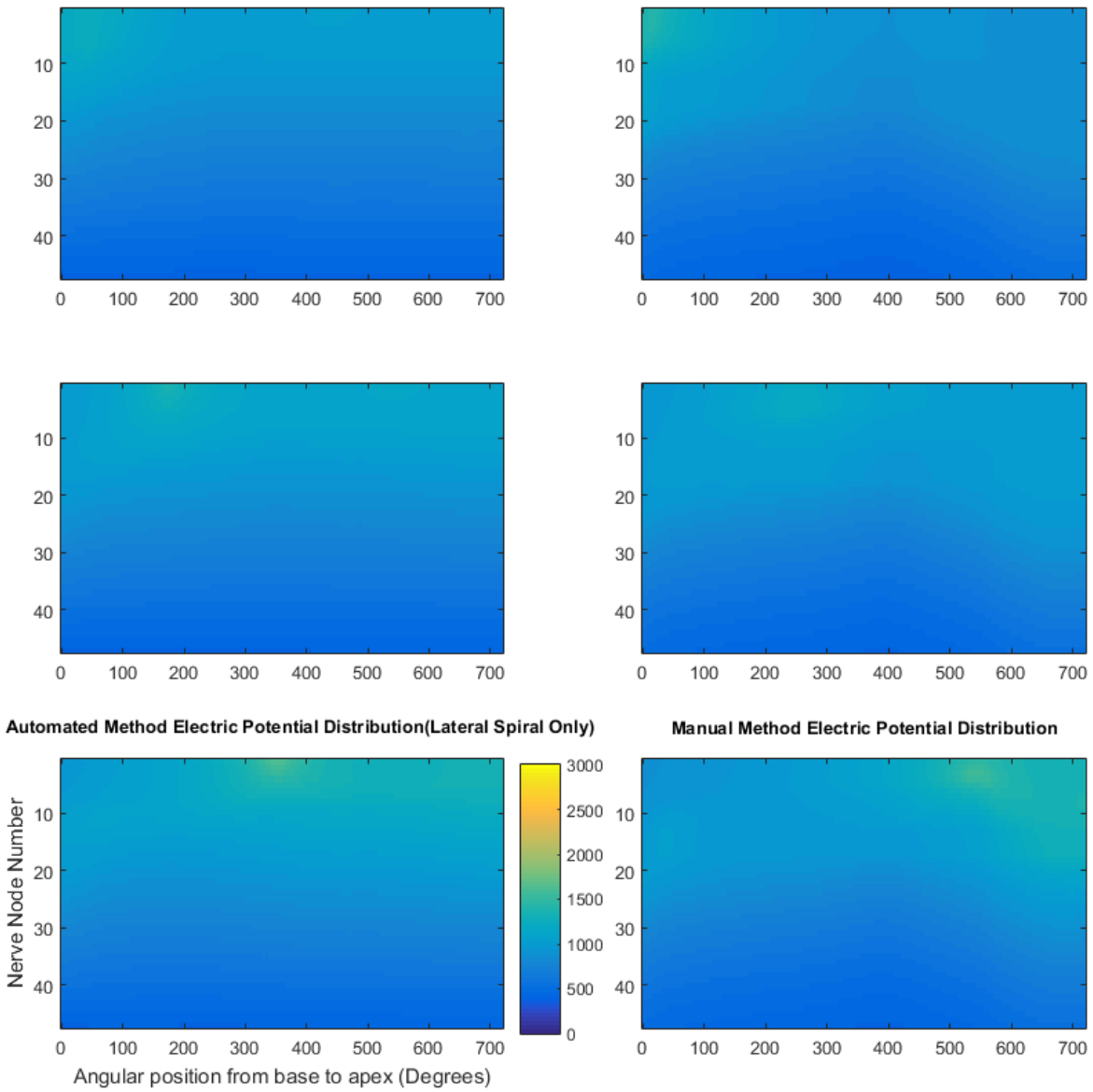

Figure 5.2 - Simulated activating function distribution across the nerve fibres as a result of electrical stimulation by electrode e1 (top), e11 (middle) and e22 (bottom). These results are shown for both the automated (lateral only) (indicated on the left) and manual (indicated on the right) methods. The results were obtained from the model created for user S13 L. The scale on the figure indicates the values in mV/µm2.

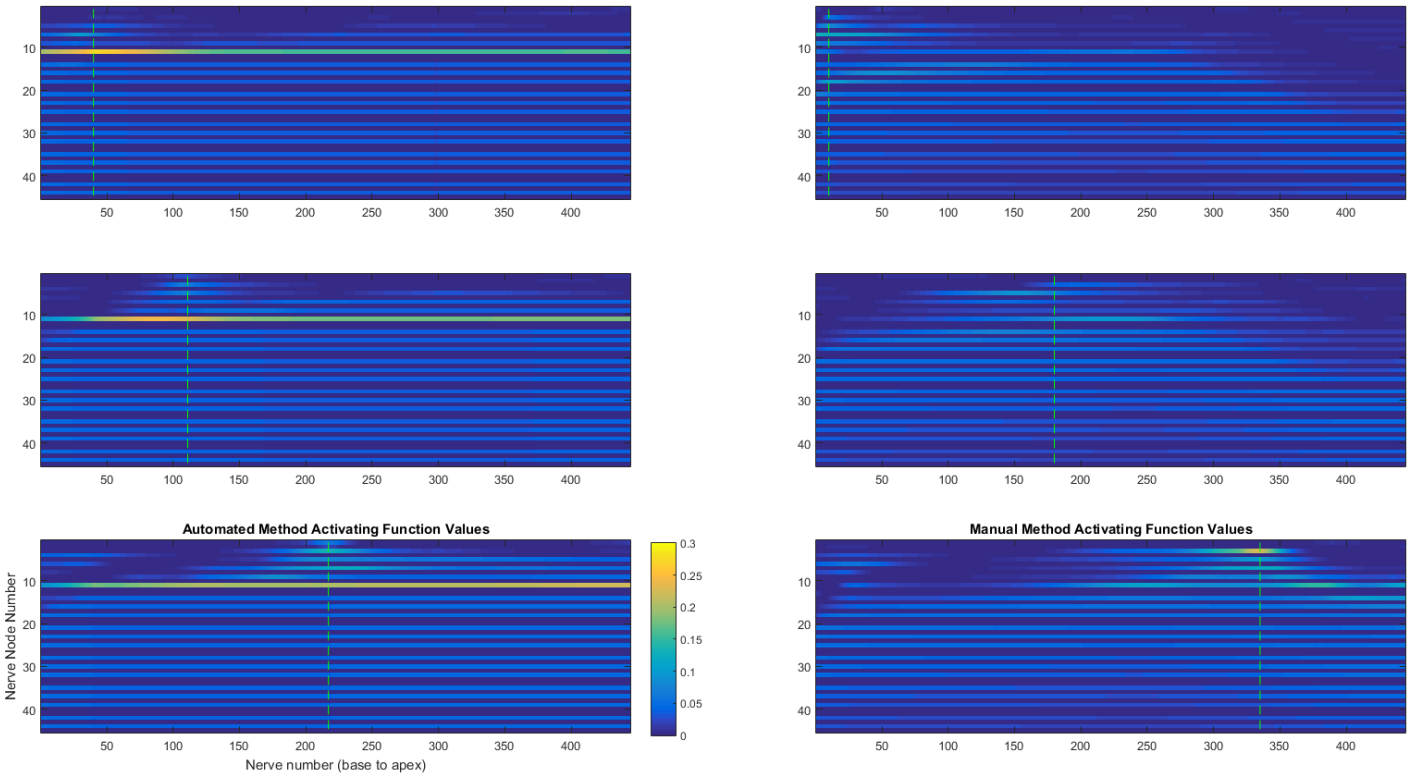

Figure 5.3 - Simulated activating function distribution across the nerve fibres as a result of electrical stimulation by electrode e1 (top), e7 (middle) and e15 (bottom). These results are shown for both the automated (lateral spiral only) (indicated on the left) and manual (indicated on the right) methods. The results were obtained from the model created for user S13 L. The scale on the figure indicates the values in $mV/\mu m^{2.}$

The normalised model produced a clear reduction in potential distribution values that were similar to the predicted potentials of the manual method. This normalised model showed similarities in results and activating function values, although the manual method predicted a higher probability of stimulation at more apically-located nerve fibres as seen in **Figure 5.4**. This result may be attributed to the fact that only the lateral spiral was used as a reference point to recreate the electrode array.

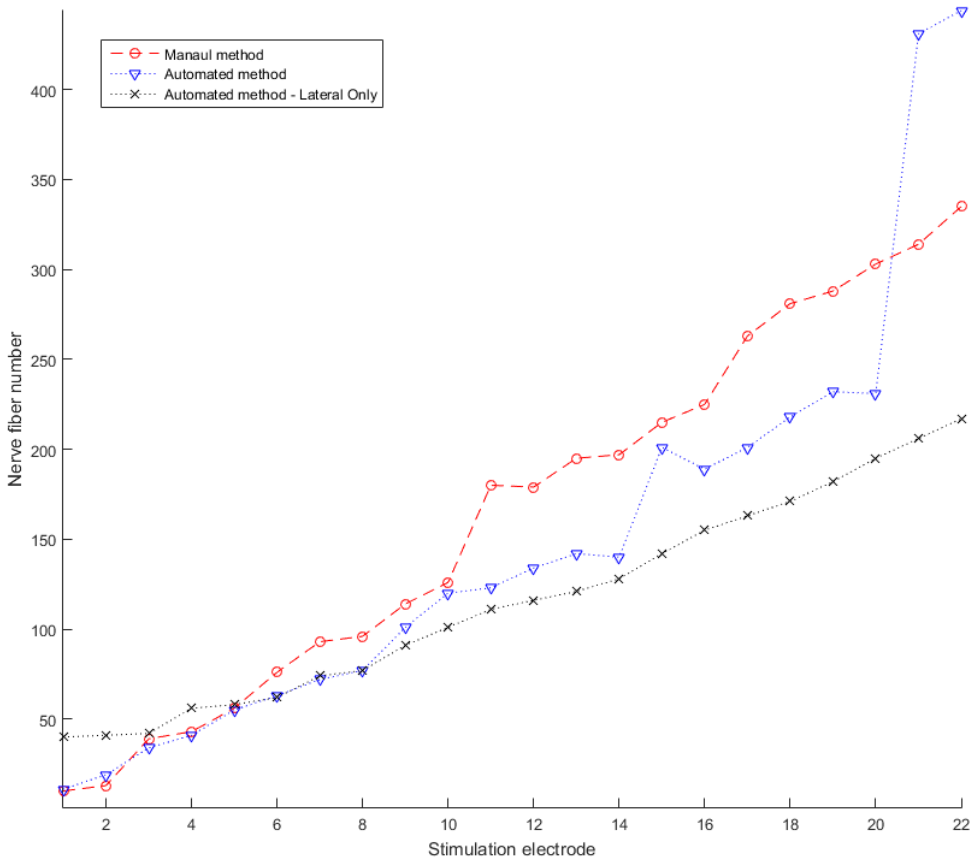

Figure 5.4 - The nerve fibre numbers with the largest number of stimulated compartments and the highest activation function values for each model.

Moreover, **Figure 5.4** indicates that the predicted regions of stimulation of the automated method, using the upper, lower and lateral reference points, showed a closer similarity to the manual method than the predicted regions of stimulation of the normalised model. The simulation predictions indicate that the inclusion of the upper, lateral and lower spiral, as well as the position of the electrode relative to all three spirals, tend to show a greater similarity to the manual measurements. The exclusion of the upper and lower spirals during model generation shows a noticeable deviation from the manual method model predictions. These results indicate that not only does the automated method predict similar regions of stimulation to that of the manual method, but it also predicts higher activating function values under similar stimulation conditions by including the upper, lateral and lower spiral points as applied in this study.

5.3 COMPARISON WITH LITERATURE

Despite the dimensional sensitivity of the landmark selection on CT scans, the average normalised root mean squared error (NRMSE) value across all the models presented in this study was 0.1566, indicating a similarity percentage of 84.34% between the two methods across all six models. Similar studies into automated measurement techniques, such as the method developed by Noble et al.(2011), indicate an average similarity percentage of 75% between the automated and manual measurements. Other studies have reported a successful detection rate (SDR) of 73.7% (Sari et al., 2015) and 64,67% (Gupta et al., 2015) of landmarks within a 2 mm accuracy window. For accuracy windows of 3 mm, the SDR increased to 86.8% (Sari et al., 2015) and 82.67 % (Gupta et al., 2015). The similarity of the measurements of the method developed in this study was found to be in close comparison to the similarities found in literature.

The average correlation percentage between the manual and automated methods in this study was found to be 89.58%, indicating a close similarity in the data trend between the automated and manual method measurements; i.e. how the data spiral point coordinates change along the length of the cochlea. This value was found to be comparable to similar automated model development strategies found in literature, with reported correlation values of 65.3% (Aneja et al., 2015) and 89% (Shahidi et al., 2014).

The mean error between the measured landmark spirals of the automated and the manual methods for the study at hand, is equal to 0.3953mm. This mean error level is below similar automated model development studies of 2.04 mm (Sari et al., 2015), 2.01 mm (Gupta et al., 2015) and 3.86 mm (Shahidi et al., 2014). The mean error in this study is more comparable to the studies of Reda et al. (2013) and Noble et al. (2011) with mean error values of 0.657 mm and below 0.80 mm, respectively.

The automated method developed and presented in this study showed comparable results to results obtained from other literature, and it is concluded that the method is valid and can be used to develop a 3D computational model of an electrically stimulated cochlea through automated and semi-automated techniques.

5.4 FUTURE WORK

The study presented a valid, semi-automated method for model development and based on this, the following areas were identified for future work.

5.4.1 Apply automation algorithm to higher resolution images

The current study presented a model development algorithm that is able to predict results comparable to similar method results found in literature. These results were however, obtained by applying the method to low resolution CT scan images. The application of the method to higher resolution images was not investigated, and the use of common imagery techniques of higher resolution, such as Cone Beam Computed Tomography (CBCT) images, could provide improved accuracy in landmark detection.

5.4.2 Automated calibration of reference data

The automated method presented in this study aimed to automate the model development process without compromising the validity and accuracy of the data. This was achieved through the use the KBLDA, which required an initial manual calibration procedure. Through further investigation into the automation of this procedure, a fully automated model development strategy can be created. By doing so, the time spent on developing the model can be decreased.

5.4.3 Insertion trauma detection and inclusion

Electrode insertion trauma, when present, is a user-specific trait unique to each CI user. Although each surgeon aims to minimise insertion trauma as far as possible, such trauma may still be present and as a result of the poor visibility of CT scan images, it is near impossible to detect such trauma. Both the detection and inclusion of insertion trauma in the development of 3D models require further investigation as this could impact the model predictions.

5.4.4 Improved internal structure adaption during template fitting

The automated model development algorithm presented in this study makes use of the detected landmarks to fit a cochlea template to the measured values. This procedure scales and rotates the template according to the three measured landmarks, thereby maintaining the relationship of the internal structures relative to the measured landmarks. In addition, the relationships between the internal structures of the cochlea template are also maintained and unaltered during template adaption. Further investigation is required on the relationship between the measured landmark points, and possible additional landmarks, and how these landmarks can be used to predict the size and shape of the each of the independent internal structures.

5.4.5 Validate predicted neural excitement through inclusion of more detailed and sophisticated neural model.

The current study included the use of the activating function as a basic interpretation of the neural excitement as a result of monopolar stimulation. This was used for comparison between the automated and manual models as an initial estimate of neural excitement. This method however, only gives an initial estimate of neural excitation and does not necessarily reflect predictions by a more sophisticated neural model. In order to further validate the prediction of the automated model, additional investigation is required to determine whether the differences seen between the automated and manual models tend to converge more towards real life data.

CHAPTER 6 CONCLUSION

The following conclusions were drawn from the study.

- The study presented a method that is able to automatically find, extract, refine and construct 3D models of cochleae and cochlear implants based on landmark detection. Manual intervention was only required during the initial calibration procedure as a result of the variations present in different cochleae as well as the selection of the type of electrode array.
- The combined time to generate a model was approximately 7 minutes, which is significantly less than the time required by manual methods (which could take weeks to complete measurements).
- When compared to manual measurements, the overall performance of the method presented in the study was 84.28% in landmark detection capability, and a very similar data trend given by a correlation percentage of 89.29% when compared to manual measurements. Similar studies in automated measurement techniques, such as the method developed by Noble et al. (2011), indicate a similarity percentage average of 75% between the automated and manual measurements. The similarity in measurements for the method developed in this study indicates a higher overall similarity.
- The models created with the automated method indicated that by including all three measured landmark spirals as opposed to only the lateral spiral to construct 3D cochlea models, a significant effect is seen on not only the model geometry, but also the results obtained from such models. The cochlear volume of the automated models was smaller, which resulted in lower electrical conductivity. The lower conductivity resulted in a higher resistance, which in turn caused higher electric potential values under constant current conditions. The higher and more

abrupt changes in electric potential along the length of the nerve fibres also indicated that the automated models showed greater nerve fibre excitement than the manual methods did under the same stimulation conditions. In four of the six models, the overall predicted potential distribution values were higher for the automated method compared to the manual method models. The remaining two models showed a similar potential distribution and activating function values. The study determined that the inclusion of all three measured landmark spirals does have a significant effect on model predictions, although further investigation is required to determine whether such significant influences are beneficial to the accuracy of the predictions made using 3D computational cochlea models.

REFERENCES

AGRAWAL, V. & NEWBOLD, C. 2012. Computer modelling of the cochlea and the cochlear implant: A review. *Cochlear Implants International,* 13**,** 113-123.

ANEJA, D., VORA, S. R., CAMCI, E. D., SHAPIRO, L. G. & COX, T. C. Automated detection of 3D landmarks for the elimination of non-biological variation in geometric morphometric analyses. Proceedings - IEEE Symposium on Computer-Based Medical Systems, 2015. 78-83.

BELLOS, C., RIGAS, G., SPIRIDON, I. F., BIBAS, A., ILIOPOULOU, D., BÖHNKE, F., KOUTSOURIS, D. & FOTIADIS, D. I. 2014. Reconstruction of Cochlea Based on Micro-CT and Histological Images of the Human Inner Ear. *BioMed Research International,* 2014.

BRAITHWAITE, B., KJER, H. M., FAGERTUN, J., BALLESTER, M. A. G., DHANASINGH, A., MISTRIK, P., GERBER, N. & PAULSEN, R. R. Cochlear implant electrode localization in post-operative CT using a spherical measure. Proceedings - International Symposium on Biomedical Imaging, 2016. 1329-1333.

COCHLEAR.COM. 2016. *Cochlear™ Implant Electrode Comparison* [Online]. Available: http://www.cochlear.com/wps/wcm/connect/b29815ab-da8c-453c-a8f4-2041e6088459/FUN1142_ISS4_JUL12_Electrode_Comparison4.pdf?MOD=AJPERES&CACHEID=ROOTWORKSPACE-b29815ab-da8c-453c-a8f4-2041e6088459-lhTpEH8 [Accessed 2016-10-08 2016].

ERIXON, E., HÖGSTORP, H., WADIN, K. & RASK-ANDERSEN, H. 2009. Variational anatomy of the human cochlea: Implications for cochlear implantation. *Otology and Neurotology,* 30**,** 14-22.

FINLEY, C. C., HOLDEN, T. A., HOLDEN, L. K., WHITING, B. R., CHOLE, R. A., NEELY, G. J., HULLAR, T. E. & SKINNER, M. W. 2008. Role of electrode placement as a contributor to variability in cochlear implant outcomes. *Otology and Neurotology,* 29**,** 920-928.

FOWLER, D. R., MEINHARDT, H. & PRUSINKIEWICZ, P. 1992. Modeling seashells. *Computer Graphics (ACM),* 26**,** 379-387.

FRIJNS, J. H. M., DE SNOO, S. L. & SCHOONHOVEN, R. 1995. Potential distributions and neural excitation patterns in a rotationally symmetric model of the electrically stimulated cochlea. *Hearing Research,* 87**,** 170-186.

GIBSON, D., GLUTH, M. B., WHYTE, A. & ATLAS, M. D. 2012. Rotation of the osseous spiral lamina from the hook region along the basal turn of the cochlea: Results of a magnetic resonance image anatomical study using high-resolution DRIVE sequences. *Surgical and Radiologic Anatomy,* 34**,** 781-785.

GIRZON, G. & EDDINGTON, D. K. THREE DIMENSIONAL, ELECTRO-ANATOMICAL MODEL OF THE IMPLANTED COCHLEA. IEEE/Engineering in Medicine and Biology Society Annual Conference, 1987. 1904-1905.

GROSS, L. 2017. *3D MODELLING OF POST-COCHLEAR IMPLANT FACIAL NERVE STIMULATION IN A SPECIFIC USER.* Master of Engineering (Bio-Engineering) Dessertation, University of Pretoria.

GUPTA, A., KHARBANDA, O. P., SARDANA, V., BALACHANDRAN, R. & SARDANA, H. K. 2015. A knowledge-based algorithm for automatic detection of

cephalometric landmarks on CBCT images. *International Journal of Computer Assisted Radiology and Surgery,* 10**,** 1737-1752.

HANDZEL, O., WANG, H., FIERING, J., BORENSTEIN, J. T., MESCHER, M. J., LEARY SWAN, E. E., MURPHY, B. A., CHEN, Z., PEPPI, M., SEWELL, W. F., KUJAWA, S. G. & MCKENNA, M. J. 2009. Mastoid cavity dimensions and shape: Method of measurement and virtual fitting of implantable devices. *Audiology and Neurotology,* 14**,** 308-314.

HANEKOM, T. & HANEKOM, J. J. 2016. Three-dimensional models of cochlear implants: A review of their development and how they could support management and maintenance of cochlear implant performance. *Network: Computation in Neural Systems,* 27**,** 67-106.

HERMAN, T. 2009. Image reconstruction from projection. *Fundamentals of computerized tomography: Image reconstruction from projection.* 2 ed.: Springer.

LI, P. M. M. C., WANG, H., NORTHROP, C., MERCHANT, S. N. & NADOL JR, J. B. 2007. Anatomy of the round window and hook region of the cochlea with implications for cochlear implantation and other endocochlear surgical procedures. *Otology and Neurotology,* 28**,** 641-648.

MALHERBE, T. K. 2009. *DEVELOPMENT OF A METHOD TO CREATE SUBJECT SPECIFIC COCHLEAR MODELS FOR ELECTRIC HEARING.* Master of Engineering (Bio-Engineering), UNIVERSITY OF PRETORIA.

MALHERBE, T. K., HANEKOM, T. & HANEKOM, J. J. 2013. Can subject-specific single-fibre electrically evoked auditory brainstem response data be predicted from a model? *Medical Engineering and Physics,* 35**,** 926-936.

MALHERBE, T. K., HANEKOM, T. & HANEKOM, J. J. 2015. The effect of the resistive properties of bone on neural excitation and electric fields in cochlear implant models. *Hearing Research,* 327**,** 126-135.

MALHERBE, T. K., HANEKOM, T. & HANEKOM, J. J. 2016. Constructing a three-dimensional electrical model of a living cochlear implant user's cochlea. *International Journal for Numerical Methods in Biomedical Engineering,* 32.

MANGADO, N., CERESA, M., DUCHATEAU, N., KJER, H. M., VERA, S., DEJEA VELARDO, H., MISTRIK, P., PAULSEN, R. R., FAGERTUN, J., NOAILLY, J., PIELLA, G. & GONZÁLEZ BALLESTER, M. Á. 2016. Automatic Model Generation Framework for Computational Simulation of Cochlear Implantation. *Annals of Biomedical Engineering,* 44**,** 2453-2463.

NADOL J.B, JR., BURGESS, B. J., GANTZ, B. J., COKER, N. J., KETTEN, D. R., KOS, I., ROLAND J.T, JR., JIUN YIH SHIAO, D. K., EDDINGTON, D. K., MONTANDON, P. & SHALLOP, J. K. 2001. Histopathology of cochlear implants in humans. *Annals of Otology, Rhinology and Laryngology,* 110**,** 883-891.

NOBLE, J. H., LABADIE, R. F., MAJDANI, O. & DAWANT, B. M. 2011. Automatic segmentation of intracochlear anatomy in conventional CT. *IEEE Transactions on Biomedical Engineering,* 58**,** 2625-2632.

RATTAY, F. 1989. Analysis of Models for Extracellular Fiber Stimulation. *IEEE Transactions on Biomedical Engineering,* 36**,** 676-682.

RATTAY, F. 1999. The basic mechanism for the electrical stimulation of the nervous system. *Neuroscience,* 89**,** 335-346.

RATTAY, F., LEAO, R. N. & FELIX, H. 2001. A model of the electrically excited human cochlear neuron. II. Influence of the three-dimensional cochlear structure on neural excitability. *Hearing Research,* 153**,** 64-79.

RAU, T. S., WÜRFEL, W., LENARZ, T. & MAJDANI, O. 2013. Three-dimensional histological specimen preparation for accurate imaging and spatial reconstruction of the middle and inner ear. *International Journal of Computer Assisted Radiology and Surgery,* 8**,** 481-509.

RAZAFINDRANALY, V., TRUY, E., PIALAT, J. B., MARTINON, A., BOURHIS, M., BOUBLAY, N., FAURE, F. & LTAIEF-BOUDRIGUA, A. 2016. Cone Beam CT versus multislice CT: Radiologic diagnostic agreement in the postoperative assessment of cochlear implantation. *Otology and Neurotology,* 37**,** 1246-1254.

REDA, F. A., DAWANT, B. M., MCRACKAN, T. R., LABADIE, R. F. & NOBLE, J. H. Automatic segmentation of intra-cochlear anatomy in post-implantation CT. Proceedings of SPIE - The International Society for Optical Engineering, 2013.

RODT, T., RATIU, P., BECKER, H., BARTLING, S., KACHER, D. F., ANDERSON, M., JOLESZ, F. A. & KIKINIS, R. 2002. 3D visualisation of the middle ear and adjacent structures using reconstructed multi-slice CT datasets, correlating 3D images and virtual endoscopy to the 2D cross-sectional images. *Neuroradiology,* 44**,** 783-790.

SARI, I. P., WIDAYATI, R., PRIAMINIARTI, M., DANUDIRDJO, D. & MENGKO, T. L. Initial estimation of landmark location for automated cephalometric analysis using template matching method. Proceedings - 2015 4th International Conference on Instrumentation, Communications, Information Technology and Biomedical Engineering, ICICI-BME 2015, 2015. 159-162.

SHAHIDI, S., BAHRAMPOUR, E., SOLTANIMEHR, E., ZAMANI, A., OSHAGH, M., MOATTARI, M. & MEHDIZADEH, A. 2014. The accuracy of a designed software for automated localization of craniofacial landmarks on CBCT images. *BMC Medical Imaging,* 14.

SOLIDWORKS.COM. 2015. *SOLIDWORKS Standard* [Online]. Available: http://www.solidworks.com/sw/products/3d-cad/solidworks-standard.htm. [Accessed 26 September 2015].

TRAN, P., SUE, A., WONG, P., LI, Q. & CARTER, P. 2015. Development of HEATHER for cochlear implant stimulation using a new modeling workflow. *IEEE Transactions on Biomedical Engineering,* 62**,** 728-735.

VERBIST, B. M., FERRARINI, L., BRIAIRE, J. J., ZAROWSKI, A., ADMIRAAL-BEHLOUL, F., OLOFSEN, H., REIBER, J. H. C. & FRIJNS, J. H. M. 2009. Anatomic considerations of cochlear morphology and its implications for insertion trauma in cochlear implant surgery. *Otology and Neurotology,* 30**,** 471-477.

WANG, G. & VANNIER, M. W. 1998. Spiral CT image deblurring for cochlear implantation. *IEEE Transactions on Medical Imaging,* 17**,** 251-262.

WANG, H., NORTHROP, C., BURGESS, B., LIBERMAN, M. C. & MERCHANT, S. N. 2006. Three-dimensional virtual model of the human temporal bone: A stand-alone, downloadable teaching tool. *Otology and Neurotology,* 27**,** 452-457.

YOO, K. S., WANG, G., RUBINSTEIN, J. T., SKINNER, M. W. & VANNIER, M. W. 2000a. Three-dimensional modeling and visualization of the cochlea on the

internet. *IEEE Transactions on Information Technology in Biomedicine,* 4**,** 144-151.

YOO, S. K., WANG, G., RUBINSTEIN, J. T. & VANNIER, M. W. 2000b. Three-dimensional geometric modeling of the cochlea using helico-spiral approximation. *IEEE Transactions on Biomedical Engineering,* 47**,** 1392-1402.

ADDENDUM A EQUATIONS APPLIED IN METHOD

A.1. Cochlea anatomical measurement database loaded as reference data

The knowledge database set, $\mathrm{CT}^{\mathrm{Set}}$, is loaded into MATLAB. Equations (A.1) to (A.3) below, depict the data set layout. The variables θ, ρ and z represent the angular position, radius and height values of the reference data, respectively. The terms *upper* and *lower* refer to the most superior and most inferior cochlear duct landmark points, respectively.

$$\mathrm{CT}^{\mathrm{Set}}\{1\} = \mathrm{CT}^{\mathrm{Upper}} = [\overline{\theta^{\mathrm{Upper}}} \quad \overline{\rho^{\mathrm{Upper}}} \quad \overline{z^{\mathrm{Upper}}}] \tag{A.1}$$

$$\mathrm{CT}^{\mathrm{Set}}\{2\} = \mathrm{CT}^{\mathrm{Lateral}} = [\overline{\theta^{\mathrm{Lateral}}} \quad \overline{\rho^{\mathrm{Lateral}}} \quad \overline{z^{\mathrm{Lateral}}}] \tag{A.2}$$

$$\mathrm{CT}^{\mathrm{Set}}\{3\} = \mathrm{CT}^{\mathrm{Lower}} = [\overline{\theta^{\mathrm{Lower}}} \quad \overline{\rho^{\mathrm{Lower}}} \quad \overline{z^{\mathrm{Lower}}}] \tag{A.3}$$

A.2. Introducing user anatomical data

Equation (A.4) depicts the mathematical representation of CT scan image I, with n representing the CT scan slide number, which is one for each degree; therefore n stretches from 1 to 180 degrees in increments of 1 degree. Variables i and j represent the row and column of each pixel, respectively. When viewing an image, i and j each start at a value of 1 at the top left corner of the image. In addition, the user is asked to give the dimension of the image height (a_{mm}) and width (b_{mm}) in mm, which can be obtained from ImageJ in order to calculate the conversion factor from pixel to mm.

$$\text{CT Scan Input Image} = I = \left(I_{ij}\right)_n \in R^{a\times b} \tag{A.4}$$

A.3. Create three contrast enhanced images from each CT scan

Figure A.1 depicts the initial image data processing workflow.

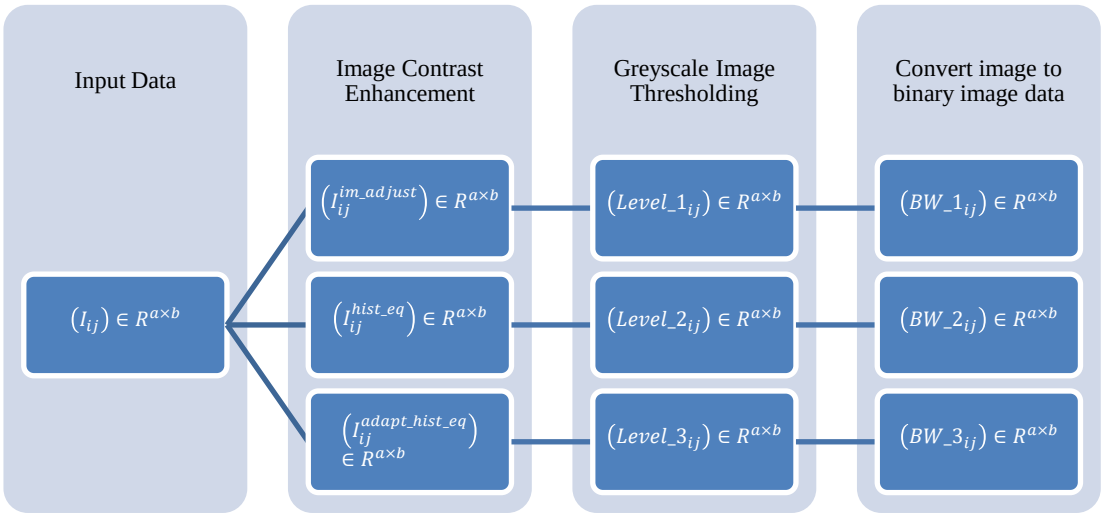

Figure A.1 – Image processing workflow diagram depicting the methods used to increase image contrast as well as the relevant variables to which these images are assigned.

A.4. Detect all possible apical points on CT scan

As the apical point can be defined as a boundary point, boundaries are easily detected by using binary images. An apical point is defined as the boundary point with a binary value of 1, with at least 3 points of binary value 0 located directly below that point on a binary image. The x and y coordinates of these points on the CT scan image, identified as possible apical points, are extracted and stored in a matrix.

To find the possible apical points, the binary image data from BW_1 and BW_2 are combined, which is then evaluated as described in the equations below.

- Binary image data is combined as seen in equation (A.5).

$$\text{Combined binary image BW3\_B} = (\text{BW\_1} \cup \text{BW\_2}) \tag{A.5}$$

- The first criterion that defines possible apical points is described in Equations (A.6) to (A.9). Coordinates i and j represent the width (rows) and length (columns) of the image in pixels respectively, each starting at the top left corner each image.

$$BW3\_B(i,j) = 1 \quad (A.6)$$

$$BW3\_B(i+1,j-1) = 0 \quad (A.7)$$

$$BW3\_B(i+1,j) = 0 \quad (A.8)$$

$$BW3\_B(i+1,j+1) = 0 \quad (A.9)$$

The coordinates (i,j) of each point, which adheres to the criteria given in equations (A.6) to (A.9) above, are stored in the matrix $\mathrm{Coord1}$.

A.5. Detect possible nerve width narrowing below possible apical point

The second criterion to be met is the detection of the points at which the minimum nerve width is located. To find these points, the function `nerve_width_detection` was developed in which the knowledge database was used. The data was used to create a search field on the contrast enhanced binary image (BW3_B) in which points that adhered to a specific set of criteria, associated with nerve width narrowing, were searched for.

The following variables and equations are used to describe how the location of each point is found at which the minimum nerve width is measured.

- Variables used during nerve width detection:

$$x^{apical} = \text{Possible apical point x coordinate value}$$

$$y^{apical} = \text{Possible apical point y coordinate value}$$

$$\mu^{height\_mm} = \text{Mean value of the height of cochleae in mm}$$

$$\sigma^{height\_mm} = \text{Standard deviation of the height of cochleae in mm}$$

$$\mu^{nerve\_width\_mm} = \text{Mean value of the nerve width of cochleae in mm}$$

$$\sigma^{nerve\_width\_mm} = \text{Standard deviation of the nerve width of cochleae in mm}$$

$$\overline{coord}^{nerve\_L} = \left[coord_x^{nerve\_L} \quad coord_y^{nerve\_L}\right]$$

$$= \text{Vector of nerve width boundary point coordinates on the left side of the apical point}$$

$$\overline{coord}^{nerve\_R} = \left[coord_x^{nerve\_R} \quad coord_y^{nerve\_R}\right]$$

$$= \text{Vector of nerve width boundary point coordinates on the right side of the apical point}$$

- The values of the variables in mm are first converted to pixel coordinates by taking the ratio of the dimension of the image in mm over the dimension of the image in

pixels. Equations (A.10) to (A.14) are used to convert the variables in mm to pixel dimensions.

$$\text{factor} = \frac{a_{mm}}{a} = \frac{b_{mm}}{b} \tag{A.10}$$

$$\mu^{height} = \frac{\mu^{height\_mm}}{\text{factor}} = \text{Equivalent mean height in pixels} \tag{A.11}$$

$$\sigma^{height} = \frac{\sigma^{height\_mm}}{\text{factor}} = \text{Equivalent standard deviation of height in pixels} \tag{A.12}$$

$$\mu^{nerve\_width} = \frac{\mu^{nerve\_width\_mm}}{\text{factor}} = \text{Equivalent mean nerve widt in pixels} \tag{A.13}$$

$$\sigma^{nerve\_width} = \frac{\sigma^{nerve\_width\_mm}}{\text{factor}} = \text{Equivalent standard deviation of nerve width in pixels} \tag{A.14}$$

- Equations (A.15) to (A.19) indicate how the boundaries are determined for the x and the y coordinates on the matrix BW3_B in order to determine $\overline{coord}^{nerve\_L}$ and $\overline{coord}^{nerve\_R}$.

  If

$$BW3\_B = BW3\_B(i,j) \tag{A.15}$$

  The range for i and j is given in equation (A.16) and (A.17), respectively. These equations describe the search field within which the left hand nerve narrowing boundary point, $\overline{coord}^{nerve\_L}$, is determined.

$$\left(x^{apical} + \mu^{height} - \sigma^{height}\right) \leq i \leq \left(x^{apical} + \mu^{height} + \sigma^{height}\right) \tag{A.16}$$

$$\left(y^{apical} - \mu^{nerve\_width} - \sigma^{nerve\_width}\right) \leq j \leq \left(y^{apical}\right) \tag{A.17}$$

  The range for i and j is given in Equation (A.18) and (A.19), respectively. These equations describe the search field within which the right hand nerve narrowing boundary point, $\overline{coord}^{nerve\_R}$, is determined.

$$\left(x^{apical} + \mu^{height} - \sigma^{height}\right) \leq i \leq \left(x^{apical} + \mu^{height} + \sigma^{height}\right) \tag{A.18}$$

$$\left(y^{apical}\right) \leq j \leq \left(y^{apical} + \mu^{nerve\_width} + \sigma^{nerve\_width}\right) \tag{A.19}$$

- The conditions that the possible nerve width points situated to the left of the apical point must adhere to, are described in Equations (A.20) to (A.21) below. These equations refer to a single binary image coordinate with a binary value equal to 1, located to the left of a binary image coordinate of binary value 0.

$$\mathrm{BW3\_B}(i,j) = 1 \tag{A.20}$$

$$\mathrm{BW3\_B}(i,j+1) = 0 \tag{A.21}$$

- The conditions that the possible nerve width points situated to the right of the apical point must adhere to, is described in Equations (A.22) to (A.23) below. These equations refer to a single binary image coordinate with a binary value equal to 1, located to the right of a binary image coordinate of binary value 0.

$$\mathrm{BW3\_B}(i,j) = 1 \tag{A.22}$$

$$\mathrm{BW3\_B}(i,j-1) = 0 \tag{A.23}$$

- All point coordinates within the defined search field that adhere to the specified criteria above are stored in the matrices $\mathrm{coord}^{\mathrm{nerve\_L}}$ and $\mathrm{coord}^{\mathrm{nerve\_R}}$ for points to left and right of the apical point, respectively.

The shortest distance between the points in $\mathrm{coord}^{\mathrm{nerve\_L}}$ and $\mathrm{coord}^{\mathrm{nerve\_R}}$ is calculated. The points that yield the shortest distance between the two matrices are determined as the minimum nerve width points and define the vectors $\overline{\mathrm{coord}}^{\mathrm{nerve\_L}}$ and $\overline{\mathrm{coord}}^{\mathrm{nerve\_R}}$, respectively.

A.6. Evaluate tissue material between possible nerve width narrowing and apical point

In order to find the cochlea on the CT scan, a third condition is applied that must be adhered to. This condition evaluates the percentage of soft tissue content between the apical point and the points where the minimum nerve width is located. If the percentage of soft tissue between the apical point and the minimum nerve width points is 75% or greater, the third condition is met.

To check for the soft tissue content on the CT image, the combined binary image data BW3_B is used. The binary image data consists of a matrix with a size equal to that of the height (a) and width (b) of the input image. Each matrix entry either contains a value of 1 or 0, and these values are associated with denser tissues such as bone and soft tissue (e.g. nerve tissue), respectively. A search field is created on the BW3_B image data between the apical point and the lowest point between $\overline{\text{coord}}^{\text{nerve\_L}}$ and $\overline{\text{coord}}^{\text{nerve\_R}}$. The total number of points in the search field with a value equal to 0 is counted. This value is then compared to the total number of points in the search field by calculating the percentage of points occupied by soft tissue (i.e. points with value equal to 0).

- Equations (A.24) and (A.25) indicate how the boundaries are determined for the search field matrix Test_Section on the larger binary image data matrix BW3_B.

  Boundaries on the x coordinates of the soft tissue search field

$$\text{x}^{\text{apical}} \leq \text{BW3\_B} \leq \max\begin{pmatrix}\text{coord}_{\text{x}}^{\text{nerve\_L}} \\ \text{coord}_{\text{x}}^{\text{nerve\_R}}\end{pmatrix} \tag{A.24}$$

  Boundaries on the y coordinates of the soft tissue search field

$$\text{coord}_{\text{y}}^{\text{nerve\_L}} \leq \text{BW3\_B} \leq \text{coord}_{\text{y}}^{\text{nerve\_R}} \tag{A.25}$$

- Within the boundaries of the search field, equation (A.26) define how the third criterion is tested for:

$$\text{soft\_tissue}\ \% = \left(\frac{\sum(\text{Test}_{\text{Section}} = 0)}{\sum(\text{Test}_{\text{Section}} = 0) + \sum(\text{Test}_{\text{Section}} = 1)}\right) \times 100 \tag{A.26}$$

- If the $\text{soft\_tissue}\ \% \geq 75\%$, the third condition is met and the cochlea is considered found on the CT scan.

After the cochlea is initially found on all CT scans, the mean of apical point coordinates is calculated and used for all the remaining calculations as x^{apical} and y^{apical}. These variables represent the mean x and y coordinate values of the apical point, respectively.

A.7. Detecting cochlear landmarks

The cochlea landmarks that should be identified are the most lateral, most superior, and most inferior boundary points of the cochlear for both the basal and middle turn on each CT image. These boundary points will subsequently be referred to as the lateral, upper and lower spiral boundary points, respectively.

The function *outline_finder* was developed to determine the boundary points in the given range and makes use of built-in Matlab functions, which utilise the Canny method to locate boundary points. The coordinates of all the boundary points detected with the *outline_finder* code is stored in a matrix labelled CC2.

- The boundary points in matrix CC2 are divided into two matrices, CC2_L and CC2_R, which represent the boundary points to left and right of the cochlea, respectively.
- The values contained in CC2_L and CC2_R are given in terms of pixel coordinates, which are then converted to dimensions in mm, as shown in Equations (A.27) to (A.32).

  Say that

$$\mathrm{CC2\_L} = \left[\overline{\mathrm{CC2\_L_x}} \quad \overline{\mathrm{CC2\_L_y}}\right] \tag{A.27}$$

$$\mathrm{CC2\_R} = \left[\overline{\mathrm{CC2\_R_x}} \quad \overline{\mathrm{CC2\_R_y}}\right] \tag{A.28}$$

  Then

$$\overline{\mathrm{CC2\_L\_x\_mm}} = \mathrm{factor} \times \left(\overline{\mathrm{CC2\_L_y}} - \mathrm{y^{apical}}\right) \tag{A.29}$$

$$\overline{\mathrm{CC2\_R\_x\_mm}} = \mathrm{factor} \times \left(\mathrm{y^{apical}} - \overline{\mathrm{CC2\_L_y}}\right) \tag{A.30}$$

$$\overline{\mathrm{CC2\_L\_y\_mm}} = \mathrm{factor} \times \left(\overline{\mathrm{CC2\_L_x}} - \mathrm{x^{apical}}\right) \tag{A.31}$$

$$\overline{\mathrm{CC2\_R\_y\_mm}} = \mathrm{factor} \times \left(\overline{\mathrm{CC2\_R_x}} - \mathrm{x^{apical}}\right) \tag{A.32}$$

- The error ratio is then calculated between the converted dimensional data above and the reference data. Equations (A.33) to (A.40) are used to calculate the error ratios. The error ratio between the reference data, ρ, and the extracted boundary points, CC2, is calculated for the basal and middle turn of the cochlea. By doing so, landmark points can be detected at multiple cochlear turns on each CT scan image.

The equations below were applied to the upper spiral as well as the lateral and lower spirals.

$$\overline{\text{error\_rho\_L\_upper\_base}} = \frac{\left|\overline{\text{CC2\_L\_x\_mm}} - (\rho^{\text{Upper}})_{\text{n}}\right|}{(\rho^{\text{Upper}})_{\text{n}}} \tag{A.33}$$

$$\overline{\text{error\_rho\_R\_upper\_base}} = \frac{\left|\overline{\text{CC2\_L\_x\_mm}} - (\rho^{\text{Upper}})_{180\text{n}}\right|}{(\rho^{\text{Upper}})_{180+\text{n}}} \tag{A.34}$$

$$\overline{\text{error\_rho\_L\_upper\_middle}} = \frac{\left|\overline{\text{CC2\_L\_x\_mm}} - (\rho^{\text{Upper}})_{360+\text{n}}\right|}{(\rho^{\text{Upper}})_{360+\text{n}}} \tag{A.35}$$

$$\overline{\text{error\_rho\_R\_upper\_middle}} = \frac{\left|\overline{\text{CC2\_L\_x\_mm}} - (\rho^{\text{Upper}})_{540+\text{n}}\right|}{(\rho^{\text{Upper}})_{540+\text{n}}} \tag{A.36}$$

$$\overline{\text{error\_z\_L\_upper\_base}} = \frac{\left|\overline{\text{CC2\_L\_y\_mm}} - (\text{z}^{\text{Upper}})_{\text{n}}\right|}{(\text{z}^{\text{Upper}})_{\text{n}}} \tag{A.37}$$

$$\overline{\text{error\_z\_R\_upper\_base}} = \frac{\left|\overline{\text{CC2\_L\_y\_mm}} - (\text{z}^{\text{Upper}})_{180+\text{n}}\right|}{(\text{z}^{\text{Upper}})_{180+\text{n}}} \tag{A.38}$$

$$\overline{\text{error\_z\_L\_upper\_middle}} = \frac{\left|\overline{\text{CC2\_L\_y\_mm}} - (\text{z}^{\text{Upper}})_{360+\text{n}}\right|}{(\text{z}^{\text{Upper}})_{360+\text{n}}} \tag{A.39}$$

$$\overline{\text{error\_z\_R\_upper\_middle}} = \frac{\left|\overline{\text{CC2\_L\_y\_mm}} - (\text{z}^{\text{Upper}})_{540+\text{n}}\right|}{(\text{z}^{\text{Upper}})_{540+\text{n}}} \tag{A.40}$$

To determine which of the points fall within the small search field for each individual landmark at each turn of the three spirals, the limits of the landmark points for the upper $(\overline{\sigma_{\text{upper}}})$, lateral $(\overline{\sigma_{\text{lateral}}})$ and lower spirals $(\overline{\sigma_{\text{upper}}})$ are used. Equations (A.41) to (A.48) are used to calculate the accepted maximum error level for the each of the spirals. All boundary points that fall within the relevant search fields are deemed as valid points.

$$\text{error\_val\_LBtx} = \frac{\left|\left(\sigma_{\text{upper}}\right)_{n}\right|}{\left(\rho^{\text{Upper}}\right)_{n}} \tag{A.41}$$

$$\text{error\_val\_RBtx} = \frac{\left|\left(\sigma_{\text{upper}}\right)_{180+n}\right|}{\left(\rho^{\text{Upper}}\right)_{180+n}} \tag{A.42}$$

$$\text{error\_val\_LMtx} = \frac{\left|\left(\sigma_{\text{upper}}\right)_{360+n}\right|}{\left(\rho^{\text{Upper}}\right)_{360+n}} \tag{A.43}$$

$$\text{error\_val\_RMtx} = \frac{\left|\left(\sigma_{\text{upper}}\right)_{540+n}\right|}{\left(\rho^{\text{Upper}}\right)_{540+n}} \tag{A.44}$$

$$\text{error\_val\_LBty} = \frac{\left|\left(\sigma_{\text{upper}}\right)_{n}\right|}{\left(z^{\text{Upper}}\right)_{n}} \tag{A.45}$$

$$\text{error\_val\_RBty} = \frac{\left|\left(\sigma_{\text{upper}}\right)_{180+n}\right|}{\left(z^{\text{Upper}}\right)_{180+n}} \tag{A.46}$$

$$\text{error\_val\_LMty} = \frac{\left|\left(\sigma_{\text{upper}}\right)_{360+n}\right|}{\left(z^{\text{Upper}}\right)_{360+n}} \tag{A.47}$$

$$\text{error\_val\_RMty} = \frac{\left|\left(\sigma_{\text{upper}}\right)_{540+n}\right|}{\left(z^{\text{Upper}}\right)_{540+n}} \tag{A.48}$$

Once the maximum error values are determined, the boundary points that produce errors lower than the calculated maximum for both the radius and height dimensions of each spiral are identified. Equations (A.49) to (A.60) each give a mathematical representation of how these values are determined for each spiral.

$$\overline{\text{upper\_points\_mm\_11}_{x}} = \overline{\text{CC2\_L\_x\_mm}}\ (\overline{\text{error\_rho\_L\_upper\_base}} \leq \text{error\_val\_LBtx}) \tag{A.49}$$

$$\overline{\text{upper\_points\_mm\_11}_{y}} = \overline{\text{CC2\_L\_y\_mm}}\ (\overline{\text{error\_z\_L\_upper\_base}} \leq \text{error\_val\_LBty}) \tag{A.50}$$

$$\text{upper\_points\_mm\_11} = \left[\overline{\text{upper\_points\_mm\_11}_{x}}\ \ \overline{\text{upper\_points\_mm\_11}_{y}}\right] \tag{A.51}$$

$$\overline{\text{upper\_points\_mm\_22}_x} = \overline{\text{CC2\_R\_x\_mm}}\ (\overline{\text{error\_rho\_R\_upper\_base}} \leq \text{error\_val\_RBtx}) \quad \text{(A.52)}$$

$$\overline{\text{upper\_points\_mm\_22}_y} = \overline{\text{CC2\_R\_y\_mm}}\ (\overline{\text{error\_z\_R\_upper\_base}} \leq \text{error\_val\_RBty}) \quad \text{(A.53)}$$

$$\text{upper\_points\_mm\_22} = \left[\overline{\text{upper\_points\_mm\_22}_x} \quad \overline{\text{upper\_points\_mm\_22}_y}\right] \quad \text{(A.54)}$$

$$\overline{\text{upper\_points\_mm\_33}_x} = \overline{\text{CC2\_L\_x\_mm}}\ (\overline{\text{error\_rho\_L\_upper\_middle}} \leq \text{error\_val\_LMtx}) \quad \text{(A.55)}$$

$$\overline{\text{upper\_points\_mm\_33}_y} = \overline{\text{CC2\_L\_y\_mm}}\ (\overline{\text{error\_z\_L\_upper\_middle}} \leq \text{error\_val\_LMty}) \quad \text{(A.56)}$$

$$\text{upper\_points\_mm\_33} = \left[\overline{\text{upper\_points\_mm\_33}_x} \quad \overline{\text{upper\_points\_mm\_33}_y}\right] \quad \text{(A.57)}$$

$$\overline{\text{upper\_points\_mm\_44}_x} = \overline{\text{CC2\_R\_x\_mm}}\ (\overline{\text{error\_rho\_R\_upper\_middle}} \leq \text{error\_val\_RMtx}) \quad \text{(A.58)}$$

$$\overline{\text{upper\_points\_mm\_44}_y} = \overline{\text{CC2\_R\_y\_mm}}\ (\overline{\text{error\_z\_R\_upper\_middle}} \leq \text{error\_val\_RMty}) \quad \text{(A.59)}$$

$$\text{upper\_points\_mm\_44} = \left[\overline{\text{upper\_points\_mm\_44}_x} \quad \overline{\text{upper\_points\_mm\_44}_y}\right] \quad \text{(A.60)}$$

Each of the matrices calculated above contain either multiple possible landmark points, or none at all for each relevant spiral. If the matrices determined in the previous step contain multiple point entries, the mean value of the radius (μ_{radius}) and the height (μ_z) of the landmark points for each separate matrix, are calculated for the CT image at n degrees. Equations (A.61) to (A.64) give a mathematical representation of these described calculations.

$$\text{upper\_points\_basal\_L}(n, 1{:}2) = \left[\mu_{radius}^{\overline{\text{upper\_points\_mm\_11}_x}} \quad \mu_z^{\overline{\text{upper\_points\_mm\_11}_y}}\right] \quad \text{(A.61)}$$

$$\text{upper\_points\_basal\_R}(n, 1{:}2) = \left[\mu_{radius}^{\overline{\text{upper\_points\_mm\_22}_x}} \quad \mu_z^{\overline{\text{upper\_points\_mm\_22}_y}}\right] \quad \text{(A.62)}$$

$$\text{upper\_points\_middle\_L}(n, 1{:}2) = \left[\mu_{radius}^{\overline{\text{upper\_points\_mm\_33}_x}} \quad \mu_z^{\overline{\text{upper\_points\_mm\_33}_y}}\right] \quad \text{(A.63)}$$

$$\text{upper\_points\_middle\_R}(n, 1{:}2) = \left[\mu_{radius}^{\overline{\text{upper\_points\_mm\_44}_x}} \quad \mu_z^{\overline{\text{upper\_points\_mm\_44}_y}}\right] \quad \text{(A.64)}$$

If no points were found within the small search fields for any of the landmark points of the several spirals, that point is deemed invalid and treated similarly by assigning a value of [0,0].

A.8. Data processing

The next step involved in the model development algorithm, is initiated once all possible landmark points are extracted from the CT scans images. This data processing step involves the analysis and refinement of the extracted coordinate datasets.

- These matrices of valid points are smoothed and interpolated in order to create a continuous set of data; from the smallest angular position of valid data to the highest angular position of valid data.

  For the upper spiral, the matrices containing the smoothed data series are named sUpper_points_basal_L, sUpper_points_basal_R, sUpper_points_middle_L and sUpper_points_middle_R.

- The matrices of each spiral are combined to form one single matrix that represents the spirals in polar coordinates. The composition of such a matrix is given in Equation (A.65).

  For the upper spiral

$$\mathrm{sUpper} = \begin{bmatrix} \mathrm{sUpper\_points\_basal\_L} \\ \mathrm{sUpper\_points\_basal\_R} \\ \mathrm{sUpper\_points\_middle\_L} \\ \mathrm{sUpper\_points\_middle\_R} \end{bmatrix} \tag{A.65}$$

- The polar coordinates in the matrices above are converted to Cartesian coordinates with the use of Equations (A.66) to (A.69) below.

The matrix entries in sUpper contain the polar coordinate vectors such as the angular position in degrees, $\overline{\theta_{\mathrm{Upper}}}$, the radius in millimetre, $\overline{\rho_{\mathrm{Upper}}}$, and the height of the landmark point, $\overline{z_{\mathrm{Upper}}}$, for the upper spiral. The equivalent Cartesian coordinates for the spiral Upper are then determined in Equation (A66) to (A69). The same method is followed for the remaining spiral landmark points and electrode array spiral points.

$$\overline{\mathrm{Upper}_x} = \overline{\rho_{\mathrm{Upper}}}\cos\left(\overline{\theta_{\mathrm{Upper}}}\right) \tag{A.66}$$

$$\overline{\mathrm{Upper}_y} = \overline{\rho_{\mathrm{Upper}}}\sin\left(\overline{\theta_{\mathrm{Upper}}}\right) \tag{A.67}$$

$$\overline{\mathrm{Upper}_z} = \overline{z_{\mathrm{Upper}}} \tag{A.68}$$

$$\mathrm{Upper} = \left[\overline{\mathrm{Upper}_x} \quad \overline{\mathrm{Upper}_y} \quad \overline{\mathrm{Upper}_z}\right] \tag{A.69}$$